

1

Global Carbon Budget 2020

2 Pierre Friedlingstein^{1,2}, Michael O'Sullivan¹, Matthew W. Jones³, Robbie M. Andrew⁴, Judith Hauck⁵,
3 Are Olsen^{6,7}, Glen P. Peters⁴, Wouter Peters^{8,9}, Julia Pongratz^{10,11}, Stephen Sitch¹², Corinne Le Quéré³,
4 Josep G. Canadell¹³, Philippe Ciais¹⁴, Robert B. Jackson¹⁵, Simone Alin¹⁶, Luiz E.O.C. Aragão^{17,12}, Almut
5 Arneeth¹⁸, Vivek Arora¹⁹, Nicholas R. Bates^{20,21}, Meike Becker^{6,7}, Alice Benoit-Cattin²², Henry C. Bittig²³,

¹ College of Engineering, Mathematics and Physical Sciences, University of Exeter, Exeter EX4 4QF, UK

² Laboratoire de Météorologie Dynamique, Institut Pierre-Simon Laplace, CNRS-ENS-UPMC-X, Département de Géosciences, Ecole Normale Supérieure, 24 rue Lhomond, 75005 Paris, France

³ Tyndall Centre for Climate Change Research, School of Environmental Sciences, University of East Anglia, Norwich Research Park, Norwich NR4 7TJ, UK

⁴ CICERO Center for International Climate Research, Oslo 0349, Norway

⁵ Alfred-Wegener-Institut Helmholtz-Zentrum für Polar- und Meeresforschung, Postfach 120161, 27515 Bremerhaven, Germany

⁶ Geophysical Institute, University of Bergen, Bergen, Norway

⁷ Bjerknes Centre for Climate Research, Bergen, Norway

⁸ Wageningen University, Environmental Sciences Group, P.O. Box 47, 6700AA, Wageningen, The Netherlands

⁹ University of Groningen, Centre for Isotope Research, Groningen, The Netherlands

¹⁰ Ludwig-Maximilians-Universität Munich, Luisenstr. 37, 80333 München, Germany

¹¹ Max Planck Institute for Meteorology, Hamburg, Germany

¹² College of Life and Environmental Sciences, University of Exeter, Exeter EX4 4RJ, UK

¹³ CSIRO Oceans and Atmosphere, Canberra, ACT 2101, Australia

¹⁴ Laboratoire des Sciences du Climat et de l'Environnement, LSCE/IPSL, CEA-CNRS-UVSQ, Université Paris-Saclay, F-91198 Gif-sur-Yvette, France

¹⁵ Department of Earth System Science, Woods Institute for the Environment, and Precourt Institute for Energy, Stanford University, Stanford, CA 94305–2210, United States of America

¹⁶ National Oceanic & Atmospheric Administration, Pacific Marine Environmental Laboratory (NOAA/PMEL), 7600 Sand Point Way NE, Seattle, WA 98115, USA

¹⁷ Remote Sensing Division, National Institute for Space Research, São José dos Campos, Brazil

¹⁸ Karlsruhe Institute of Technology, Institute of Meteorology and Climate Research/Atmospheric Environmental Research, 82467 Garmisch-Partenkirchen, Germany

¹⁹ Canadian Centre for Climate Modelling and Analysis, Climate Research Division, Environment and Climate Change Canada, Victoria, BC, Canada

²⁰ Bermuda Institute of Ocean Sciences (BIOS), 17 Biological Lane, St. Georges, GE01, Bermuda

²¹ Department of Ocean and Earth Science, University of Southampton, European Way, Southampton, SO14 3ZH, UK

²² Marine and Freshwater Research Institute, Fornubudir 5, 220 Hafnarfjörður, Iceland

²³ Leibniz Institute for Baltic Sea Research Warnemuende (IOW), Seestrasse 15; 18119 Rostock, Germany

6 Laurent Bopp²⁴, Selma Bultan¹⁰, Naveen Chandra^{25,26}, Frédéric Chevallier¹⁴, Louise P. Chini²⁷, Wiley
7 Evans²⁸, Liesbeth Florentie⁸, Piers M. Forster²⁹, Thomas Gasser³⁰, Marion Gehlen¹⁴, Dennis Gilfillan³¹,
8 Thanos Gkritzalis³², Luke Gregor³³, Nicolas Gruber³³, Ian Harris³⁴, Kerstin Hartung^{10,35}, Vanessa
9 Haverd¹³, Richard A. Houghton³⁶, Tatiana Ilyina¹¹, Atul K. Jain³⁷, Emilie Joetzjer³⁸, Koji Kadono³⁹,
10 Etsushi Kato⁴⁰, Vassilis Kitidis⁴¹, Jan Ivar Korsbakken⁴, Peter Landschützer¹¹, Nathalie Lefèvre⁴²,
11 Andrew Lenton⁴³, Sebastian Lienert⁴⁴, Zhu Liu⁴⁵, Danica Lombardozzi⁴⁶, Gregg Marland^{31,47}, Nicolas

²⁴ Laboratoire de Météorologie Dynamique / Institut Pierre-Simon Laplace, CNRS, Ecole Normale Supérieure / Université PSL, Sorbonne Université, Ecole Polytechnique, Paris, France

²⁵ Japan Agency for Marine-Earth Science and Technology (JAMSTEC), Yokohama, 236-0001

²⁶ Center for Global Environmental Research, National Institute for Environmental Studies (NIES), 16-2 Onogawa, Tsukuba, Ibaraki, 305-8506, Japan

²⁷ Department of Geographical Sciences, University of Maryland, College Park, Maryland 20742, USA

²⁸ Hakai Institute, Heriot Bay, BC, Canada

²⁹ Priestley International Centre for Climate, University of Leeds, Leeds, UK

³⁰ International Institute for Applied Systems Analysis (IIASA), Schlossplatz 1 A-2361 Laxenburg, Austria

³¹ Research Institute for Environment, Energy, and Economics, Appalachian State University, Boone, North Carolina, USA

³² Flanders Marine Institute (VLIZ), InnovOceanSite, Wandelaarkaai 7, 8400 Ostend, Belgium

³³ Environmental Physics Group, ETH Zürich, Institute of Biogeochemistry and Pollutant Dynamics and Center for Climate Systems Modeling (C2SM), Zurich, Switzerland

³⁴ NCAS-Climate, Climatic Research Unit, School of Environmental Sciences, University of East Anglia, Norwich Research Park, Norwich, NR4 7TJ, UK

³⁵ Deutsches Zentrum für Luft- und Raumfahrt, Institut für Physik der Atmosphäre, Oberpfaffenhofen, Germany.

³⁶ Woods Hole Research Center (WHRC), Falmouth, MA 02540, USA

³⁷ Department of Atmospheric Sciences, University of Illinois, Urbana, IL 61821, USA

³⁸ CNRM, Université de Toulouse, Météo-France, CNRS, Toulouse, France

³⁹ Japan Meteorological Agency, 1-3-4 Otemachi, Chiyoda-Ku, Tokyo 100-8122, Japan

⁴⁰ Institute of Applied Energy (IAE), Minato-ku, Tokyo 105-0003, Japan

⁴¹ Plymouth Marine Laboratory (PML), Plymouth, PL13DH, United Kingdom

⁴² LOCEAN/IPSL laboratory, Sorbonne Université, CNRS/IRD/MNHN, Paris, France

⁴³ CSIRO Oceans and Atmosphere, Hobart, TAS, Australia

⁴⁴ Climate and Environmental Physics, Physics Institute and Oeschger Centre for Climate Change Research, University of Bern, Bern, Switzerland

⁴⁵ Department of Earth System Science, Tsinghua University, Beijing 100084, China

⁴⁶ National Center for Atmospheric Research, Climate and Global Dynamics, Terrestrial Sciences Section, Boulder, CO 80305, USA

⁴⁷ Department of Geological and Environmental Sciences, Appalachian State University, Boone, North Carolina, USA

12 Metzl⁴², David R. Munro^{48,49}, Julia E.M.S. Nabel¹¹, Shin-Ichiro Nakaoka²⁶, Yosuke Niwa^{26,50}, Kevin
13 O'Brien^{51,16}, Tsuneo Ono⁵², Paul I. Palmer^{53,54}, Denis Pierrot⁵⁵, Benjamin Poulter⁵⁶, Laure Resplandy⁵⁷,
14 Eddy Robertson⁵⁸, Christian Rödenbeck⁵⁹, Jörg Schwinger^{60,7}, Roland Séférian³⁸, Ingunn Skjelvan^{60,7},
15 Adam J.P. Smith³, Adrienne J. Sutton¹⁶, Toste Tanhua⁶¹, Pieter P. Tans⁶², Hanqin Tian⁶³, Bronte
16 Tilbrook^{43,64}, Guido van der Werf⁶⁵, Nicolas Vuichard¹⁴, Anthony P. Walker⁶⁶, Rik Wanninkhof⁶⁵, Andrew
17 J. Watson¹², David Willis⁶⁷, Andrew J. Wiltshire⁵⁸, Wenping Yuan⁶⁸, Xu Yue⁶⁹, Sönke Zaehle⁵⁹
18
19

⁴⁸ Cooperative Institute for Research in Environmental Sciences, University of Colorado,
Boulder, CO, 80305, USA

⁴⁹ National Oceanic & Atmospheric Administration/Global Monitoring Laboratory
(NOAA/GML), Boulder, CO, 80305, USA

⁵⁰ Meteorological Research Institute, 1-1 Nagamine, Tsukuba, Ibaraki, 305-0052 Japan

⁵¹ Cooperative Institute for Climate, Ocean and Ecosystem Studies (CICOES), University of
Washington, Seattle, WA, USA

⁵² Japan Fisheries Research and Education Agency, 2-12-4 Fukuura, Kanazawa-Ku, Yokohama
236-8648, Japan

⁵³ National Centre for Earth Observation, University of Edinburgh, UK

⁵⁴ School of GeoSciences, University of Edinburgh, UK

⁵⁵ National Oceanic & Atmospheric Administration/Atlantic Oceanographic & Meteorological
Laboratory (NOAA/AOML), Miami, FL 33149, USA

⁵⁶ NASA Goddard Space Flight Center, Biospheric Sciences Laboratory, Greenbelt,
Maryland 20771, USA

⁵⁷ Princeton University, Department of Geosciences and Princeton Environmental Institute,
Princeton, NJ, USA

⁵⁸ Met Office Hadley Centre, FitzRoy Road, Exeter EX1 3PB, UK

⁵⁹ Max Planck Institute for Biogeochemistry, P.O. Box 600164, Hans-Knöll-Str. 10, 07745 Jena,
Germany

⁶⁰ NORCE Norwegian Research Centre, Jahnebakken 5, 5007 Bergen, Norway

⁶¹ GEOMAR Helmholtz Centre for Ocean Research Kiel, Düsternbrooker Weg 20, 24105 Kiel,
Germany

⁶² National Oceanic & Atmospheric Administration, Earth System Research Laboratory
(NOAA ESRL), Boulder, CO 80305, USA

⁶³ School of Forestry and Wildlife Sciences, Auburn University, 602 Duncan Drive,
Auburn, AL 36849, USA

⁶⁴ Australian Antarctic Partnership Program, University of Tasmania, Hobart, Australia

⁶⁵ Faculty of Science, Vrije Universiteit, Amsterdam, the Netherlands

⁶⁶ Climate Change Science Institute & Environmental Sciences Division, Oak Ridge
National Lab

⁶⁷ University of East Anglia, Norwich Research Park, Norwich NR4 7TJ, UK

⁶⁸ School of Atmospheric Sciences, Guangdong Province Key Laboratory for Climate
Change and Natural Disaster Studies, Zhuhai Key Laboratory of Dynamics Urban Climate
and Ecology, Sun Yat-sen University, Zhuhai, Guangdong 510245, China.

⁶⁹ Jiangsu Key Laboratory of Atmospheric Environment Monitoring and Pollution
Control, Collaborative Innovation Center of Atmospheric Environment and Equipment
Technology, School of Environmental Science and Engineering, Nanjing University of
Information Science & Technology (NUIST), Nanjing, 210044, China

20
21
22
23
24
25
26
27
28
29
30
31
32
33
34
35
36
37
38
39
40

Correspondence: Pierre Friedlingstein (p.friedlingstein@exeter.ac.uk)

41 **Abstract**

42 Accurate assessment of anthropogenic carbon dioxide (CO₂) emissions and their redistribution
43 among the atmosphere, ocean, and terrestrial biosphere in a changing climate – the ‘global
44 carbon budget’ – is important to better understand the global carbon cycle, support the
45 development of climate policies, and project future climate change. Here we describe data sets
46 and methodology to quantify the five major components of the global carbon budget and their
47 uncertainties. Fossil CO₂ emissions (E_{FOS}) are based on energy statistics and cement production
48 data, while emissions from land-use change (E_{LUC}), mainly deforestation, are based on land-use
49 and land-use change data and bookkeeping models. Atmospheric CO₂ concentration is
50 measured directly and its growth rate (G_{ATM}) is computed from the annual changes in
51 concentration. The ocean CO₂ sink (S_{OCEAN}) and terrestrial CO₂ sink (S_{LAND}) are estimated with
52 global process models constrained by observations. The resulting carbon budget imbalance
53 (B_{IM}), the difference between the estimated total emissions and the estimated changes in the
54 atmosphere, ocean, and terrestrial biosphere, is a measure of imperfect data and
55 understanding of the contemporary carbon cycle. All uncertainties are reported as ±1σ. For the
56 last decade available (2010-2019), E_{FOS} was 9.4 ± 0.5 GtC yr⁻¹, E_{LUC} 1.6 ± 0.7 GtC yr⁻¹, G_{ATM} 5.1 ±
57 0.02 GtC yr⁻¹ (2.4 ± 0.01 ppm yr⁻¹), S_{OCEAN} 2.5 ± 0.6 GtC yr⁻¹, and S_{LAND} 3.4 ± 0.9 GtC yr⁻¹, with a
58 budget imbalance B_{IM} of -0.1 GtC yr⁻¹ indicating a near balance between estimated sources and
59 sinks over the last decade. For year 2019 alone, the growth in E_{FOS} was only about 0.1% with
60 fossil emissions increasing to 9.7 ± 0.5 GtC yr⁻¹, E_{LUC} was 1.8 ± 0.7 GtC yr⁻¹, for a total
61 anthropogenic CO₂ emissions of 11.5 ± 0.9 GtC yr⁻¹ (42.2 ± 3.3 GtCO₂). Also for 2019, G_{ATM} was
62 5.4 ± 0.2 GtC yr⁻¹ (2.5 ± 0.1 ppm yr⁻¹), S_{OCEAN} was 2.6 ± 0.6 GtC yr⁻¹ and S_{LAND} was 3.1 ± 1.2 GtC yr⁻¹,
63 with a B_{IM} of 0.3 GtC. The global atmospheric CO₂ concentration reached 409.85 ± 0.1 ppm
64 averaged over 2019. Preliminary data for 2020, accounting for the COVID-19 induced changes in
65 emissions, suggest a decrease in E_{FOS} relative to 2019 of about -6% (median estimate, individual
66 estimates: -6%, -6%, -7%, -13%). Overall, the mean and trend in the components of the global
67 carbon budget are consistently estimated over the period 1959-2019, but discrepancies of up to
68 1 GtC yr⁻¹ persist for the representation of semi-decadal variability in CO₂ fluxes. Comparison of
69 estimates from diverse approaches and observations shows: (1) no consensus in the mean and
70 trend in land-use change emissions over the last decade, (2) a persistent low agreement
71 between the different methods on the magnitude of the land CO₂ flux in the northern extra-
72 tropics, and (3) an apparent discrepancy between the different methods on the ocean sink
73 outside the tropics, particularly in the Southern Ocean. This living data update documents
74 changes in the methods and data sets used in this new global carbon budget and the progress
75 in understanding of the global carbon cycle compared with previous publications of this data
76 set (Friedlingstein et al., 2019; Le Quéré et al., 2018b, 2018a, 2016, 2015b, 2015a, 2014, 2013).
77 The data generated by this work are available at <https://doi.org/10.18160/gcp-2020>
78 (Friedlingstein et al., 2020).

79 **1 Introduction**

80 The concentration of carbon dioxide (CO₂) in the atmosphere has increased from approximately
81 277 parts per million (ppm) in 1750 (Joos and Spahni, 2008), the beginning of the Industrial Era,
82 to 409.85 ± 0.1 ppm in 2019 (Dlugokencky and Tans, 2020); Fig. 1). The atmospheric CO₂
83 increase above pre-industrial levels was, initially, primarily caused by the release of carbon to

84 the atmosphere from deforestation and other land-use change activities (Ciais et al., 2013).
85 While emissions from fossil fuels started before the Industrial Era, they only became the
86 dominant source of anthropogenic emissions to the atmosphere from around 1950 and their
87 relative share has continued to increase until present. Anthropogenic emissions occur on top of
88 an active natural carbon cycle that circulates carbon between the reservoirs of the atmosphere,
89 ocean, and terrestrial biosphere on time scales from sub-daily to millennia, while exchanges
90 with geologic reservoirs occur at longer timescales (Archer et al., 2009).

91 The global carbon budget presented here refers to the mean, variations, and trends in the
92 perturbation of CO₂ in the environment, referenced to the beginning of the Industrial Era
93 (defined here as 1750). This paper describes the components of the global carbon cycle over
94 the historical period with a stronger focus on the recent period (since 1958, onset of
95 atmospheric CO₂ measurements), the last decade (2010-2019), the last year (2019) and the
96 current year (2020). We quantify the input of CO₂ to the atmosphere by emissions from human
97 activities, the growth rate of atmospheric CO₂ concentration, and the resulting changes in the
98 storage of carbon in the land and ocean reservoirs in response to increasing atmospheric CO₂
99 levels, climate change and variability, and other anthropogenic and natural changes (Fig. 2). An
100 understanding of this perturbation budget over time and the underlying variability and trends
101 of the natural carbon cycle is necessary to understand the response of natural sinks to changes
102 in climate, CO₂ and land-use change drivers, and the permissible emissions for a given climate
103 stabilization target. Note that this paper does not estimate the remaining future carbon
104 emissions consistent with a given climate target (often referred to as the remaining carbon
105 budget (Millar et al., 2017; Rogelj et al., 2016, 2019).

106 The components of the CO₂ budget that are reported annually in this paper include separate
107 estimates for the CO₂ emissions from (1) fossil fuel combustion and oxidation from all energy
108 and industrial processes; also including cement production and carbonation (E_{FOS} ; GtC yr⁻¹) and
109 (2) the emissions resulting from deliberate human activities on land, including those leading to
110 land-use change (E_{LUC} ; GtC yr⁻¹); and their partitioning among (3) the growth rate of
111 atmospheric CO₂ concentration (G_{ATM} ; GtC yr⁻¹), and the uptake of CO₂ (the 'CO₂ sinks') in (4)
112 the ocean (S_{OCEAN} ; GtC yr⁻¹) and (5) on land (S_{LAND} ; GtC yr⁻¹). The CO₂ sinks as defined here
113 conceptually include the response of the land (including inland waters and estuaries) and ocean
114 (including coasts and territorial sea) to elevated CO₂ and changes in climate, rivers, and other

115 environmental conditions, although in practice not all processes are fully accounted for (see
116 Section 2.7). The global emissions and their partitioning among the atmosphere, ocean and
117 land are in reality in balance, however due to imperfect spatial and/or temporal data coverage,
118 errors in each estimate, and smaller terms not included in our budget estimate (discussed in
119 Section 2.7), their sum does not necessarily add up to zero. We estimate a budget imbalance
120 (B_{IM}), which is a measure of the mismatch between the estimated emissions and the estimated
121 changes in the atmosphere, land and ocean, with the full global carbon budget as follows:

$$122 \quad E_{FOS} + E_{LUC} = G_{ATM} + S_{OCEAN} + S_{LAND} + B_{IM} \quad (1)$$

123 G_{ATM} is usually reported in ppm yr⁻¹, which we convert to units of carbon mass per year, GtC yr⁻¹,
124 using 1 ppm = 2.124 GtC (Ballantyne et al., 2012; Table 1). All quantities are presented in units
125 of gigatonnes of carbon (GtC, 10¹⁵ gC), which is the same as petagrams of carbon (PgC; Table 1).
126 Units of gigatonnes of CO₂ (or billion tonnes of CO₂) used in policy are equal to 3.664 multiplied
127 by the value in units of GtC.

128

129 We also include a quantification of E_{FOS} by country, computed with both territorial and
130 consumption-based accounting (see Section 2), and discuss missing terms from sources other
131 than the combustion of fossil fuels (see Section 2.7).

132 The CO₂ budget has been assessed by the Intergovernmental Panel on Climate Change (IPCC) in
133 all assessment reports (Prentice et al., 2001; Schimel et al., 1995; Watson et al., 1990; Denman
134 et al., 2007; Ciais et al., 2013), and by others (e.g. Ballantyne et al., 2012). The IPCC
135 methodology has been revised and used by the Global Carbon Project (GCP,
136 www.globalcarbonproject.org, last access: 27 September 2020), which has coordinated this
137 cooperative community effort for the annual publication of global carbon budgets for the year
138 2005 (Raupach et al., 2007; including fossil emissions only), year 2006 (Canadell et al., 2007),
139 year 2007 (published online; GCP, 2007), year 2008 (Le Quéré et al., 2009), year 2009
140 (Friedlingstein et al., 2010), year 2010 (Peters et al., 2012b), year 2012 (Le Quéré et al., 2013;
141 Peters et al., 2013), year 2013 (Le Quéré et al., 2014), year 2014 (Le Quéré et al., 2015a;
142 Friedlingstein et al., 2014), year 2015 (Jackson et al., 2016; Le Quéré et al., 2015b), year 2016
143 (Le Quéré et al., 2016), year 2017 (Le Quéré et al., 2018a; Peters et al., 2017), year 2018 (Le
144 Quéré et al., 2018b; Jackson et al., 2018) and most recently the year 2019 (Friedlingstein et al.,

145 2019; Jackson et al., 2019; Peters et al., 2019). Each of these papers updated previous estimates
146 with the latest available information for the entire time series.

147 We adopt a range of ± 1 standard deviation (σ) to report the uncertainties in our estimates,
148 representing a likelihood of 68% that the true value will be within the provided range if the
149 errors have a Gaussian distribution and no bias is assumed. This choice reflects the difficulty of
150 characterising the uncertainty in the CO₂ fluxes between the atmosphere and the ocean and
151 land reservoirs individually, particularly on an annual basis, as well as the difficulty of updating
152 the CO₂ emissions from land-use change. A likelihood of 68% provides an indication of our
153 current capability to quantify each term and its uncertainty given the available information. For
154 comparison, the Fifth Assessment Report of the IPCC (AR5) generally reported a likelihood of
155 90% for large data sets whose uncertainty is well characterised, or for long time intervals less
156 affected by year-to-year variability. Our 68% uncertainty value is near the 66% which the IPCC
157 characterises as ‘likely’ for values falling into the $\pm 1\sigma$ interval. The uncertainties reported here
158 combine statistical analysis of the underlying data and expert judgement of the likelihood of
159 results lying outside this range. The limitations of current information are discussed in the
160 paper and have been examined in detail elsewhere (Ballantyne et al., 2015; Zscheischler et al.,
161 2017). We also use a qualitative assessment of confidence level to characterise the annual
162 estimates from each term based on the type, amount, quality and consistency of the evidence
163 as defined by the IPCC (Stocker et al., 2013).

164 This paper provides a detailed description of the data sets and methodology used to compute
165 the global carbon budget estimates for the industrial period, from 1750 to 2019, and in more
166 detail for the period since 1959. It also provides decadal averages starting in 1960 including the
167 last decade (2010-2019), results for the year 2019, and a projection for the year 2020. Finally it
168 provides cumulative emissions from fossil fuels and land-use change since the year 1750, the
169 pre-industrial period; and since the year 1850, the reference year for historical simulations in
170 IPCC (AR6). This paper is updated every year using the format of ‘living data’ to keep a record of
171 budget versions and the changes in new data, revision of data, and changes in methodology
172 that lead to changes in estimates of the carbon budget. Additional materials associated with
173 the release of each new version will be posted at the Global Carbon Project (GCP) website
174 (<http://www.globalcarbonproject.org/carbonbudget>, last access: 27 September 2020), with
175 fossil fuel emissions also available through the Global Carbon Atlas

176 (<http://www.globalcarbonatlas.org>, last access: 27 September 2020). With this approach, we
177 aim to provide the highest transparency and traceability in the reporting of CO₂, the key driver
178 of climate change.

179 **2 Methods**

180 Multiple organizations and research groups around the world generated the original
181 measurements and data used to complete the global carbon budget. The effort presented here
182 is thus mainly one of synthesis, where results from individual groups are collated, analysed and
183 evaluated for consistency. We facilitate access to original data with the understanding that
184 primary data sets will be referenced in future work (see Table 2 for how to cite the data sets).
185 Descriptions of the measurements, models, and methodologies follow below and detailed
186 descriptions of each component are provided elsewhere.

187 This is the 15th version of the global carbon budget and the ninth revised version in the format
188 of a living data update in Earth System Science Data. It builds on the latest published global
189 carbon budget of Friedlingstein et al. (2019). The main changes are: (1) the inclusion of data to
190 year 2019 and a projection for the global carbon budget for year 2020; (2) the inclusion of gross
191 carbon fluxes associated with land use changes; and (3) the inclusion of cement carbonation in
192 the fossil fuel and cement component of the budget (E_{FOS}). The main methodological
193 differences between recent annual carbon budgets (2015-2019) are summarised in Table 3 and
194 previous changes since 2006 are provided in Table A7.

195 **2.1 Fossil CO₂ emissions (E_{FOS})**

196 **2.1.1 Emissions estimates**

197 The estimates of global and national fossil CO₂ emissions (E_{FOS}) include the combustion of fossil
198 fuels through a wide range of activities (e.g. transport, heating and cooling, industry, fossil
199 industry own use & natural gas flaring), the production of cement, and other process emissions
200 (e.g. the production of chemicals & fertilizers) as well as CO₂ uptake during the cement
201 carbonation process. The estimates of E_{FOS} rely primarily on energy consumption data,
202 specifically data on hydrocarbon fuels, collated and archived by several organisations (Andres et
203 al., 2012; Andrew, 2020a). We use four main data sets for historical emissions (1750-2019):

- 204 1. Global and national emission estimates for coal, oil, natural gas as well as peat fuel
205 extraction from CDIAC for the time period 1750-2017 (Gilfillan et al., 2020), as it is the only
206 data set that extends back to 1750 by country.
- 207 2. Official UNFCCC national inventory reports annually for 1990-2018 for the 42 Annex I
208 countries in the UNFCCC (UNFCCC, 2020). We assess these to be the most accurate
209 estimates because they are compiled by experts within countries that have access to the
210 most detailed data, and they are periodically reviewed.
- 211 3. The BP Statistical Review of World Energy (BP, 2020), as these are the most up-to-date
212 estimates of national energy statistics.
- 213 4. Global and national cement emissions updated from Andrew (2019) to include the latest
214 estimates of cement production and clinker ratios.

215 In the following section we provide more details for each data set and describe the additional
216 modifications that are required to make the data set consistent and usable.

217 *CDIAC*: The CDIAC estimates have been updated annually to the year 2017, derived primarily
218 from energy statistics published by the United Nations (UN, 2020). Fuel masses and volumes
219 are converted to fuel energy content using country-level coefficients provided by the UN, and
220 then converted to CO₂ emissions using conversion factors that take into account the
221 relationship between carbon content and energy (heat) content of the different fuel types
222 (coal, oil, natural gas, natural gas flaring) and the combustion efficiency (Marland and Rotty,
223 1984). Following Andrew (2020a), we make corrections to emissions from coal in the Soviet
224 Union during World War II, amounting to a cumulative reduction of 53 MtC over two years, and
225 corrections to emissions from oil in the Netherland Antilles and Aruba prior to 1950, amounting
226 to a cumulative reduction of 340 MtC over 23 years.

227 *UNFCCC*: Estimates from the UNFCCC national inventory reports follow the IPCC guidelines
228 (IPCC, 2006), but have a slightly larger system boundary than CDIAC by including emissions
229 coming from carbonates other than in cement manufacture. We reallocate the detailed
230 UNFCCC estimates to the CDIAC definitions of coal, oil, natural gas, cement, and other to allow
231 more consistent comparisons over time and between countries.

232 *Specific country updates: India*: The data reported by CDIAC for India are for the fiscal year
233 running from April to March (Andrew, 2020a), and various interannual variations in emissions
234 are not supported by official data. We therefore replace CDIAC estimates with calendar-year

235 estimates through 2019 by Andrew (2020b). Saudi Arabia: The 2019 edition of CDIAC
236 introduced what appear to be spurious interannual variations for this country (IEA, 2019),
237 therefore we use data from the 2018 global carbon budget (Le Quéré et al., 2018b). Norway:
238 CDIAC's method of apparent energy consumption results in large errors for Norway, and we
239 therefore overwrite emissions before 1990 with estimates derived from official Norwegian
240 statistics.

241 *BP*: For the most recent year(s) when the UNFCCC and CDIAC estimates are yet not available,
242 we generate preliminary estimates using energy consumption data from the BP Statistical
243 Review of World Energy (Andres et al., 2014; BP, 2020; Myhre et al., 2009). We apply the BP
244 growth rates by fuel type (coal, oil, natural gas) to estimate 2019 emissions based on 2018
245 estimates (UNFCCC Annex I countries), and to estimate 2018-2019 emissions based on 2017
246 estimates (remaining countries except India). BP's dataset explicitly covers about 70 countries
247 (96% of global energy emissions), and for the remaining countries we use growth rates from the
248 sub-region the country belongs to. For the most recent years, natural gas flaring is assumed
249 constant from the most recent available year of data (2018 for Annex I countries, 2017 for the
250 remainder). We apply one exception to this update using BP data, and that is for China's coal
251 emissions, for which we rely on more recent official data (NBS, 2020b).

252 *Cement*: Estimates of emissions from cement production are updated from Andrew (2019).
253 Other carbonate decomposition processes are not included explicitly here, except in national
254 inventories provided by Annex I countries, but are discussed in Section 2.7.2.

255 *Country mappings*: The published CDIAC data set includes 257 countries and regions. This list
256 includes countries that no longer exist, such as the USSR and Yugoslavia. We reduce the list to
257 214 countries by reallocating emissions to currently defined territories, using mass-preserving
258 aggregation or disaggregation. Examples of aggregation include merging East and West
259 Germany to the currently defined Germany. Examples of disaggregation include reallocating the
260 emissions from the former USSR to the resulting independent countries. For disaggregation, we
261 use the emission shares when the current territories first appeared (e.g. USSR in 1992), and
262 thus historical estimates of disaggregated countries should be treated with extreme care. In the
263 case of the USSR, we were able to disaggregate 1990 and 1991 using data from the IEA. In
264 addition, we aggregate some overseas territories (e.g. Réunion, Guadeloupe) into their
265 governing nations (e.g. France) to align with UNFCCC reporting.

266 *Global total*: The global estimate is the sum of the individual countries' emissions and
267 international aviation and marine bunkers. The CDIAC global total differs to the sum of the
268 countries and bunkers since 1) the sum of imports in all countries is not equal to the sum of
269 exports because of reporting inconsistencies, 2) changes in stocks, and 3) the share of non-
270 oxidised carbon (e.g. as solvents, lubricants, feedstocks, etc.) at the global level is assumed to
271 be fixed at the 1970's average while it varies in the country level data based on energy data
272 (Andres et al., 2012). From the 2019 edition CDIAC now includes changes in stocks in the global
273 total (pers. comm., Dennis Gilfillan), removing one contribution to this discrepancy. The
274 discrepancy has grown over time from around zero in 1990 to over 500 MtCO₂ in recent years,
275 consistent with the growth in non-oxidised carbon (IEA, 2019). To remove this discrepancy we
276 now calculate the global total as the sum of the countries and international bunkers.

277
278 *Cement carbonation*: From the moment it is created, cement begins to gradually absorb CO₂
279 from the atmosphere, a process known as 'cement carbonation'. We estimate this CO₂ sink, as
280 the average of two studies in the literature (Cao et al., 2020; Guo et al., *submitted*). Both
281 studies use the same model, developed by Xi et al. (2016), with different parameterisations and
282 input data, with the estimate of Guo and colleagues being a revision of Xi et al (2016). The
283 trends of the two studies are very similar. Modelling cement carbonation requires estimation of
284 a large number of parameters, including the different types of cement material in different
285 countries, the lifetime of the structures before demolition, of cement waste after demolition,
286 and the volumetric properties of structures, among others (Xi et al., 2016). Lifetime is an
287 important parameter because demolition results in the exposure of new surfaces to the
288 carbonation process. The most significant reasons for differences between the two studies
289 appear to be the assumed lifetimes of cement structures and the geographic resolution, but the
290 uncertainty bounds of the two studies overlap. In the present budget, we include the cement
291 carbonation carbon sink in the fossil CO₂ emission component (E_{FOS}).

292 **2.1.2 Uncertainty assessment for E_{FOS}**

293 We estimate the uncertainty of the global fossil CO₂ emissions at ±5% (scaled down from the
294 published ±10 % at ±2σ to the use of ±1σ bounds reported here; Andres et al., 2012). This is
295 consistent with a more detailed analysis of uncertainty of ±8.4% at ±2σ (Andres et al., 2014) and
296 at the high-end of the range of ±5-10% at ±2σ reported by (Ballantyne et al., 2015). This

297 includes an assessment of uncertainties in the amounts of fuel consumed, the carbon and heat
298 contents of fuels, and the combustion efficiency. While we consider a fixed uncertainty of $\pm 5\%$
299 for all years, the uncertainty as a percentage of the emissions is growing with time because of
300 the larger share of global emissions from emerging economies and developing countries
301 (Marland et al., 2009). Generally, emissions from mature economies with good statistical
302 processes have an uncertainty of only a few per cent (Marland, 2008), while emissions from
303 developing countries such as China have uncertainties of around $\pm 10\%$ (for $\pm 1\sigma$; Gregg et al.,
304 2008). Uncertainties of emissions are likely to be mainly systematic errors related to underlying
305 biases of energy statistics and to the accounting method used by each country.

306 We assign a medium confidence to the results presented here because they are based on
307 indirect estimates of emissions using energy data (Durant et al., 2011). There is only limited and
308 indirect evidence for emissions, although there is high agreement among the available
309 estimates within the given uncertainty (Andres et al., 2012, 2014), and emission estimates are
310 consistent with a range of other observations (Ciais et al., 2013), even though their regional and
311 national partitioning is more uncertain (Francey et al., 2013).

312 **2.1.3 Emissions embodied in goods and services**

313 CDIAC, UNFCCC, and BP national emission statistics 'include greenhouse gas emissions and
314 removals taking place within national territory and offshore areas over which the country has
315 jurisdiction' (Rypdal et al., 2006), and are called territorial emission inventories. Consumption-
316 based emission inventories allocate emissions to products that are consumed within a country,
317 and are conceptually calculated as the territorial emissions minus the 'embodied' territorial
318 emissions to produce exported products plus the emissions in other countries to produce
319 imported products (Consumption = Territorial – Exports + Imports). Consumption-based
320 emission attribution results (e.g. Davis and Caldeira, 2010) provide additional information to
321 territorial-based emissions that can be used to understand emission drivers (Hertwich and
322 Peters, 2009) and quantify emission transfers by the trade of products between countries
323 (Peters et al., 2011b). The consumption-based emissions have the same global total, but reflect
324 the trade-driven movement of emissions across the Earth's surface in response to human
325 activities.

326 We estimate consumption-based emissions from 1990-2018 by enumerating the global supply
327 chain using a global model of the economic relationships between economic sectors within and

328 between every country (Andrew and Peters, 2013; Peters et al., 2011a). Our analysis is based
 329 on the economic and trade data from the Global Trade and Analysis Project (GTAP; Narayanan
 330 et al., 2015), and we make detailed estimates for the years 1997 (GTAP version 5), 2001
 331 (GTAP6), and 2004, 2007, and 2011 (GTAP9.2), covering 57 sectors and 141 countries and
 332 regions. The detailed results are then extended into an annual time-series from 1990 to the
 333 latest year of the Gross Domestic Product (GDP) data (2018 in this budget), using GDP data by
 334 expenditure in current exchange rate of US dollars (USD; from the UN National Accounts main
 335 Aggregates database; UN, 2019) and time series of trade data from GTAP (based on the
 336 methodology in Peters et al., 2011b). We estimate the sector-level CO₂ emissions using the
 337 GTAP data and methodology, include flaring and cement emissions from CDIAC, and then scale
 338 the national totals (excluding bunker fuels) to match the emission estimates from the carbon
 339 budget. We do not provide a separate uncertainty estimate for the consumption-based
 340 emissions, but based on model comparisons and sensitivity analysis, they are unlikely to be
 341 significantly different than for the territorial emission estimates (Peters et al., 2012a).

342 **2.1.4 Growth rate in emissions**

343 We report the annual growth rate in emissions for adjacent years (in percent per year) by
 344 calculating the difference between the two years and then normalising to the emissions in the
 345 first year: $(E_{FOS}(t_{0+1}) - E_{FOS}(t_0)) / E_{FOS}(t_0) \times 100\%$. We apply a leap-year adjustment where relevant to
 346 ensure valid interpretations of annual growth rates. This affects the growth rate by about 0.3%
 347 yr⁻¹ (1/366) and causes calculated growth rates to go up approximately 0.3% if the first year is a
 348 leap year and down 0.3% if the second year is a leap year.

349 The relative growth rate of E_{FOS} over time periods of greater than one year can be rewritten
 350 using its logarithm equivalent as follows:

$$351 \frac{1}{E_{FOS}} \frac{dE_{FOS}}{dt} = \frac{d(\ln E_{FOS})}{dt} \quad (2)$$

352 Here we calculate relative growth rates in emissions for multi-year periods (e.g. a decade) by
 353 fitting a linear trend to $\ln(E_{FOS})$ in Eq. (2), reported in percent per year.

354 **2.1.5 Emissions projections**

355 To gain insight on emission trends for 2020, we provide an assessment of global fossil CO₂
 356 emissions, E_{FOS} , by combining individual assessments of emissions for China, USA, the EU, and

357 India (the four countries/regions with the largest emissions), and the rest of the world. Our
358 analysis this year is different to previous editions of the Global Carbon Budget, as there have
359 been several independent studies estimating 2020 emissions in response to restrictions related
360 to the COVID-19 pandemic, and the highly unusual nature of the year makes the projection
361 much more difficult. We consider three separate studies, in addition to building on the method
362 used in our previous editions. We separate each method into two parts: first we estimate
363 emissions for the Year To Date (YTD) and, second, we project emissions for the rest of the year
364 2020. Each method is presented in the order it was published.

365 **2.1.5.1 UEA: Le Quéré et al. (2020)**

366
367 YTD: Le Quéré et al (2020) estimated the effect of COVID-19 on emissions using observed
368 changes in activity using proxy data for six sectors of the economy as a function of confinement
369 levels, scaled to the globe based on policy data in response to the pandemic. The analyses
370 employed baseline emissions by country for the latest year available (2018 or 2019) from the
371 Global Carbon Budget 2019 to estimate absolute emission changes and covered 67 countries
372 representing 97% of global emissions. Here we use an update to September. The parameters
373 for the changes in activity by sector were updated for the industry and aviation sectors, to
374 account for the slow recovery in these sectors observed since the first peak of the pandemic.
375 Specific country-based parameters were used for India and the US, which improved the match
376 to the observed monthly emissions (from Section 2.1.5.4). By design, this estimate does not
377 include the background seasonal variability in emissions (e.g. lower emissions in Northern
378 Hemisphere summer; Jones et al. in revision), nor the trends in emissions that would be caused
379 by other factors (e.g. reduced use of coal in the EU and the US).

380 Projection: A projection is used to fill the data from September to December, assuming
381 confinement measures currently in place are in place for six weeks before they ease in each
382 country.

383 **2.1.5.2 Priestley Centre: Forster et al. (2020)**

384 YTD: Forster et al. (2020) estimated YTD emissions based primarily on Google mobility data. The
385 mobility data were used to estimate daily fractional changes in emissions from power, surface
386 transport, industry, residential, and public and commercial sectors. The analyses employed
387 baseline emissions for 2019 from the Global Carbon Project to estimate absolute emission

388 changes and covered 123 countries representing over 99% of global emissions. For a few
389 countries - most notably China and Iran - Google data was not available and so data were
390 obtained from the high-reduction estimate from Le Quéré et al (2020). We use an updated
391 version of Forster et al (2020) in which emission-reduction estimates were extended through 5
392 September.

393 Projection: The estimates were projected from September to December with the assumption
394 that the declines in emissions from their baselines remain at 66% of the level over the last 30
395 days with estimates.

396 **2.1.5.3 Carbon Monitor: Liu et al. (2020)**

397 YTD: Liu et al (2020) estimated YTD emissions using emission data and emission proxy activity
398 data including hourly to daily electrical power generation data and carbon emission factors for
399 each different electricity sources from national electricity operation systems of 31 countries,
400 real-time mobility data (TomTom city congestion index data of 416 cities worldwide calibrated
401 to reproduce vehicle fluxes in one city and FlightRadar24 individual flight location data),
402 monthly industrial production data (calculated separately by cement production, steel
403 production, chemical production and other industrial production of 27 industries) or indices
404 (primarily Industrial Production Index) from national statistics of 62 countries and regions, and
405 monthly fuel consumption data corrected for the daily population-weighted air temperature in
406 206 countries using predefined heating and temperature functions from EDGAR for residential,
407 commercial and public buildings heating emissions, to finally calculate the global fossil CO₂
408 emissions, as well as the daily sectoral emissions from power sector, industry sector, transport
409 sector (including ground transport, aviation and shipping), and residential sector respectively.

410 Projection: Liu et al did not perform a projection and only presented YTD results. For purposes
411 of comparison with other methods, we use a simple approach to extrapolating their
412 observations by assuming the remaining months of the year change by the same relative
413 amount compared to 2019 in the final month of observations.

414 **2.1.5.4 Global Carbon Budget Estimates**

415 Previous editions of the Global Carbon Budget (GCB) have estimated YTD emissions, and
416 performed projections, using sub-annual energy consumption data from a variety of sources
417 depending on the country or region. The YTD estimates have then been projected to the full
418 year using specific methods for each country or region. This year we make some adjustments to
419 this approach, as described below, with detailed descriptions provided in Appendix C.

420 China: There is no YTD estimate, with the projection based on the relationship between
421 previous monthly data and full year data to extend the 2020 monthly data to estimate full year
422 emissions.

423 USA: The YTD and projection are taken directly from the US Energy Information Agency.

424 EU27: The YTD estimates are based on monthly consumption data of coal, oil, and gas
425 converted to CO₂ and scaled to match previous year emissions. We use the same method for
426 the EU27 as for Carbon Monitor to generate a full-year projection.

427 India: YTD estimates are updated from Andrew (2020), which calculates monthly emissions
428 directly from energy and cement production data. We use the same method for India as for
429 Carbon Monitor to generate a full-year projection.

430 Rest of World: There is no YTD estimate, while the 2020 projection is based on a GDP estimate
431 from the IMF combined with average improvements in carbon intensity observed in the last 10
432 years, as in previous editions of the Global Carbon Budget (e.g. Friedlingstein et al. 2019).

433 **2.1.5.5 Synthesis**

434 In the results section we present the estimates from the four different methods, showing the
435 YTD estimates to the last common historical data point in each dataset and the projections for
436 2020.

437 **2.2 CO₂ emissions from land-use, land-use change and forestry (E_{LUC})**

438 The net CO₂ flux from land-use, land-use change and forestry (E_{LUC}, called land-use change
439 emissions in the rest of the text) includes CO₂ fluxes from deforestation, afforestation, logging
440 and forest degradation (including harvest activity), shifting cultivation (cycle of cutting forest for
441 agriculture, then abandoning), and regrowth of forests following wood harvest or
442 abandonment of agriculture. Emissions from peat burning and drainage are added from
443 external datasets (see 2.2.1). Only some land-management activities are included in our land-
444 use change emissions estimates (Table A1). Some of these activities lead to emissions of CO₂ to
445 the atmosphere, while others lead to CO₂ sinks. E_{LUC} is the net sum of emissions and removals
446 due to all anthropogenic activities considered. Our annual estimate for 1959-2019 is provided
447 as the average of results from three bookkeeping approaches (Section 2.2.1): an estimate using
448 the Bookkeeping of Land Use Emissions model (Hansis et al., 2015; hereafter BLUE), the
449 estimate published by (Houghton and Nassikas, 2017; hereafter H&N2017) and the estimate

450 published by Gasser et al. (2020) using the compact Earth system model OSCAR, the latter two
451 updated to 2019. All three data sets are then extrapolated to provide a projection for 2020
452 (Section 2.2.4). In addition, we use results from Dynamic Global Vegetation Models (DGVMs;
453 see Section 2.2.2 and Table 4) to help quantify the uncertainty in E_{LUC} (Section 2.2.3), and thus
454 better characterise our understanding.

455 **2.2.1 Bookkeeping models**

456 Land-use change CO_2 emissions and uptake fluxes are calculated by three bookkeeping models.
457 These are based on the original bookkeeping approach of Houghton (2003) that keeps track of
458 the carbon stored in vegetation and soils before and after a land-use change (transitions
459 between various natural vegetation types, croplands and pastures). Literature-based response
460 curves describe decay of vegetation and soil carbon, including transfer to product pools of
461 different lifetimes, as well as carbon uptake due to regrowth. In addition, the bookkeeping
462 models represent long-term degradation of primary forest as lowered standing vegetation and
463 soil carbon stocks in secondary forests, and also include forest management practices such as
464 wood harvests.

465 BLUE and H&N2017 exclude land ecosystems' transient response to changes in climate,
466 atmospheric CO_2 and other environmental factors, and base the carbon densities on
467 contemporary data from literature and inventory data. Since carbon densities thus remain fixed
468 over time, the additional sink capacity that ecosystems provide in response to CO_2 -fertilization
469 and some other environmental changes is not captured by these models (Pongratz et al., 2014).
470 On the contrary, OSCAR includes this transient response, and it follows a theoretical framework
471 (Gasser and Ciais, 2013) that allows separating bookkeeping land-use emissions and the loss of
472 additional sink capacity. Only the former is included here, while the latter is discussed in
473 Section 2.7.4. The bookkeeping models differ in (1) computational units (spatially explicit
474 treatment of land-use change for BLUE, country-level for H&N2017, 10 regions and 5 biomes
475 for OSCAR), (2) processes represented (see Table A1), and (3) carbon densities assigned to
476 vegetation and soil of each vegetation type (literature-based for H&N2017 and BLUE, calibrated
477 to DGVMs for OSCAR). A notable change of H&N2017 over the original approach by Houghton
478 (2003) used in earlier budget estimates is that no shifting cultivation or other back- and forth-
479 transitions at a level below country are included. Only a decline in forest area in a country as
480 indicated by the Forest Resource Assessment of the FAO that exceeds the expansion of

481 agricultural area as indicated by FAO is assumed to represent a concurrent expansion and
482 abandonment of cropland. In contrast, the BLUE and OSCAR models include sub-grid-scale
483 transitions between all vegetation types). Furthermore, H&N2017 assume conversion of natural
484 grasslands to pasture, while BLUE and OSCAR allocates pasture proportionally on all natural
485 vegetation that exists in a grid-cell. This is one reason for generally higher emissions in BLUE
486 and OSCAR. Bookkeeping models do not directly capture carbon emissions from peat fires,
487 which can create large emissions and interannual variability due to synergies of land-use and
488 climate variability in Southeast Asia, in particular during El-Niño events, nor emissions from the
489 organic layers of drained peat soils. To correct for this, H&N2017 includes carbon emissions
490 from peat burning based on the Global Fire Emission Database (GFED4s; van der Werf et al.,
491 2017), and peat drainage based on estimates by Hooijer et al. (2010) for Indonesia and
492 Malaysia. We add GFED4s peat fire emissions to BLUE and OSCAR output, but use the newly
493 published global FAO peat drainage emissions 1990-2018 from croplands and grasslands
494 (<http://www.fao.org/faostat/en>). We linearly increase tropical drainage emissions from 0 in
495 1980, consistent with H&N2017's assumption, and keep emissions from the often old drained
496 areas of the extratropics constant pre-1990. This adds 8.6 GtC 1960-2019 for FAO compared to
497 5.4 GtC for Hooijer et al. (2010). Peat fires add another 2.0 GtC over the same period.

498 The three bookkeeping estimates used in this study differ with respect to the land-use change
499 data used to drive the models. H&N2017 base their estimates directly on the Forest Resource
500 Assessment of the FAO which provides statistics on forest-area change and management at
501 intervals of five years currently updated until 2015 (FAO, 2015). The data is based on country
502 reporting to FAO, and may include remote-sensing information in more recent assessments.
503 Changes in land-use other than forests are based on annual, national changes in cropland and
504 pasture areas reported by FAO (FAOSTAT, 2015). On the other hand, BLUE uses the harmonised
505 land-use change data LUH2 covering the entire 850-2019 period
506 (<https://doi.org/10.22033/ESGF/input4MIPs.1127>; Hurtt et al., 2020), which was also used as
507 input to the DGVMs (Sec. 2.2.2). It describes land-use change, also based on the FAO data as
508 well as the HYDE dataset (Goldewijk et al., 2017a, 2017b), but downscaled at a quarter-degree
509 spatial resolution, considering sub-grid-scale transitions between primary forest, secondary
510 forest, cropland, pasture and rangeland. The LUH2 data provides a distinction between
511 rangelands and pasture, based on inputs from HYDE. To constrain the models' interpretation on
512 whether rangeland implies the original natural vegetation to be transformed to grassland or not

513 (e.g., browsing on shrubland), a forest mask was provided with LUH2; forest is assumed to be
514 transformed to grasslands, while other natural vegetation remains (in case of secondary
515 vegetation) or is degraded from primary to secondary vegetation (Ma et al., 2020). This is
516 implemented in BLUE. OSCAR was run with both LUH2 850-2018 (as used in Friedlingstein et al.,
517 2019) and FAO/FRA, where the latter was extended beyond 2015 with constant 2011-2015
518 average values. The best-guess OSCAR estimate used in our study is a combination of results for
519 LUH2 and FAO/FRA land-use data and a large number of perturbed parameter simulations
520 weighted against an observational constraint. H&N2017 was extended here for 2016 to 2019 by
521 adding the annual change in total tropical emissions to the H&N2017 estimate for 2015,
522 including estimates of peat drainage and peat burning as described above as well as emissions
523 from tropical deforestation and degradation fires from GFED4.1s (van der Werf et al., 2017).
524 Similarly, OSCAR was extended from 2018 to 2019. Gross fluxes for H&N2017 and OSCAR were
525 extended to 2019 based on a regression of gross sources (including peat emissions) to net
526 emissions for recent years. BLUE's 2019 value was adjusted because the LUH2 forcing for 2019
527 was an extrapolation of earlier years, thus not capturing the rising deforestation rates occurring
528 in South America in 2019 and the anomalous fire season in Southeast Asia. GFED tropical
529 deforestation and degradation anomalies relative to 2018 are therefore added. Resulting
530 dynamics in the Amazon are consistent with BLUE simulations using directly observed forest
531 cover loss and forest alert data (Hansen et al., 2013; Hansen et al., 2016).

532 For E_{LUC} from 1850 onwards we average the estimates from BLUE, H&N2017 and OSCAR. For
533 the cumulative numbers starting 1750 an average of four earlier publications is added (30 ± 20
534 PgC 1750-1850, rounded to nearest 5; Le Quéré et al., 2016).

535 **2.2.2 Dynamic Global Vegetation Models (DGVMs)**

536 Land-use change CO_2 emissions have also been estimated using an ensemble of 17 DGVM
537 simulations. The DGVMs account for deforestation and regrowth, the most important
538 components of E_{LUC} , but they do not represent all processes resulting directly from human
539 activities on land (Table A1). All DGVMs represent processes of vegetation growth and
540 mortality, as well as decomposition of dead organic matter associated with natural cycles, and
541 include the vegetation and soil carbon response to increasing atmospheric CO_2 concentration
542 and to climate variability and change. Some models explicitly simulate the coupling of carbon
543 and nitrogen cycles and account for atmospheric N deposition and N fertilisers (Table A1). The

544 DGVMs are independent from the other budget terms except for their use of atmospheric CO₂
545 concentration to calculate the fertilization effect of CO₂ on plant photosynthesis.

546 Many DGVMs used the HYDE land-use change data set (Goldewijk et al., 2017a, 2017b), which
547 provides annual (1700-2019), half-degree, fractional data on cropland and pasture. The data are
548 based on the available annual FAO statistics of change in agricultural land area available until
549 2015. HYDE version 3.2 used FAO statistics until 2012, which were supplemented using the
550 annual change anomalies from FAO data for years 2013-2015 relative to year 2012. HYDE
551 forcing was also corrected for Brazil for years 1951-2012. After the year 2015 HYDE
552 extrapolates cropland, pasture, and urban land-use data until the year 2019. Some models also
553 use the LUH2 data set, an update of the more comprehensive harmonised land-use data set
554 (Hurtt et al., 2011), that further includes fractional data on primary and secondary forest
555 vegetation, as well as all underlying transitions between land-use states (1700-2019)
556 (<https://doi.org/10.22033/ESGF/input4MIPs.1127>; Hurtt et al., 2011; Hurtt et al., 2020; Table
557 A1). This new data set is of quarter degree fractional areas of land-use states and all transitions
558 between those states, including a new wood harvest reconstruction, new representation of
559 shifting cultivation, crop rotations, management information including irrigation and fertilizer
560 application. The land-use states include five different crop types in addition to the pasture-
561 rangeland split discussed before. Wood harvest patterns are constrained with Landsat-based
562 tree cover loss data (Hansen et al. 2013). Updates of LUH2 over last year's version are using the
563 most recent HYDE/FAO release (covering the time period up to including 2015), which also
564 corrects an error in the version used for the 2018 budget in Brazil. The FAO wood harvest data
565 has changed for the years 2015 onwards and so those are now being used in this year's LUH-
566 GCB dataset. This means the LUH-GCB data is identical to last year's dataset for all years up to
567 2015 and differs slightly in terms of wood harvest and resulting secondary area/age/biomass
568 for years after 2015.

569

570 DGVMs implement land-use change differently (e.g. an increased cropland fraction in a grid cell
571 can either be at the expense of grassland or shrubs, or forest, the latter resulting in
572 deforestation; land cover fractions of the non-agricultural land differ between models).

573 Similarly, model-specific assumptions are applied to convert deforested biomass or deforested

574 area, and other forest product pools into carbon, and different choices are made regarding the
575 allocation of rangelands as natural vegetation or pastures.

576 The DGVM model runs were forced by either the merged monthly CRU and 6 hourly JRA-55
577 data set or by the monthly CRU data set, both providing observation-based temperature,
578 precipitation, and incoming surface radiation on a 0.5°x0.5° grid and updated to 2019 (Harris et
579 al., 2014). The combination of CRU monthly data with 6 hourly forcing from JRA-55 (Kobayashi
580 et al., 2015) is performed with methodology used in previous years (Viogy, 2016) adapted to
581 the specifics of the JRA-55 data. The forcing data also include global atmospheric CO₂, which
582 changes over time (Dlugokencky and Tans, 2020), and gridded, time dependent N deposition
583 and N fertilisers (as used in some models; Table A1).

584 Two sets of simulations were performed with each of the DGVMs. Both applied historical
585 changes in climate, atmospheric CO₂ concentration, and N inputs. The two sets of simulations
586 differ, however, with respect to land-use: one set applies historical changes in land-use, the
587 other a time-invariant pre-industrial land cover distribution and pre-industrial wood harvest
588 rates. By difference of the two simulations, the dynamic evolution of vegetation biomass and
589 soil carbon pools in response to land-use change can be quantified in each model (E_{LUC}). Using
590 the difference between these two DGVM simulations to diagnose E_{LUC} means the DGVMs
591 account for the loss of additional sink capacity (around 0.4 ± 0.3 GtC yr⁻¹; see Section 2.7.4),
592 while the bookkeeping models do not.

593 As a criterion for inclusion in this carbon budget, we only retain models that simulate a positive
594 E_{LUC} during the 1990s, as assessed in the IPCC AR4 (Denman et al., 2007) and AR5 (Ciais et al.,
595 2013). All DGVMs met this criteria, although one model was not included in the E_{LUC} estimate
596 from DGVMs as it exhibited a spurious response to the transient land cover change forcing after
597 its initial spin-up.

598 **2.2.3 Uncertainty assessment for E_{LUC}**

599 Differences between the bookkeeping models and DGVM models originate from three main
600 sources: the different methodologies, which among others lead to inclusion of the loss of
601 additional sink capacity in DGVMs (Section 2.7.4), the underlying land-use/land cover data set,
602 and the different processes represented (Table A1). We examine the results from the DGVM

603 models and of the bookkeeping method, and use the resulting variations as a way to
604 characterise the uncertainty in E_{LUC} .

605 Despite these differences, the E_{LUC} estimate from the DGVMs multi-model mean is consistent
606 with the average of the emissions from the bookkeeping models (Table 5). However there are
607 large differences among individual DGVMs (standard deviation at around 0.5 GtC yr^{-1} ; Table 5),
608 between the bookkeeping estimates (average difference BLUE-HN2017 of 0.7 GtC yr^{-1} , BLUE-
609 OSCAR of 0.3 GtC yr^{-1} , OSCAR-HN2017 of 0.5 GtC yr^{-1}), and between the current estimate of
610 H&N2017 and its previous model version (Houghton et al., 2012). The uncertainty in E_{LUC} of ± 0.7
611 GtC yr^{-1} reflects our best value judgment that there is at least 68% chance ($\pm 1\sigma$) that the true
612 land-use change emission lies within the given range, for the range of processes considered
613 here. Prior to the year 1959, the uncertainty in E_{LUC} was taken from the standard deviation of
614 the DGVMs. We assign low confidence to the annual estimates of E_{LUC} because of the
615 inconsistencies among estimates and of the difficulties to quantify some of the processes in
616 DGVMs.

617 **2.2.4 Emissions projections for E_{LUC}**

618 We project the 2020 land-use emissions for BLUE, H&N2017 and OSCAR, starting from their
619 estimates for 2019 assuming unaltered peat drainage, which has low interannual variability,
620 and the highly variable emissions from peat fires, tropical deforestation and degradation as
621 estimated using active fire data (MCD14ML; Giglio et al., 2016). Those latter scale almost
622 linearly with GFED over large areas (van der Werf et al., 2017), and thus allows for tracking fire
623 emissions in deforestation and tropical peat zones in near-real time. During most years,
624 emissions during January-September cover most of the fire season in the Amazon and
625 Southeast Asia, where a large part of the global deforestation takes place and our estimates
626 capture emissions until September 14th. By then, 2020 emissions from deforestation and
627 degradation fires were still substantially lower than 2019. However, projections for the Amazon
628 expect about 50% higher deforestation by the end of 2020 than in 2019 (L. Aragão et al, pers.
629 comm.). We scale the 2019 Amazon fire emissions up by this factor for a preliminary 2020
630 projection. For the other tropical regions we add 20% to the 2020 Jan-Sep fire emissions to
631 capture the rest of the fire season. Together, this results in pantropical fire emissions of about
632 300 Tg C projected for 2020 as compared to 460 Tg C in 2019.

633 **2.3 Growth rate in atmospheric CO₂ concentration (G_{ATM})**

634 **2.3.1 Global growth rate in atmospheric CO₂ concentration**

635 The rate of growth of the atmospheric CO₂ concentration is provided by the US National
636 Oceanic and Atmospheric Administration Earth System Research Laboratory (NOAA/ESRL;
637 Dlugokencky and Tans, 2020), which is updated from Ballantyne et al. (2012). For the 1959-
638 1979 period, the global growth rate is based on measurements of atmospheric CO₂
639 concentration averaged from the Mauna Loa and South Pole stations, as observed by the CO₂
640 Program at Scripps Institution of Oceanography (Keeling et al., 1976). For the 1980-2019 time
641 period, the global growth rate is based on the average of multiple stations selected from the
642 marine boundary layer sites with well-mixed background air (Ballantyne et al., 2012), after
643 fitting each station with a smoothed curve as a function of time, and averaging by latitude band
644 (Masarie and Tans, 1995). The annual growth rate is estimated by Dlugokencky and Tans (2020)
645 from atmospheric CO₂ concentration by taking the average of the most recent December-
646 January months corrected for the average seasonal cycle and subtracting this same average one
647 year earlier. The growth rate in units of ppm yr⁻¹ is converted to units of GtC yr⁻¹ by multiplying
648 by a factor of 2.124 GtC per ppm (Ballantyne et al., 2012).

649 The uncertainty around the atmospheric growth rate is due to four main factors. First, the long-
650 term reproducibility of reference gas standards (around 0.03 ppm for 1σ from the 1980s;
651 Dlugokencky and Tans, 2020). Second, small unexplained systematic analytical errors that may
652 have a duration of several months to two years come and go. They have been simulated by
653 randomizing both the duration and the magnitude (determined from the existing evidence) in a
654 Monte Carlo procedure. Third, the network composition of the marine boundary layer with
655 some sites coming or going, gaps in the time series at each site, etc (Dlugokencky and Tans,
656 2020). The latter uncertainty was estimated by NOAA/ESRL with a Monte Carlo method by
657 constructing 100 "alternative" networks (Masarie and Tans, 1995; NOAA/ESRL, 2019). The
658 second and third uncertainties, summed in quadrature, add up to 0.085 ppm on average
659 (Dlugokencky and Tans, 2020). Fourth, the uncertainty associated with using the average CO₂
660 concentration from a surface network to approximate the true atmospheric average CO₂
661 concentration (mass-weighted, in 3 dimensions) as needed to assess the total atmospheric CO₂
662 burden. In reality, CO₂ variations measured at the stations will not exactly track changes in total
663 atmospheric burden, with offsets in magnitude and phasing due to vertical and horizontal

664 mixing. This effect must be very small on decadal and longer time scales, when the atmosphere
665 can be considered well mixed. Preliminary estimates suggest this effect would increase the
666 annual uncertainty, but a full analysis is not yet available. We therefore maintain an uncertainty
667 around the annual growth rate based on the multiple stations data set ranges between 0.11
668 and 0.72 GtC yr⁻¹, with a mean of 0.61 GtC yr⁻¹ for 1959-1979 and 0.17 GtC yr⁻¹ for 1980-2019,
669 when a larger set of stations were available as provided by Dlugokencky and Tans (2020), but
670 recognise further exploration of this uncertainty is required. At this time, we estimate the
671 uncertainty of the decadal averaged growth rate after 1980 at 0.02 GtC yr⁻¹ based on the
672 calibration and the annual growth rate uncertainty, but stretched over a 10-year interval. For
673 years prior to 1980, we estimate the decadal averaged uncertainty to be 0.07 GtC yr⁻¹ based on
674 a factor proportional to the annual uncertainty prior and after 1980 (0.02 * [0.61/0.17] GtC yr⁻¹).
675

676 We assign a high confidence to the annual estimates of G_{ATM} because they are based on direct
677 measurements from multiple and consistent instruments and stations distributed around the
678 world (Ballantyne et al., 2012).

679 In order to estimate the total carbon accumulated in the atmosphere since 1750 or 1850, we
680 use an atmospheric CO₂ concentration of 277 ± 3 ppm or 286 ± 3 ppm, respectively, based on a
681 cubic spline fit to ice core data (Joos and Spahni, 2008). The uncertainty of ±3 ppm (converted
682 to ±1σ) is taken directly from the IPCC's assessment (Ciais et al., 2013). Typical uncertainties in
683 the growth rate in atmospheric CO₂ concentration from ice core data are equivalent to ±0.1-
684 0.15 GtC yr⁻¹ as evaluated from the Law Dome data (Etheridge et al., 1996) for individual 20-
685 year intervals over the period from 1850 to 1960 (Bruno and Joos, 1997).

686 **2.3.2 Atmospheric growth rate projection**

687 We provide an assessment of G_{ATM} for 2020 based on the monthly calculated global
688 atmospheric CO₂ concentration (GLO) through July (Dlugokencky and Tans, 2020), and bias-
689 adjusted Holt–Winters exponential smoothing with additive seasonality (Chatfield, 1978) to
690 project to January 2021. Additional analysis suggests that the first half of the year shows more
691 interannual variability than the second half of the year, so that the exact projection method
692 applied to the second half of the year has a relatively smaller impact on the projection of the
693 full year. Uncertainty is estimated from past variability using the standard deviation of the last 5
694 years' monthly growth rates.

695 **2.4 Ocean CO₂ sink**

696 Estimates of the global ocean CO₂ sink S_{OCEAN} are from an ensemble of global ocean
697 biogeochemistry models (GOBMs, Table A2) that meet observational constraints over the 1990s
698 (see below). We use observation-based estimates of S_{OCEAN} to provide a qualitative assessment
699 of confidence in the reported results, and two diagnostic ocean models to estimate S_{OCEAN} over
700 the industrial era (see below).

701 **2.4.1 Observation-based estimates**

702 We primarily use the observational constraints assessed by IPCC of a mean ocean CO₂ sink of
703 $2.2 \pm 0.7 \text{ GtC yr}^{-1}$ for the 1990s (90% confidence interval; Denman et al., 2007, Ciais et al., 2013)
704 to verify that the GOBMs provide a realistic assessment of S_{OCEAN} . We further test that GOBMs
705 and data-products fall within the IPCC estimates for the 2000s ($2.3 \pm 0.7 \text{ GtC yr}^{-1}$), and the
706 period 2002-2011 ($2.4 \pm 0.7 \text{ GtC yr}^{-1}$, Ciais et al., 2013). The IPCC estimates are based on the
707 observational constraint of the mean 1990s sink and trends derived mainly from models and
708 one data-product (Ciais et al., 2013). This is based on indirect observations with seven different
709 methodologies and their uncertainties, using the methods that are deemed most reliable for
710 the assessment of this quantity (Denman et al., 2007; Ciais et al., 2013). The observation-based
711 estimates use the ocean/land CO₂ sink partitioning from observed atmospheric CO₂ and O₂/N₂
712 concentration trends (Manning and Keeling, 2006; updated in Keeling and Manning, 2014), an
713 oceanic inversion method constrained by ocean biogeochemistry data (Mikaloff Fletcher et al.,
714 2006), and a method based on penetration time scale for chlorofluorocarbons (McNeil et al.,
715 2003). The IPCC estimate of 2.2 GtC yr^{-1} for the 1990s is consistent with a range of methods
716 (Wanninkhof et al., 2013).

717 We also use five estimates of the ocean CO₂ sink and its variability based on interpolations of
718 measurements of surface ocean fugacity of CO₂ ($f\text{CO}_2$, which equals $p\text{CO}_2$ corrected for the non-
719 ideal behaviour of the gas; Pfeil et al., 2013). These estimates use different wind products and
720 gas-exchange formulations as specified in Table A3), and we refer to these as $p\text{CO}_2$ -based flux
721 estimates. The measurements are from the Surface Ocean CO₂ Atlas version 2020 (Bakker et
722 al., 2020), which is an update of version 3 (Bakker et al., 2016) and contains quality-controlled
723 data through 2019 (see data attribution Table A5). The SOCAT v2020 data were mapped using a
724 data-driven diagnostic method (Rödenbeck et al., 2013; referred to here as Jena-MLS), a
725 combined self-organising map and feed-forward neural network (Landschützer et al., 2014;

726 MPI-SOMFFN), an artificial neural network model (Denvil-Sommer et al., 2019; Copernicus
727 Marine Environment Monitoring Service (CMEMS)), an ensemble average of six machine
728 learning estimates of pCO₂ using a cluster regression approach (Gregor et al., 2019; CSIR).
729 Further, we use the flux estimate of Watson et al. (2020) that recalculated the SOCAT fCO₂
730 database adjusted to the subskin temperature of the ocean, and used the combined self-
731 organising map and feed-forward neural network (MPI-SOMFFN) to map the recalculated fCO₂
732 data. The Watson et al flux estimate also differs from the others by adjusting the flux to a cool,
733 salty ocean surface skin. The global pCO₂-based flux estimates were adjusted to remove the
734 pre-industrial ocean source of CO₂ to the atmosphere of 0.61 GtC yr⁻¹ from river input to the
735 ocean (the average of 0.45 ± 0.18 GtC yr⁻¹ by Jacobson et al (2007) and 0.78 ± 0.41 GtC yr⁻¹ by
736 Resplandy et al., 2018), to satisfy our definition of S_{OCEAN} (Hauck et al., 2020). The river flux
737 adjustment was distributed over the latitudinal bands using the regional distribution of Aumont
738 et al. (2001; North: 0.16 GtC yr⁻¹, Tropics: 0.15 GtC yr⁻¹, South: 0.30 GtC yr⁻¹). The CO₂ flux from
739 each pCO₂-based product is scaled by the ratio of the total ocean area covered by the
740 respective product to the total ocean area (361.9e6 km²) from ETOPO1 (Amante and Eakins,
741 2009; Eakins and Sharman, 2010). In products where the covered area varies with time (MPI-
742 SOMFFN, CMEMS) we use the maximum area coverage. The data-products cover 88% (MPI-
743 SOMFFN, CMEMS) to 101% (Jena-MLS) of the observed total ocean area, so two products are
744 effectively corrected upwards by a factor of 1.13 (Table A3, Hauck et al., 2020).

745 We further use results from two diagnostic ocean models, Khatiwala et al. (2013) and DeVries
746 (2014), to estimate the anthropogenic carbon accumulated in the ocean prior to 1959. The two
747 approaches assume constant ocean circulation and biological fluxes, with S_{OCEAN} estimated as a
748 response in the change in atmospheric CO₂ concentration calibrated to observations. The
749 uncertainty in cumulative uptake of ±20 GtC (converted to ±1σ) is taken directly from the IPCC's
750 review of the literature (Rhein et al., 2013), or about ±30% for the annual values (Khatiwala et
751 al., 2009).

752 **2.4.2 Global Ocean Biogeochemistry Models (GOBMs)**

753 The ocean CO₂ sink for 1959-2019 is estimated using nine GOBMs (Table A2). The GOBMs
754 represent the physical, chemical and biological processes that influence the surface ocean
755 concentration of CO₂ and thus the air-sea CO₂ flux. The GOBMs are forced by meteorological
756 reanalysis and atmospheric CO₂ concentration data available for the entire time period. They

757 mostly differ in the source of the atmospheric forcing data (meteorological reanalysis), spin up
758 strategies, and in their horizontal and vertical resolutions (Table A2). All GOBMs except one
759 (CESM-ETHZ) do not include the effects of anthropogenic changes in nutrient supply (Duce et
760 al., 2008). They also do not include the perturbation associated with changes in riverine organic
761 carbon (see Section 2.7.3).

762 Two sets of simulations were performed with each of the GOBMs. Simulation A applied
763 historical changes in climate and atmospheric CO₂ concentration. Simulation B is a control
764 simulation with constant atmospheric forcing (normal year or repeated year forcing) and
765 constant preindustrial atmospheric CO₂ concentration. In order to derive S_{OCEAN} from the model
766 simulations, we subtracted the annual time-series of the control simulation B from the annual
767 time-series of simulation A. Assuming that drift and bias are the same in simulations A and B,
768 we thereby correct for any model drift. Further, this difference also removes the natural steady
769 state flux (assumed to be 0 GtC yr⁻¹ globally) which is often a major source of biases. Simulation
770 B of IPSL had to be treated differently as it was forced with constant atmospheric CO₂, but
771 observed historical changes in climate. For IPSL, we fitted a linear trend to the simulation B and
772 subtracted this linear trend from simulation A. This approach assures that the interannual
773 variability is not removed from IPSL simulation A.

774 The absolute correction for bias and drift per model in the 1990s varied between <0.01 GtC yr⁻¹
775 and 0.35 GtC yr⁻¹, with six models having positive and three models having negative biases. This
776 correction reduces the model mean ocean carbon sink by 0.07 GtC yr⁻¹ in the 1990s. The CO₂
777 flux from each model is scaled by the ratio of the total ocean area covered by the respective
778 GOBM to the total ocean area (361.9e6 km²) from ETOPO1 (Amante and Eakins, 2009; Eakins
779 and Sharman, 2010). The ocean models cover 99% to 101% of the total ocean area, so the
780 effect of this correction is small.

781 **2.4.3 GOBM evaluation and uncertainty assessment for S_{OCEAN}**

782 The mean ocean CO₂ sink for all GOBMs and the ensemble mean falls within 90% confidence of
783 the observed range, or 1.5 to 2.9 GtC yr⁻¹ for the 1990s (Ciais et al., 2013) and within the
784 derived constraints for the 2000s and 2002-2011 (see section 2.4.1) before and after applying
785 corrections. The GOBMs and flux products have been further evaluated using the fugacity of
786 sea surface CO₂ from the SOCAT v2020 database (Bakker et al., 2016, 2020), hereafter referred
787 to as pCO₂. We focused this evaluation on the root mean squared error (RMSE) between

788 observed and modelled pCO₂ and on a measure of the amplitude of the interannual variability
789 of the flux (modified after Rödenbeck et al., 2015). The RMSE is calculated from annually and
790 regionally averaged time-series calculated from GOBM and data-product pCO₂ subsampled to
791 open ocean (water depth > 400 m) SOCAT sampling points to measure the misfit between
792 large-scale signals (Hauck et al., 2020) as opposed to the RMSE calculated from binned monthly
793 data as in the previous year. The amplitude of the S_{OCEAN} interannual variability (A-IAV) is
794 calculated as the temporal standard deviation of the detrended CO₂ flux time-series
795 (Rödenbeck et al., 2015, Hauck et al., 2020). These metrics are chosen because RMSE is the
796 most direct measure of data-model mismatch and the A-IAV is a direct measure of the
797 variability of S_{OCEAN} on interannual timescales. We apply these metrics globally and by latitude
798 bands (Fig. B1). Results are shown in Fig. B1 and discussed in Section 3.1.3.

799 The 1- σ uncertainty around the mean ocean sink of anthropogenic CO₂ was quantified by
800 Denman et al. (2007) for the 1990s to be ± 0.5 GtC yr⁻¹. Here we scale the uncertainty of ± 0.5
801 GtC yr⁻¹ to the mean estimate of 2.2 GtC yr⁻¹ in the 1990s to obtain a relative uncertainty of \pm
802 18%, which is then applied to the full time-series. To quantify the uncertainty around annual
803 values, we examine the standard deviation of the GOBM ensemble, which varies between 0.2
804 and 0.4 GtC yr⁻¹ and averages to 0.30 GtC yr⁻¹ during 1959-2019. We estimate that the
805 uncertainty in the annual ocean CO₂ sink increases from ± 0.3 GtC yr⁻¹ in the 1960s to ± 0.6 GtC
806 yr⁻¹ in the decade 2010-19 from the combined uncertainty of the mean flux based on
807 observations of $\pm 18\%$ (Denman et al., 2007) and the standard deviation across GOBMs of up to
808 ± 0.4 GtC yr⁻¹, reflecting both the uncertainty in the mean sink from observations during the
809 1990s (Denman et al., 2007; Section 2.4.1) and the uncertainty in annual estimates from the
810 standard deviation across the GOBM ensemble.

811 We examine the consistency between the variability of the model-based and the pCO₂-based
812 flux products to assess confidence in S_{OCEAN}. The interannual variability of the ocean fluxes
813 (quantified as A-IAV, the standard deviation after detrending, Figure B1) of the five pCO₂-based
814 flux products for 1992-2019, ranges from 0.16 to 0.25 GtC yr⁻¹ with the lower estimates by the
815 two ensemble methods (CSIR, CMEMS). The inter-annual variability in the GOBMs ranges
816 between 0.11 and 0.17 GtC yr⁻¹, hence there is overlap with the lower A-IAV estimates of two
817 data-products.

818 Individual estimates (both GOBM and flux products) generally produce a higher ocean CO₂ sink
819 during strong El Niño events. There is emerging agreement between GOBMs and data-products

820 on the patterns of decadal variability of S_{OCEAN} with a global stagnation in the 1990s and an
821 extra-tropical strengthening in the 2000s (McKinley et al., 2020, Hauck et al., 2020).
822 The annual $p\text{CO}_2$ -based flux products correlate with the ocean CO_2 sink estimated here with a
823 correlation coefficient r ranging from 0.75 to 0.97 (1985-2019). The central estimates of the
824 annual flux from the GOBMs and the $p\text{CO}_2$ -based flux products have a correlation r of 0.94
825 (1985-2019). The agreement between the models and the flux products reflects some
826 consistency in their representation of underlying variability since there is little overlap in their
827 methodology or use of observations. We assess a medium confidence level to the annual ocean
828 CO_2 sink and its uncertainty because it is based on multiple lines of evidence, it is consistent
829 with ocean interior carbon estimates (Gruber et al., 2019, see section 3.1.2) and the results are
830 consistent in that the interannual variability in the GOBMs and data-based estimates are all
831 generally small compared to the variability in the growth rate of atmospheric CO_2
832 concentration.

833 **2.5 Terrestrial CO_2 sink**

834 **2.5.1 DGVM simulations**

835 The terrestrial land sink (S_{LAND}) is thought to be due to the combined effects of fertilisation by
836 rising atmospheric CO_2 and N inputs on plant growth, as well as the effects of climate change
837 such as the lengthening of the growing season in northern temperate and boreal areas. S_{LAND}
838 does not include land sinks directly resulting from land-use and land-use change (e.g. regrowth
839 of vegetation) as these are part of the land-use flux (E_{LUC}), although system boundaries make it
840 difficult to attribute exactly CO_2 fluxes on land between S_{LAND} and E_{LUC} (Erb et al., 2013).

841 S_{LAND} is estimated from the multi-model mean of 17 DGVMs (Table 4). As described in section
842 2.2.2, DGVM simulations include all climate variability and CO_2 effects over land, with 12
843 DGVMs also including the effect of N inputs. The DGVMs estimate of S_{LAND} does not include the
844 export of carbon to aquatic systems or its historical perturbation, which is discussed in section
845 2.7.3.

846 **2.5.2 DGVM evaluation and uncertainty assessment for S_{LAND}**

847 We apply three criteria for minimum DGVM realism by including only those DGVMs with (1)
848 steady state after spin up, (2) global net land flux ($S_{\text{LAND}} - E_{\text{LUC}}$) that is an atmosphere-to-land
849 carbon flux over the 1990s ranging between -0.3 and 2.3 GtC yr^{-1} , within 90% confidence of

850 constraints by global atmospheric and oceanic observations (Keeling and Manning, 2014;
851 Wanninkhof et al., 2013), and (3) global E_{LUC} that is a carbon source to the atmosphere over the
852 1990s, as mentioned in section 2.2.2. All 17 DGVMs meet these three criteria.

853 In addition, the DGVM results are also evaluated using the International Land Model
854 Benchmarking system (ILAMB; Collier et al., 2018). This evaluation is provided here to
855 document, encourage and support model improvements through time. ILAMB variables cover
856 key processes that are relevant for the quantification of S_{LAND} and resulting aggregated
857 outcomes. The selected variables are vegetation biomass, gross primary productivity, leaf area
858 index, net ecosystem exchange, ecosystem respiration, evapotranspiration, soil carbon, and
859 runoff (see Fig. B2 for the results and for the list of observed databases). Results are shown in
860 Fig. B2 and discussed in Section 3.1.3.

861 For the uncertainty for S_{LAND} , we use the standard deviation of the annual CO_2 sink across the
862 DGVMs, averaging to about $\pm 0.6 \text{ GtC yr}^{-1}$ for the period 1959 to 2019. We attach a medium
863 confidence level to the annual land CO_2 sink and its uncertainty because the estimates from the
864 residual budget and averaged DGVMs match well within their respective uncertainties (Table
865 5).

866 **2.6 The atmospheric perspective**

867 The world-wide network of atmospheric measurements and satellite xCO_2 observations can be
868 used with atmospheric inversion methods to constrain the location of the combined total
869 surface CO_2 fluxes from all sources, including fossil and land-use change emissions and land and
870 ocean CO_2 fluxes. The inversions assume E_{FOS} to be well known, and they solve for the spatial
871 and temporal distribution of land and ocean fluxes from the residual gradients of CO_2 between
872 stations that are not explained by fossil fuel emissions.

873 Six atmospheric inversions (Table A4) used atmospheric CO_2 data to the end of 2019 (including
874 preliminary values in some cases) to infer the spatio-temporal distribution of the CO_2 flux
875 exchanged between the atmosphere and the land or oceans. We focus here on the total land
876 and ocean CO_2 fluxes and their partitioning among the Northern extratropics (30°N - 90°N), the
877 tropics (30°S - 30°N) and the Southern extratropics (30°S - 90°S). We also break down those
878 estimates for the land and ocean regions separately. We use these estimates to comment on
879 the consistency across various data streams and process-based estimates.

2801 Atmospheric inversions

881 The six inversion systems used in this release are described in Table A4. The inversions are
882 based on Bayesian inversion principles with prior information on fluxes and their uncertainties.
883 The inversion systems are based on near-identical observations of surface measurements of
884 CO₂ time series (or subsets thereof) from various flask and in situ networks. Two inversion
885 systems (UoE and CAMS) were also applied using only satellite xCO₂ measurements from
886 GOSAT or OCO-2, but their results at the larger scales discussed in this work did not deviate
887 substantially from their in-situ counterparts, and are therefore not separately included (Palmer
888 et al., 2009, 2019). Each inversion system uses different methodologies and input data but is
889 rooted in Bayesian inversion principles (Table A4). These differences mainly concern the
890 selection of atmospheric CO₂ data and prior fluxes, as well as the spatial resolution, assumed
891 correlation structures, and mathematical approach of the models. The details of each model's
892 approach are documented extensively in the references provided in Table A4. Each system uses
893 a different transport model, which was demonstrated to be a driving factor behind differences
894 in atmospheric inversion based flux estimates, and specifically their distribution across
895 latitudinal bands (e.g., Gaubert et al., 2019).

896 The inversion systems prescribe global fossil fuel emissions. For the first time in this year's
897 budget, most (five of the six) inversion systems prescribed the same estimate for E_{FOS};
898 specifically, the GCP's Gridded Fossil Emissions Dataset version 2020.1 (GCP-GridFEDv2020.1),
899 which is an update to 2019 of the first version of GCP-GridFED presented by Jones et al. (*in*
900 *revision*). GCP-GridFEDv2020.1 scales gridded estimates of CO₂ emissions from EDGARv4.3.2
901 (Janssens-Maenhout et al., 2019) within national territories to match national emissions
902 estimates provided by the GCP for the years 1959-2019, which were compiled following the
903 methodology described in section 2.1 with all datasets available on 31st July 2020 (R. Andrew,
904 *pers. comm.*).

905 Previously, the use of different estimate for E_{FOS} resulted in different estimates of total CO₂
906 uptake in atmospheric inversions (Peylin et al., 2013; Gaubert et al., 2019), and it was necessary
907 to adjust the land sink of each inversion estimate to enforce a common E_{FOS}. Adjustments of up
908 to 0.5 GtC were applied in certain years in the Northern extratropics. The use of a common E_{FOS}
909 avoids the need to correct the estimated land sink for most models, with the exception of the
910 UoE inversion (see Table A4). Further, the use of GCP-GridFEDv2020.1 for E_{FOS} ensures a close

911 alignment with the estimate of E_{FOS} used in this budget assessment, enhancing the
912 comparability of the inversion-based estimate with the flux estimates deriving from DGVMs,
913 GOBMs and pCO_2 -based methods.

914 The land and ocean CO_2 fluxes from atmospheric inversions contain anthropogenic
915 perturbation and natural pre-industrial CO_2 fluxes. On annual time scales, natural pre-industrial
916 fluxes are primarily land CO_2 sinks and ocean CO_2 sources corresponding to carbon taken up on
917 land, transported by rivers from land to ocean, and outgassed by the ocean. These pre-
918 industrial land CO_2 sinks are thus compensated over the globe by ocean CO_2 sources
919 corresponding to the outgassing of riverine carbon inputs to the ocean. We apply the
920 distribution of land-to-ocean C fluxes from rivers in three latitude bands using estimates from
921 Resplandy et al. (2018), which are constrained by ocean heat transport to a total land-to-ocean
922 carbon transfer of 0.61 GtC yr^{-1} . The latitude distribution of river-induced ocean CO_2 sources
923 (North: 0.16 GtC yr^{-1} , Tropics: 0.15 GtC yr^{-1} , South: 0.30 GtC yr^{-1}) from carbon originating from
924 land (North: 0.29 GtC yr^{-1} , Tropics: 0.32 GtC yr^{-1} , South: $<0.01 \text{ GtC yr}^{-1}$) are derived from a
925 simulation of the IPSL GOBM using as an input the river flux constrained by heat transport of
926 Resplandy et al. (2018). To facilitate the comparison, we adjusted the inverse estimates of the
927 land and ocean fluxes per latitude band with these numbers to produce historical perturbation
928 CO_2 fluxes from inversions.

929 The atmospheric inversions are also evaluated using vertical profiles of atmospheric CO_2
930 concentrations (Fig. B3). More than 30 aircraft programs over the globe, either regular
931 programs or repeated surveys over at least 9 months, have been used in order to draw a robust
932 picture of the model performance (with space-time data coverage irregular and denser in the 0-
933 45°N latitude band; Table A6). The six models are compared to the independent aircraft CO_2
934 measurements between 2 and 7 km above sea level between 2001 and 2018. Results are shown
935 in Fig. B3 and discussed in Section 3.1.3.

936 **2.7 Processes not included in the global carbon budget**

937 The contribution of anthropogenic CO and CH_4 to the global carbon budget is not fully
938 accounted for in Eq. (1) and is described in Section 2.7.1. The contributions of other carbonates
939 to CO_2 emissions is described in Section 2.7.2. The contribution of anthropogenic changes in
940 river fluxes is conceptually included in Eq. (1) in S_{OCEAN} and in S_{LAND} , but it is not represented in

941 the process models used to quantify these fluxes. This effect is discussed in Section 2.7.3.
942 Similarly, the loss of additional sink capacity from reduced forest cover is missing in the
943 combination of approaches used here to estimate both land fluxes (E_{LUC} and S_{LAND}) and its
944 potential effect is discussed and quantified in Section 2.7.4.

945 **2.7.1 Contribution of anthropogenic CO and CH₄ to the global carbon budget**

946 Equation (1) includes only partly the net input of CO₂ to the atmosphere from the chemical
947 oxidation of reactive carbon-containing gases from sources other than the combustion of fossil
948 fuels, such as: (1) cement process emissions, since these do not come from combustion of fossil
949 fuels, (2) the oxidation of fossil fuels, (3) the assumption of immediate oxidation of vented
950 methane in oil production. It omits however any other anthropogenic carbon-containing gases
951 that are eventually oxidised in the atmosphere, such as anthropogenic emissions of CO and CH₄.
952 An attempt is made in this section to estimate their magnitude, and identify the sources of
953 uncertainty. Anthropogenic CO emissions are from incomplete fossil fuel and biofuel burning
954 and deforestation fires. The main anthropogenic emissions of fossil CH₄ that matter for the
955 global (anthropogenic) carbon budget are the fugitive emissions of coal, oil and gas sectors (see
956 below). These emissions of CO and CH₄ contribute a net addition of fossil carbon to the
957 atmosphere.

958 In our estimate of E_{FOS} we assumed (Section 2.1.1) that all the fuel burned is emitted as CO₂,
959 thus CO anthropogenic emissions associated with incomplete fossil fuel combustion and its
960 atmospheric oxidation into CO₂ within a few months are already counted implicitly in E_{FOS} and
961 should not be counted twice (same for E_{LUC} and anthropogenic CO emissions by deforestation
962 fires). Anthropogenic emissions of fossil CH₄ are however not included in E_{FOS} , because these
963 fugitive emissions are not included in the fuel inventories. Yet they contribute to the annual
964 CO₂ growth rate after CH₄ gets oxidized into CO₂. Emissions of fossil CH₄ represent 30% of total
965 anthropogenic CH₄ emissions (Saunio et al. 2020 ; their top-down estimate is used because it is
966 consistent with the observed CH₄ growth rate), that is 0.083 GtC yr⁻¹ for the decade 2008-2017.
967 Assuming steady state, an amount equal to this fossil CH₄ emission is all converted to CO₂ by
968 OH oxidation, and thus explain 0.083 GtC yr⁻¹ of the global CO₂ growth rate with an uncertainty
969 range of 0.061 to 0.098 GtC yr⁻¹ taken from the min-max of top-down estimates in Saunio et
970 al. 2020. If this min-max range is assumed to be 2 σ because Saunio et al. did not account for

971 the internal uncertainty of their min and max top-down estimates, it translates into a 1- σ
972 uncertainty of 0.019 GtC yr⁻¹.

973 Other anthropogenic changes in the sources of CO and CH₄ from wildfires, vegetation biomass,
974 wetlands, ruminants or permafrost changes are similarly assumed to have a small effect on the
975 CO₂ growth rate. The CH₄ and CO emissions and sinks are published and analysed separately in
976 the Global Methane Budget and Global Carbon Monoxide Budget publications, which follow a
977 similar approach to that presented here (Saunois et al., 2020; Zheng et al., 2019).

978 **2.7.2 Contribution of other carbonates to CO₂ emissions**

979 Even though this year we account for cement carbonation, the contribution of emissions of
980 fossil carbonates other than cement production is not systematically included in estimates of
981 E_{FOS}, except at the national level where they are accounted in the UNFCCC national inventories.
982 The missing processes include CO₂ emissions associated with the calcination of lime and
983 limestone outside cement production. Carbonates are also used in various industries, including
984 in iron and steel manufacture and in agriculture. They are found naturally in some coals.

985 **2.7.3 Anthropogenic carbon fluxes in the land-to-ocean aquatic continuum**

986 The approach used to determine the global carbon budget refers to the mean, variations, and
987 trends in the perturbation of CO₂ in the atmosphere, referenced to the pre-industrial era.
988 Carbon is continuously displaced from the land to the ocean through the land-ocean aquatic
989 continuum (LOAC) comprising freshwaters, estuaries and coastal areas (Bauer et al., 2013;
990 Regnier et al., 2013). A significant fraction of this lateral carbon flux is entirely 'natural' and is
991 thus a steady state component of the pre-industrial carbon cycle. We account for this pre-
992 industrial flux where appropriate in our study. However, changes in environmental conditions
993 and land-use change have caused an increase in the lateral transport of carbon into the LOAC –
994 a perturbation that is relevant for the global carbon budget presented here.

995 The results of the analysis of Regnier et al. (2013) can be summarized in two points of relevance
996 for the anthropogenic CO₂ budget. First, the anthropogenic perturbation of the LOAC has
997 increased the organic carbon export from terrestrial ecosystems to the hydrosphere by as much
998 as 1.0 ± 0.5 GtC yr⁻¹ since pre-industrial, mainly owing to enhanced carbon export from soils.
999 Second, this exported anthropogenic carbon is partly respired through the LOAC, partly
1000 sequestered in sediments along the LOAC and to a lesser extent, transferred to the open ocean

1001 where it may accumulate or be outgassed. The increase in storage of land-derived organic
1002 carbon in the LOAC carbon reservoirs (burial) and in the open ocean combined is estimated by
1003 Regnier et al. (2013) at $0.65 \pm 0.35 \text{ GtC yr}^{-1}$. The inclusion of LOAC related anthropogenic CO_2
1004 fluxes should affect estimates of S_{LAND} and S_{OCEAN} in Eq. (1), but does not affect the other terms.
1005 Representation of the anthropogenic perturbation of LOAC CO_2 fluxes is however not included
1006 in the GOBMs and DGVMs used in our global carbon budget analysis presented here.

1007 **2.7.4 Loss of additional sink capacity**

1008 Historical land-cover change was dominated by transitions from vegetation types that can
1009 provide a large carbon sink per area unit (typically, forests) to others less efficient in removing
1010 CO_2 from the atmosphere (typically, croplands). The resultant decrease in land sink, called the
1011 ‘loss of additional sink capacity’, can be calculated as the difference between the actual land
1012 sink under changing land-cover and the counterfactual land sink under pre-industrial land-
1013 cover. This term is not accounted for in our global carbon budget estimate. Here, we provide a
1014 quantitative estimate of this term to be used in the discussion. Seven of the DGVMs used in
1015 Friedlingstein et al (2019) performed additional simulations with and without land-use change
1016 under cycled pre-industrial environmental conditions. The resulting loss of additional sink
1017 capacity amounts to $0.9 \pm 0.3 \text{ GtC yr}^{-1}$ on average over 2009-2018 and $42 \pm 16 \text{ GtC}$ accumulated
1018 between 1850 and 2018. OSCAR, emulating the behaviour of 11 DGVMs finds values of the loss
1019 of additional sink capacity of $0.7 \pm 0.6 \text{ GtC yr}^{-1}$ and $31 \pm 23 \text{ GtC}$ for the same time period (Gasser
1020 et al., 2020).

1021 **3 Results**

1022 **3.1 Global carbon budget mean and variability for 1959-2019**

1023 The global carbon budget averaged over the historical period (1850-2019) is shown in Fig. 3. For
1024 the more recent 1959-2019 period where direct atmospheric CO_2 measurements are available ,
1025 81% of the total emissions ($E_{\text{FOS}} + E_{\text{LUC}}$) were caused by fossil CO_2 emissions, and 19% by land-
1026 use change. The total emissions were partitioned among the atmosphere (45%), ocean (24%)
1027 and land (32%), with a near-zero unattributed budget imbalance (0%). All components except
1028 land-use change emissions have significantly grown since 1959, with important interannual
1029 variability in the growth rate in atmospheric CO_2 concentration and in the land CO_2 sink (Fig. 4),

1030 and some decadal variability in all terms (Table 6). Differences with previous budget releases
1031 are documented in Fig. B4.

1032 **3.1.1 CO₂ emissions**

1033 Global fossil CO₂ emissions have increased every decade from an average of 3.0 ± 0.2 GtC yr⁻¹
1034 for the decade of the 1960s to an average of 9.4 ± 0.5 GtC yr⁻¹ during 2010-2019 (Table 6, Fig. 2
1035 and Fig. 5). The growth rate in these emissions decreased between the 1960s and the 1990s,
1036 from 4.3% yr⁻¹ in the 1960s (1960-1969), 3.1% yr⁻¹ in the 1970s (1970-1979), 1.6% yr⁻¹ in the
1037 1980s (1980-1989), to 0.9% yr⁻¹ in the 1990s (1990-1999). After this period, the growth rate
1038 began increasing again in the 2000s at an average growth rate of 3.0% yr⁻¹, decreasing to 1.2%
1039 yr⁻¹ for the last decade (2010-2019).

1040 In contrast, CO₂ emissions from land-use, land-use change and forestry have remained
1041 relatively constant, at around 1.4 ± 0.7 GtC yr⁻¹ over the past half-century (Table 6) but with
1042 large spread across estimates (Table 5, Fig. 6). These emissions are also relatively constant in
1043 the DGVM ensemble of models, except during the last decade when they increase to 2.1 ± 0.5
1044 GtC yr⁻¹. However, there is no agreement on this recent increase between the bookkeeping
1045 estimates, with H&N2017 suggesting a downward trend as compared to a weak and strong
1046 upward trend in OSCAR and the BLUE estimates respectively (Fig. 6).

1047 For the first time we provide estimates of gross land use changes fluxes: gross sources from
1048 decaying material left dead on site and from products after clearing of natural vegetation for
1049 agricultural purposes, wood harvesting, and, for BLUE, degradation from primary to secondary
1050 land through usage of natural vegetation as rangeland, and emissions from peat drainage and
1051 peat burning; and gross sinks from regrowth after agricultural abandonment and wood
1052 harvesting. Gross sources are on average 2-3 times larger than net emissions, increasing from an
1053 average of 3.5 ± 1.2 GtC yr⁻¹ for the decade of the 1960s to an average of 4.4 ± 1.6 GtC yr⁻¹
1054 during 2010-2019 (Fig. 6, Table 5), showing the relevance of land management such as
1055 harvesting or rotational agriculture. They differ more across the three bookkeeping estimates
1056 than net fluxes, which is expected due to different process representation; in particular
1057 exclusion of shifting cultivation (H&N2017) reduces both sources and sinks.

1058 The uptake of CO₂ by cement via carbonation has increased with increasing stocks of cement
1059 products, from an average of 20 MtC yr⁻¹ in the 1960s to an average of 190 MtC yr⁻¹ during

1060 2010-2019 (Fig. 5). The growth rate declined from 6.7% yr⁻¹ in the 1960s to 3.3% yr⁻¹ in the
1061 1980s, rising again to 6.2% yr⁻¹ in the 2000s, before declining again to 3.5% yr⁻¹ in the 2010s.

1062 **3.1.2 Partitioning among the atmosphere, ocean and land**

1063 The growth rate in atmospheric CO₂ level increased from 1.8 ± 0.07 GtC yr⁻¹ in the 1960s to 5.1
1064 ± 0.02 GtC yr⁻¹ during 2010-2019 with important decadal variations (Table 6 and Fig. 3). Both
1065 ocean and land CO₂ sinks have increased roughly in line with the atmospheric increase, but with
1066 significant decadal variability on land (Table 6 and Fig. 6), and possibly in the ocean (Fig. 7).

1067 The ocean CO₂ sink increased from 1.0 ± 0.3 GtC yr⁻¹ in the 1960s to 2.5 ± 0.6 GtC yr⁻¹ during
1068 2010-2019, with interannual variations of the order of a few tenths of GtC yr⁻¹ generally
1069 showing an increased ocean sink during large El Niño events (i.e. 1997-1998) (Fig. 7; Rödenbeck
1070 et al., 2014, Hauck et al., 2020). The GOBMs show the same patterns of decadal variability as
1071 the mean of the pCO₂-based flux products, but of weaker magnitude (Section 2.4.3 and Fig. 7;
1072 DeVries et al., 2019, Hauck et al., 2020). The pCO₂-based flux products and the ocean inverse
1073 model highlight different regions as the main origin of this decadal variability, with the pCO₂-
1074 based flux products placing more of the weakening trend in the Southern Ocean and the ocean
1075 inverse model suggesting that more of the weakening trend occurred in the North Atlantic and
1076 North Pacific (DeVries et al., 2019). Both approaches show also decadal trends in the low-
1077 latitude oceans (DeVries et al., 2019).

1078 Although all individual GOBMs and data-products fall within the observational constraint, the
1079 ensemble means of GOBMs and data-products adjusted for the riverine flux diverge over time
1080 with a mean offset of 0.4 GtC yr⁻¹ in the 1990s to 0.8 GtC yr⁻¹ in the decade 2010-2019 and > 1
1081 GtC yr⁻¹ since 2017. The GOBMs best estimate of S_{OCEAN} over the period 1994-2007 is 2.1 ± 0.5
1082 GtC yr⁻¹ and is in agreement with the ocean interior estimate of 2.2 ± 0.4 GtC yr⁻¹ when taking
1083 into account the interior ocean carbon changes of 2.6 ± 0.3 GtC yr⁻¹ due to the increase of
1084 atmospheric CO₂ and -0.4 ± 0.24 GtC yr⁻¹ due to anthropogenic climate change and variability
1085 (Gruber et al., 2019) to match the definition of S_{OCEAN} used here (Hauck et al., 2020). The
1086 discrepancy between GOBMs and data-products is higher than in previous releases of the
1087 Global Carbon Budget (e.g. Friedlingstein et al., 2019, Hauck et al., 2020), due to changes in the
1088 data-product ensemble. The Jena-MLS product was revised upwards and CSIR and Watson et al
1089 are new in the ensemble. The Watson et al. (2020) data-product is higher than all other data-
1090 products prior to 1992 and since 2005. The discrepancy between GOBMs and data-products

1091 stems from the southern and northern extratropics prior to 2005, and mostly from the
1092 Southern Ocean since the mid-2000s. Possible explanations for the discrepancy in the Southern
1093 Ocean could be missing winter observations or uncertainties in the regional river flux
1094 adjustment (see section 3.2.3.1, Hauck et al., 2020).

1095 The terrestrial CO₂ sink increased from 1.3 ± 0.4 GtC yr⁻¹ in the 1960s to 3.4 ± 0.9 GtC yr⁻¹ during
1096 2010-2019, with important interannual variations of up to 2 GtC yr⁻¹ generally showing a
1097 decreased land sink during El Niño events (Fig. 6), responsible for the corresponding enhanced
1098 growth rate in atmospheric CO₂ concentration. The larger land CO₂ sink during 2010-2019
1099 compared to the 1960s is reproduced by all the DGVMs in response to the combined
1100 atmospheric CO₂ increase and the changes in climate, and consistent with constraints from the
1101 other budget terms (Table 5).

1102 The total atmosphere-to-land fluxes ($S_{\text{LAND}} - E_{\text{LUC}}$), calculated here as the difference between
1103 S_{LAND} from the DGVMs and E_{LUC} from the bookkeeping models, increased from a 0.2 ± 0.9 GtC yr⁻¹
1104 ¹ source in the 1960s to a 1.9 ± 1.1 GtC yr⁻¹ sink during 2010-2019 (Table 5). Estimates of total
1105 atmosphere-to-land fluxes ($S_{\text{LAND}} - E_{\text{LUC}}$) from the DGVMs alone are consistent with our
1106 estimate and also with the global carbon budget constraint ($E_{\text{FOS}} - G_{\text{ATM}} - S_{\text{OCEAN}}$, Table 5). Over the
1107 last decade, the land use emission estimate from the DGVMs is significantly larger than the
1108 bookkeeping estimate, mainly explaining why the DGVMs total atmosphere-to-land flux
1109 estimate is lower than the other estimates.

1110 **3.1.3 Model evaluation**

1111 The evaluation of the ocean estimates (Fig. B1) shows an RMSE from annually detrended data
1112 of 0.5 to 1.6 μatm for the five pCO₂-based flux products over the globe, relative to the pCO₂
1113 observations from the SOCAT v2020 database for the period 1985-2019. The GOBM RMSEs are
1114 larger and range from 3.5 to 6.9 μatm. The RMSEs are generally larger at high latitudes
1115 compared to the tropics, for both the flux products and the GOBMs. The five flux products have
1116 RMSEs of 0.4 to 1.9 μatm in the tropics, 0.6 to 1.9 μatm in the north, and 1.5 to 2.8 μatm in the
1117 south. Note that the flux products are based on the SOCAT v2020 database, hence these latter
1118 are no independent data set for the evaluation of the flux products. The GOBM RMSEs are
1119 more spread across regions, ranging from 2.7 to 4.0 μatm in the tropics, 3.1 to 7.3 μatm in the
1120 North, and 6.6 to 11.4 μatm in the South. The higher RMSEs occur in regions with stronger

1121 climate variability, such as the northern and southern high latitudes (poleward of the
1122 subtropical gyres).
1123 The evaluation of the DGVMs (Fig. B2) shows generally high skill scores across models for
1124 runoff, and to a lesser extent for vegetation biomass, GPP, and ecosystem respiration (Fig. B2,
1125 left panel). Skill score was lowest for leaf area index and net ecosystem exchange, with a widest
1126 disparity among models for soil carbon. Further analysis of the results will be provided
1127 separately, focusing on the strengths and weaknesses in the DGVM ensemble and its validity for
1128 use in the global carbon budget.

1129 The evaluation of the atmospheric inversions (Fig. B3) shows long-term mean biases in the free
1130 troposphere lower than 0.4 ppm in absolute values for each product. These biases show some
1131 dependency on latitude and are different for each inverse model, which may reveal biases in
1132 the surface fluxes (e.g., Houweling et al., 2015, Gaubert et al., 2019). Despite tracking surface
1133 and in-situ CO₂ observations, the systems reproduce NOAA's global annual CO₂ growth rate
1134 (Section 2.3.1) with mixed skill: where decadal biases are typically small for all systems (<0.08
1135 ppm/yr), interannual differences are larger (1- σ : 0.10-0.25 ppm/yr, N=19 years) but can be as
1136 large as 0.6 ppm/yr for the model/year with worst performance on this metric.

1137 **3.1.4 Budget imbalance**

1138 The carbon budget imbalance (B_{IM} ; Eq. 1) quantifies the mismatch between the estimated total
1139 emissions and the estimated changes in the atmosphere, land and ocean reservoirs. The mean
1140 budget imbalance from 1959 to 2019 is small (average of -0.03 GtC yr⁻¹) and shows no trend
1141 over the full time series. The process models (GOBMs and DGVMs) have been selected to
1142 match observational constraints in the 1990s and derived constraints for the 2000s and 2002-
1143 2011, but no further constraints have been applied to their representation of trend and
1144 variability. Therefore, the near-zero mean and trend in the budget imbalance is an indirect
1145 evidence of a coherent community understanding of the emissions and their partitioning on
1146 those time scales (Fig. 4). However, the budget imbalance shows substantial variability of the
1147 order of ± 1 GtC yr⁻¹, particularly over semi-decadal time scales, although most of the variability
1148 is within the uncertainty of the estimates. The positive carbon imbalance during the 1960s,
1149 early 1990s, and in the last decade, suggests that either the emissions were overestimated or
1150 the sinks were underestimated during these periods. The reverse is true for the 1970s and
1151 around 1995-2000 (Fig. 4).

1152 We cannot attribute the cause of the variability in the budget imbalance with our analysis, we
1153 only note that the budget imbalance is unlikely to be explained by errors or biases in the
1154 emissions alone because of its large semi-decadal variability component, a variability that is
1155 untypical of emissions and has not changed in the past 50 years in spite of a near tripling in
1156 emissions (Fig. 4). Errors in S_{LAND} and S_{OCEAN} are more likely to be the main cause for the budget
1157 imbalance. For example, underestimation of the S_{LAND} by DGVMs has been reported following
1158 the eruption of Mount Pinatubo in 1991 possibly due to missing responses to changes in diffuse
1159 radiation (Mercado et al., 2009) or other yet unknown factors, and DGVMs are suspected to
1160 overestimate the land sink in response to the wet decade of the 1970s (Sitch et al., 2008).
1161 Quasi-decadal variability in the ocean sink has also been reported recently (DeVries et al., 2019,
1162 2017; Landschützer et al., 2015), with all methods agreeing on a smaller than expected ocean
1163 CO_2 sink in the 1990s and a larger than expected sink in the 2000s (Fig. 7; DeVries et al., 2019,
1164 McKinley et al., 2020). The decadal variability is possibly caused by changes in ocean circulation
1165 (DeVries et al., 2017) not captured in coarse resolution GOBMs used here (Dufour et al., 2013),
1166 but also by external forcing from decadal varying atmospheric CO_2 growth rates and cooling
1167 effects through the eruption of Mount Pinatubo in 1991 which is captured by GOBMs (McKinley
1168 et al., 2020).
1169 The decadal variability is thought to be largest in the high latitude ocean regions (poleward of
1170 the subtropical gyres) and the equatorial Pacific (Li and Ilyina, 2018; McKinley et al., 2016,
1171 McKinley et al., 2020). Some of these errors could be driven by errors in the climatic forcing
1172 data, particularly precipitation (for S_{LAND}) and wind (for S_{OCEAN}) rather than in the models.

1173 **3.2 Global carbon budget for the last decade (2010 – 2019)**

1174 The global carbon budget averaged over the last decade (2010-2019) is shown in Fig. 2 and Fig.
1175 9 (right panel). For this time period, 86% of the total emissions ($E_{\text{FOS}} + E_{\text{LUC}}$) were from fossil CO_2
1176 emissions (E_{FOS}), and 14% from land-use change (E_{LUC}). The total emissions were partitioned
1177 among the atmosphere (46%), ocean (23%) and land (31%), with an unattributed budget
1178 imbalance (-1%).

1179 **3.2.1 CO_2 emissions**

1180 Global fossil CO_2 emissions grew at a rate of $1.2\% \text{ yr}^{-1}$ for the last decade (2010-2019), with a
1181 decadal average of $9.4 \pm 0.5 \text{ GtC yr}^{-1}$ (Fig. 5, Table 6). China's emissions increased by $+1.2\% \text{ yr}^{-1}$
1182 on average (increasing by $+0.046 \text{ GtC yr}^{-1}$ during the 10-year period) dominating the global

1183 trend, followed by India's emissions increase by $+5.1\% \text{ yr}^{-1}$ (increasing by $+0.025 \text{ GtC yr}^{-1}$), while
1184 emissions decreased in EU27 by $-1.4\% \text{ yr}^{-1}$ (decreasing by $-0.014 \text{ GtC yr}^{-1}$), and in the USA by $-$
1185 $0.7\% \text{ yr}^{-1}$ (decreasing by $-0.01 \text{ GtC yr}^{-1}$). In the past decade, fossil CO_2 emissions decreased
1186 significantly (at the 95% level) in 19 growing economies: Belgium, Croatia, Czech Republic,
1187 Denmark, Finland, France, Italy, Latvia, Luxembourg, Republic of Macedonia, Malta, the
1188 Netherlands, Romania, Slovenia, Sweden, Switzerland, United Kingdom, USA and Uzbekistan.
1189 The drivers of recent decarbonisation are examined in Le Quéré et al. (2019).

1190 In contrast, there is no clear trend in CO_2 emissions from land-use change over the last decade
1191 (Fig. 6, Table 6), though the data are very uncertain, with partly diverging trends over the last
1192 decade (Sec. 3.1.1). Larger emissions are expected increasingly over time for DGVM-based
1193 estimates as they include the loss of additional sink capacity, while the bookkeeping estimates
1194 do not. The LUH2 data set also features large dynamics in land-use in particular in the tropics in
1195 recent years, causing higher emissions in DGVMs, BLUE and the OSCAR best-guess, which
1196 includes simulations based on LUH2, than in H&N.

1197 **3.2.2 Partitioning among the atmosphere, ocean and land**

1198 The growth rate in atmospheric CO_2 concentration increased during 2010-2019, with a decadal
1199 average of $5.1 \pm 0.02 \text{ GtC yr}^{-1}$, albeit with large interannual variability (Fig. 4). Averaged over
1200 that decade, the ocean and land sinks amount to $2.5 \pm 0.6 \text{ GtC yr}^{-1}$ and $3.4 \pm 0.9 \text{ GtC yr}^{-1}$
1201 respectively. During 2010-2017, the ocean CO_2 sink appears to have intensified in line with the
1202 expected increase from atmospheric CO_2 (McKinley et al., 2020). This effect is stronger in the
1203 pCO_2 -based flux products (Fig. 7, McKinley et al., 2020). The reduction of -0.16 GtC (range: -0.43
1204 to $+0.03 \text{ GtC}$) in the ocean CO_2 sink in 2017 is consistent with the return to normal conditions
1205 after the El Niño in 2015/16, which caused an enhanced sink in previous years.

1206 The budget imbalance (Table 6) and the residual sink from global budget (Table 5) include an
1207 error term due to the inconsistency that arises from using E_{LUC} from bookkeeping models, and
1208 S_{LAND} from DGVMs. This error term includes the fundamental differences between bookkeeping
1209 models and DGVMs, most notably the loss of additional sink capacity. Other differences
1210 include: an incomplete accounting of LUC practices and processes in DGVMs, while they are all
1211 accounted for in bookkeeping models by using observed carbon densities, and bookkeeping
1212 error of keeping present-day carbon densities fixed in the past. That the budget imbalance
1213 shows no clear trend towards larger values over time is an indication that the loss of additional

1214 sink capacity plays a minor role compared to other errors in S_{LAND} or S_{OCEAN} (discussed in Section
1215 3.1.4).

1216 **3.2.3 Inter-comparison of flux estimates (2010-2019)**

1217 **3.2.3.1 Regionality**

1218 Fig. 8 shows the partitioning of the total atmosphere-to-surface fluxes excluding fossil CO₂
1219 emissions ($S_{\text{OCEAN}} + S_{\text{LAND}} - E_{\text{LUC}}$) according to the multi-model average estimates from process
1220 models (GOBMs and DGVMs), atmospheric inversions and ocean pCO₂-based products. Fig. 8
1221 provides information on the regional distribution of those fluxes by latitude bands. The global
1222 mean total atmosphere-to-surface CO₂ fluxes from process models for 2010-2019 is 3.8 ± 0.7
1223 GtC yr⁻¹, below the global mean atmosphere-to-surface flux of 4.3 ± 0.5 GtC yr⁻¹ inferred by the
1224 carbon budget ($E_{\text{FOS}} - G_{\text{ATM}}$ in Equation 1; Table 6). The total atmosphere-to-surface CO₂ fluxes
1225 from the inversions (4.5 ± 0.1 GtC yr⁻¹) almost matches the value inferred by the carbon budget,
1226 which is expected due to the constraint on G_{ATM} incorporated within the inversion approach
1227 and the adjustment of the fossil emissions prior to a value consistent with the E_{FOS} budget term
1228 (Jones et al., *in revision*; See Section 2.6).

1229 In the southern extratropics (south of 30°S), the atmospheric inversions suggest a total
1230 atmosphere-to-surface sink ($S_{\text{OCEAN}} + S_{\text{LAND}} - E_{\text{LUC}}$) for 2010-2019 of 1.8 ± 0.2 GtC yr⁻¹, above the
1231 process models' estimate of 1.4 ± 0.3 GtC yr⁻¹ (Fig. 8). An approximately neutral total land flux
1232 ($S_{\text{LAND}} - E_{\text{LUC}}$) for the southern extratropics is estimated by both the DGVMs (0.0 ± 0.1 GtC yr⁻¹)
1233 and the inversion models (sink of 0.1 ± 0.2 GtC yr⁻¹). The GOBMs (1.4 ± 0.3 GtC yr⁻¹) produce a
1234 lower estimate for the ocean sink than the inversion models (1.6 ± 0.2 GtC yr⁻¹) or pCO₂-based
1235 flux products (1.8 ± 0.2 GtC yr⁻¹; discussed further below).

1236 In the tropics (30°S-30°N), both the atmospheric inversions and process models suggest that
1237 the total carbon balance in this region ($S_{\text{OCEAN}} + S_{\text{LAND}} - E_{\text{LUC}}$) is close to neutral over the past
1238 decade. The inversion models indicate a small tropical source to the atmosphere of 0.2 ± 0.6
1239 GtC yr⁻¹, whereas the process models indicate a small sink of 0.2 ± 0.7 GtC yr⁻¹. The GOBMs (0.1
1240 ± 0.2 GtC yr⁻¹ source), inversion models (0.1 ± 0.2 GtC yr⁻¹ source) and pCO₂-based flux products
1241 (0.0 ± 0.1 GtC yr⁻¹) all indicate an approximately neutral tropical ocean flux, meaning that the
1242 difference in sign of the total fluxes stems from the land component. Indeed, the DGVMs
1243 indicate a total land sink ($S_{\text{LAND}} - E_{\text{LUC}}$) of 0.2 ± 0.7 GtC yr⁻¹, whereas the inversion models indicate

1244 a small land source of $0.1 \pm 0.7 \text{ GtC yr}^{-1}$, though with high uncertainty in both cases. Overall, the
1245 GOBMs, pCO_2 -based flux products and inversion models suggest either a neutral ocean flux or a
1246 small ocean source, while the DGVMs and inversion models suggest either a small sink or
1247 source on land. The agreement between inversions and process models is significantly better
1248 for the last decade than for any previous decade (Fig. 8), although the reasons for this better
1249 agreement are still unclear.

1250 In the northern extratropics (north of 30°N) the atmospheric inversions suggest an atmosphere-
1251 to-surface sink ($S_{\text{OCEAN}}+S_{\text{LAND-ELUC}}$) for 2010-2019 of $2.9 \pm 0.6 \text{ GtC yr}^{-1}$, which is higher than the
1252 process models' estimate of $2.3 \pm 0.6 \text{ GtC yr}^{-1}$ (Fig. 8). The difference derives from the total land
1253 flux ($S_{\text{LAND-ELUC}}$) estimate, which is $1.1 \pm 0.6 \text{ GtC yr}^{-1}$ in the DGVMs compared with $1.7 \pm 0.8 \text{ GtC}$
1254 yr^{-1} in the inversion models. The GOBMs ($1.2 \pm 0.2 \text{ GtC yr}^{-1}$), inversion models ($1.2 \pm 0.2 \text{ GtC yr}^{-1}$)
1255 and pCO_2 -based flux products ($1.4 \pm 0.2 \text{ GtC yr}^{-1}$) produce similar estimates of the ocean sink.

1256 The noteworthy differences between the annual estimates produced by different data sources
1257 are as follows:

1258 (i) the southern S_{OCEAN} flux in the pCO_2 -based flux products and inversion models is
1259 higher than in the GOBMs. This might be explained by the sparse sampling of Southern
1260 Ocean surface pCO_2 observations in winter, when CO_2 outgassing occurs south of the
1261 Polar Front (Bushinsky et al., 2019), or by the uncertainty in the regional distribution of
1262 the river flux adjustment (Aumont et al., 2001, Lacroix et al., 2020) applied to pCO_2 -
1263 based flux products to isolate the anthropogenic S_{OCEAN} flux.

1264 (ii) the larger magnitude of the northern net land flux ($S_{\text{LAND-ELUC}}$) in inversion models
1265 than in the DGVMs. Discrepancies in the northern and tropical land fluxes conforms with
1266 persistent issues surrounding the quantification of the drivers of the global net land CO_2
1267 flux (Arneeth et al., 2017; Huntzinger et al., 2017) and the distribution of atmosphere-to-
1268 land fluxes between the tropics and high northern latitudes (Baccini et al., 2017; Schimel
1269 et al., 2015; Stephens et al., 2007; Ciais et al. 2019). These differences cannot be simply
1270 explained. They could either reflect a bias in the inversions or missing processes or
1271 biases in the process models, such as the lack of adequate parameterizations for land
1272 management for the DGVMs. In fact, the 6 inversions shown in Fig. 8 form two
1273 categories, one with a large northern land sink and a tropical land source and another

1274 with a moderate northern land sink and a small tropical sink (3.2.3.3). The estimated
1275 contribution of the north and its uncertainty from process models is sensitive both to
1276 the ensemble of process models used e.g. the inclusion of northern forest management
1277 in DGVMs and possibly too strong emissions from LUC (Bastos et al. 2020), and to the
1278 specifics of each inversion e.g. zonal and latitudinal transport and its covariance with
1279 seasonal fluxes (Denning et al. 1995).

1280 **3.2.3.2 Interannual Variability**

1281 The interannual variability in the southern extratropics is low because of the dominance of
1282 ocean area with low variability compared to land areas. The split between land ($S_{\text{LAND-E}_{\text{LUC}}}$) and
1283 ocean (S_{OCEAN}) shows a small contribution to variability in the south coming from the land, with
1284 no consistency between the DGVMs and the inversions or among inversions. This is expected
1285 due to the difficulty of separating exactly the land and oceanic fluxes when viewed from
1286 atmospheric observations alone. The interannual variability, calculated as the standard
1287 deviation from detrended time-series around the mean, was found to be similar in the $p\text{CO}_2$ -
1288 based flux products (0.05 to 0.10 GtC yr^{-1}) and GOBMs (0.06 to 0.17 GtC yr^{-1}) in 2010-2019
1289 (Fig. B1).

1290 Both the process models and the inversions consistently allocate more year-to-year variability
1291 of CO_2 fluxes to the tropics compared to the northern extratropics (Fig. 8). The land is the origin
1292 of most of the tropical variability, consistently among the process models and inversions. The
1293 interannual variability in the tropics is similar among the five ocean flux products (0.03 to 0.09
1294 GtC yr^{-1}) and the models (0.02 to 0.09 GtC yr^{-1} ; Sect. 3.1.3, Fig. B1). The inversions indicate
1295 that atmosphere-to-land CO_2 fluxes are more variable than atmosphere-to-ocean CO_2 fluxes in
1296 the tropics, and produce slightly higher IAV than the ocean flux products or GOBMs. With a
1297 sparsity of tropical atmospheric measurements, an aliasing of the large land flux variations onto
1298 the tropical ocean fluxes in the inversions is one likely cause of this difference.

1299 In the northern extratropics, the models, inversions, and $p\text{CO}_2$ -based flux products consistently
1300 suggest that most of the variability stems from the land (Fig. 8). Inversions, GOBMs, and $p\text{CO}_2$ -
1301 based flux products agree on the mean of S_{OCEAN} , but with a higher interannual variability in the
1302 $p\text{CO}_2$ -based flux products (0.05 to 0.08 GtC yr^{-1}) than in the GOBMs (0.04 to 0.10 GtC yr^{-1} , Fig.
1303 B1).

1304 **3.2.3.3 Atmospheric inversion models differences**

1305 The expanded ensemble of atmospheric inversions (from N=3 to N=6) allows to have a more
1306 representative sample of model-model differences e.g. in latitudinal transport and other
1307 inversion settings (Table A4). When assessed for their tropical/northern land+ocean fluxes we
1308 see a dipole arise, where three models estimate a Northern extratropical sink close to 2.5
1309 GtC/year, and the other three a sink of close to 3.5 GtC/year. The inversions resulting in a large
1310 Northern sink estimate also a tropical source. Both groups of models perform equally well on
1311 the evaluation metric of the misfit of optimized CO₂ from inversions against independent
1312 aircraft data in Fig B3 though, and resolving this difference will require the consideration and
1313 inclusion of larger volumes of semi-continuous observations of concentrations, fluxes as well as
1314 auxiliary variables collected from (tall) towers close to the surface CO₂ exchange. Improvements
1315 in model resolution and atmospheric transport realism together with expansion of the
1316 observational record (also in the data sparse Boreal Eurasian area) may help anchor the mid-
1317 latitude NH fluxes per continent. In addition, new metrics could potentially differentiate
1318 between the more and less realistic realisations of the Northern Hemisphere land sink shown in
1319 Fig.8.

1320 In previous versions of this publication, another hypothesised explanation was that differences
1321 in the prior dataset used by the inversion models, and related adjustments to posterior
1322 estimates, drove inter-model disparity. However, separate analysis has shown that the
1323 influence of the chosen prior land and ocean fluxes is minor compared to other aspects of each
1324 inversion, and the majority (5 of 6) of the inversion models presented in this update now use a
1325 consistent prior for fossil emissions (Jones et al., *in revision*; see Section 2.6).

1326 Finally, in the 2020 effort, two inverse systems (UoE and CAMS) used column CO₂ products
1327 derived from GoSAT and OCO-2, respectively. Their estimated fluxes and performance on the
1328 metrics evaluated in this work were similar to their counterparts driven by in-situ and flask
1329 observations, and hence these solutions were not included separately (as noted by Chevalier et
1330 al., 2019). Nevertheless, this convergence of solutions is an important prerequisite for the use
1331 of longer remote sensing CO₂ time series in the future, and could help to further study
1332 differences driven by observational coverage and/or sparseness of the current network. Also,
1333 column-CO₂ products are likely to be less sensitive to vertical transport differences between
1334 models, believed to be a remaining source of uncertainty (Basu et al., 2018).

1335 **3.2.4 Budget imbalance**

1336 The budget imbalance (B_{IM}) was low, -0.1 GtC yr^{-1} on average over 2010-2019, although the B_{IM}
1337 uncertainty is large (1.4 GtC yr^{-1} over the decade). Also, the B_{IM} shows significant departure
1338 from zero on yearly time scales (Fig. 4), highlighting unresolved variability of the carbon cycle,
1339 likely in the land sink (S_{LAND}), given its large year to year variability. The origin for missing annual
1340 variability is likely in the land sink (S_{LAND}), given its large year to year variability (Fig. 4e and 6b),
1341 while the decadal variability could originate from both the land and ocean sinks, given the large
1342 mismatch between the ocean models and the ocean $p\text{CO}_2$ -based flux products (Fig. 7).

1343 Although the budget imbalance is near zero for the recent decades, it could be due to
1344 compensation of errors. We cannot exclude an overestimation of CO_2 emissions, in particular
1345 from land-use change, given their large uncertainty, as has been suggested elsewhere (Piao et
1346 al., 2018), combined with an underestimate of the sinks. A larger S_{LAND} would reconcile model
1347 results with inversions estimates for fluxes in the total land during the past decade (Fig. 8; Table
1348 5). Likewise, a larger S_{OCEAN} is also possible given the higher estimates from the data-products
1349 (see section 3.1.2, Fig. 7 and 8). More integrated use of observations in the Global Carbon
1350 Budget, either on their own or for further constraining model results, should help resolve some
1351 of the budget imbalance (Peters et al., 2017; Section 4).

1352 **3.3 Global carbon budget for year 2019**

1353 **3.3.1 CO_2 emissions**

1354 Preliminary estimates of global fossil CO_2 emissions are for growth of only 0.1% between 2018
1355 and 2019 to remain at $9.7 \pm 0.5 \text{ GtC}$ in 2019 (Fig. 5), distributed among coal (39%), oil (34%),
1356 natural gas (21%), cement (4%) and others (1.5%). Compared to the previous year, emissions
1357 from coal decreased by 1.8%, while emissions from oil, natural gas, and cement increased by
1358 0.8%, 2.0%, and 3.2%, respectively. All growth rates presented are adjusted for the leap year,
1359 unless stated otherwise.

1360 In 2019, the largest absolute contributions to global fossil CO_2 emissions were from China
1361 (28%), the USA (14%), the EU (27-member states; 8%), and India (7%). These four regions
1362 account for 57% of global CO_2 emissions, while the rest of the world contributed 43% which
1363 includes aviation and marine bunker fuels (3.5% of the total). Growth rates for these countries
1364 from 2018 to 2019 were +2.2% (China), -2.6% (USA), -4.5% (EU27), and +1.0% (India), with

1365 +1.8% for the rest of the world. The per-capita fossil CO₂ emissions in 2019 were 1.3 tC person⁻¹
1366 yr⁻¹ for the globe, and were 4.4 (USA), 1.9 (China), 1.8 (EU27) and 0.5 (India) tC person⁻¹ yr⁻¹ for
1367 the four highest emitting countries (Fig. 5).

1368 The growth in emissions of 0.1% in 2019 is within the range of the projected growth of 0.6%
1369 (range of -0.2 to 1.5%) published in Friedlingstein et al. (2019) based on national emissions
1370 projections for China, the USA, the EU27, and India and projections of gross domestic product
1371 corrected for I_{FOS} trends for the rest of the world. The growth in emissions in 2019 for China,
1372 the USA, EU27, India, and the rest of the world were all within their previously projected range
1373 (Table 7).

1374 The largest absolute contributions to global CO₂ emissions from a consumption perspective
1375 were China (25%), USA (16%), the EU (10%), and India (6%) for 2016, the last year with available
1376 data. The difference between territorial and consumption emissions (the net emission transfer
1377 via international trade) has generally increased from 1990 to around 2005 and remained
1378 relatively stable afterwards until the last year available (2016; Fig. 5).

1379 The global CO₂ emissions from land-use change are estimated as 1.8 ± 0.7 GtC in 2019, slightly
1380 larger than the previous decade, which results in particular from the high peat and
1381 deforestation/degradation fires due to anomalously dry conditions in equatorial Asia
1382 (GFED4.1s, van der Werf et al., 2017) and the surge in deforestation fires in the Amazon
1383 (GFED4.1s, van der Werf et al., 2017, Aragão et al., 2020), but with low confidence in the annual
1384 change. This brings the total CO₂ emissions from fossil plus land-use change (E_{FOS}+E_{LUC}) to $11.5 \pm$
1385 0.9 GtC (42.2 ± 3.3 GtCO₂).

1386 **3.3.2 Partitioning among the atmosphere, ocean and land**

1387 The growth rate in atmospheric CO₂ concentration corresponded to 5.4 ± 0.2 GtC in 2019 (2.54
1388 ± 0.08 ppm; Fig. 4; Dlugokencky and Tans, 2020), slightly above the 2010-2019 average of $5.1 \pm$
1389 0.02 GtC yr⁻¹.

1390 The estimated ocean CO₂ sink was 2.6 ± 0.6 GtC in 2019. The multi-model mean agrees with the
1391 mean of the pCO₂-based flux products on an average increase of 0.06-0.07 GtC in 2019. Six
1392 models and three flux products show an increase of S_{OCEAN} (GOBM up to +0.30 GtC, data-
1393 product up to +0.29 GtC), while three models and two flux products show no change or a
1394 decrease of S_{OCEAN} (GOBMs down to -0.03 GtC, data-products down to -0.17 GtC; Fig. 7).

1395 The terrestrial CO₂ sink from the DGVM model ensemble was 3.1 ± 1.2 GtC in 2019, slightly
1396 below the decadal average (Fig. 4) and consistent with constraints from the rest of the budget
1397 (Table 5). Atmospheric inversions confirm a lower-than-average land sink in 2019, and
1398 consistently estimate this as an increased source from the tropical land (+0.3 GtC). The budget
1399 imbalance was +0.3 GtC in 2019, which is above the average over the last decade (Table 6). This
1400 imbalance is indicative only, given its significant year to year variability and large uncertainty
1401 (1.4 GtC yr^{-1}).

1402 **3.4 Global carbon budget projection for year 2020**

1403 **3.4.1 Fossil CO₂ emissions**

1404 We present the results from the four separate methods in Table A8, with monthly results for
1405 each country, region, and globally shown in Figure B5. The restrictions implemented in
1406 response to COVID-19 led to dramatic and unprecedented changes in society, and this caused
1407 large changes in CO₂ emissions. All countries had significant deviations from their previous
1408 emission trends.

1409 **3.4.1.1 Year To Date (YTD)**

1410 The four methods presented here use a mix of direct emissions estimates from energy
1411 consumption data to the use of proxies as indicators of changes in activity levels. Annual CO₂
1412 emissions estimates are traditionally largely derived from reported energy data, but we do not
1413 have sufficient information to say that the use of monthly energy data gives any more accurate
1414 estimates during 2020 than proxy approaches. While the GCB method is based on monthly
1415 energy consumption data, the monthly data is also subject to revisions and is incomplete.
1416 Forster et al (2020) shows the biggest reductions in all regions except the EU27. As noted in
1417 Forster et al (2020) the reductions in CO₂ emissions may be about 20% overestimated based on
1418 meteorologically adjusted NO_x observations.

1419 The YTD results (Fig. B5, Table A8) run to August for all regions and methods, except the EU27
1420 which is to June (limited by the Eurostat data used by the GCB method). To August (June) 2020,
1421 the four methods indicate fossil CO₂ emissions were down in all regions and globally. However,
1422 the background for these declines varies by countries. The EU and the US had declining
1423 emission trends before COVID-19, so the pandemic effect is on top of these existing emission
1424 reductions. In both the EU and the US, reductions in coal use have been accelerated by COVID-

1425 19. Similarly, India's emissions were in decline through 2019, but this time because of economic
1426 troubles (Andrew, 2020b), but COVID-19 is potentially superimposed on the longer term trend
1427 of increasing emissions in India. In contrast, China and the Rest of the World have the COVID-19
1428 effect on the top of rising emissions. China has lower reductions, but this may also indicate that
1429 the full impact of the COVID-19 restrictions occurred earlier and the economy has had a longer
1430 time to recover.

1431 Based on the three studies providing sufficient data, from January to August, global emissions
1432 may have declined around 8% (median, based on model estimates of -8.0% UEA, -8.1% Carbon
1433 Monitor, -14.3% Priestley Centre). This range between estimates does not include the
1434 uncertainty inherent in each method, which would increase the spread.

1435 **3.4.1.2 2020 projections**

1436 The full-year projection for 2020 must necessarily be interpreted cautiously. Only Le Quéré et al
1437 (2020) include a formal projection, by assuming confinement measures currently in place are in
1438 place for six weeks before they ease in each country. Forster et al (2020) use a simple
1439 extrapolation, assuming the declines in emissions from their baselines remain at 66% of the
1440 level over the last 30 days with estimates. Liu et al (2020) and the GCB method did not perform
1441 a projection for 2020, and for purposes of comparison we use a simple approach to
1442 extrapolating their observations by assuming the remaining months of the year change by the
1443 same relative amount compared to 2019 as the final month of observations.

1444 Based on these assumptions, the countries and regions considered are all expected to see a
1445 decline in annual total emissions, with the potential exception of China which may have a slight
1446 increase according to Carbon Monitor and the GCB method (Fig. B5). The year 2020 is behaving
1447 in many ways entirely differently to any year in history, and the confidence in the 2020
1448 projection is therefore currently low, due to both the spread in results and the uncertain
1449 developments of the disease itself, strength of future societal and industrial restrictions, and
1450 stimulus packages throughout the remainder of 2020. The largest source of uncertainty comes
1451 from the emissions in China, because of the limited available information both on monthly
1452 emissions and for proxy data, and emissions for the RoW, because it represents around 40% of
1453 the world's emissions in aggregate.

1454 Based on the median value of the four methods considered, global emissions may decline by
1455 about 6% in 2020 (-5.6% UEA, -6.0% GCB, -6.6% Carbon Monitor, -12.7% Priestley Centre), with
1456 additional uncertainty from each method on top of this (Fig B5, Table A8). Using a purely GDP-
1457 based projection, based on the IMF GDP forecast as of June 2020, and assuming the 10-year
1458 trend in CO₂/GDP continues in 2020, emissions would decline 7.5% – well within the range of
1459 other estimates. In April 2020, the IEA forecasted a drop of 8% in fossil energy emissions (IEA,
1460 2020). The decrease in emissions for the full year 2020 appears more pronounced in the US,
1461 EU27 and India, partly due to pre-existing trends. In contrast the decrease in emissions appears
1462 least pronounced in China, where restrictions measures associated with COVID-19 occurred
1463 early in the year and lockdown measures were more limited in time.

1464 **3.4.1.3 Synthesis**

1465 Given a negative median growth rate of about -6% across methods, global fossil CO₂ emissions
1466 (E_{FOS}) in 2020 would be around 9.4 GtC (34.3 GtCO₂) in 2020 (Table A8). These figures do not
1467 include the uncertainty from this method in projecting 2020 emissions.

1468 Our preliminary estimates of fire emissions in deforestation zones and Amazon deforestation
1469 rates indicate that emissions from land-use change (E_{LUC}) for 2020 are similar to the 2010-2019
1470 average (Sec. 2.2.4). We therefore expect E_{LUC} emissions of around 1.6 GtC in 2020.

1471 We hence project global total anthropogenic CO₂ emissions from fossil and land use changes to
1472 be around 11.0 GtC (40.3 GtCO₂) in 2020.

1473 **3.4.2 Partitioning among the atmosphere, ocean and land**

1474 The 2020 growth in atmospheric CO₂ concentration (G_{ATM}) is projected to be about 4.6 GtC (2.2
1475 ppm) based on GLO observations until the end of June 2020, bringing the atmospheric CO₂
1476 concentration to an expected level of 412 ppm averaged over the year. Combining projected
1477 E_{FOS}, E_{LUC} and G_{ATM} suggests a combined land and ocean sink (S_{LAND} + S_{OCEAN}) of about 6.4 GtC for
1478 2020. Although each term has large uncertainty, the oceanic sink S_{OCEAN} has generally low
1479 interannual variability and is likely to remain close to its 2019 value of around 2.6 GtC, leaving a
1480 rough estimated land sink S_{LAND} (including any budget imbalance) of around 3.8 GtC,
1481 substantially above the 2019 estimate.

1482 **3.5 Cumulative sources and sinks**

1483 Cumulative historical sources and sinks are estimated as in Eq. (1) with semi-independent
1484 estimates for each term and a global carbon budget imbalance. Cumulative fossil CO₂ emissions
1485 for 1850-2019 were 445 ± 20 GtC for E_{FOS} and 210 ± 60 GtC for E_{LUC} (Table 8; Fig. 9), for a total
1486 of 650 ± 65 GtC. The cumulative emissions from E_{LUC} are particularly uncertain, with large
1487 spread among individual estimates of 150 GtC (H&N), 275 GtC (BLUE), and 200 GtC (OSCAR) for
1488 the three bookkeeping models and a similar wide estimate of 200 ± 60 GtC for the DGVMs.
1489 These estimates are consistent with indirect constraints from vegetation biomass observations
1490 (Li et al., 2017), but given the large spread a best estimate is difficult to ascertain.

1491 Emissions during the period 1850-2019 were partitioned among the atmosphere (265 ± 5 GtC;
1492 40%), ocean (160 ± 20 GtC; 25%), and the land (210 ± 55 GtC; 32%). This cumulative land sink is
1493 broadly equal to the cumulative land-use emissions, making the global land near neutral over
1494 the 1850-2019 period. The use of nearly independent estimates for the individual terms shows
1495 a cumulative budget imbalance of 20 GtC (3%) during 1850-2019 (Fig. 2), which, if correct,
1496 suggests that emissions are too high by the same proportion or that the land or ocean sinks are
1497 underestimated. The bulk of the imbalance could originate from the estimation of large E_{LUC}
1498 between the mid 1920s and the mid 1960s which is unmatched by a growth in atmospheric CO₂
1499 concentration as recorded in ice cores (Fig. 3). The known loss of additional sink capacity of 30-
1500 40 GtC due to reduced forest cover has not been accounted for in our method and would
1501 further exacerbate the budget imbalance (Section 2.7.4).

1502 Cumulative emissions through to year 2020 increase to 655 ± 65 GtC (2340 ± 240 GtCO₂), with
1503 about 70% contribution from E_{FOS} and about 30% contribution from E_{LUC}. Cumulative emissions
1504 and their partitioning for different periods are provided in Table 8.

1505 Given the large and persistent uncertainties in historical cumulative emissions, we suggest
1506 extreme caution is needed if using this estimate to determine the remaining cumulative CO₂
1507 emissions consistent with an ambition to stay below a given temperature limit (Millar et al.,
1508 2017; Rogelj et al., 2016, 2019).

1509 **4 Discussion**

1510 Each year when the global carbon budget is published, each flux component is updated for all
1511 previous years to consider corrections that are the result of further scrutiny and verification of

1512 the underlying data in the primary input data sets. Annual estimates may be updated with
1513 improvements in data quality and timeliness (e.g. to eliminate the need for extrapolation of
1514 forcing data such as land-use). Of all terms in the global budget, only the fossil CO₂ emissions
1515 and the growth rate in atmospheric CO₂ concentration are based primarily on empirical inputs
1516 supporting annual estimates in this carbon budget. The carbon budget imbalance, yet an
1517 imperfect measure, provides a strong indication of the limitations in observations in
1518 understanding and representing processes in models, and/or in the integration of the carbon
1519 budget components.

1520 The persistent unexplained variability in the carbon budget imbalance limits our ability to verify
1521 reported emissions (Peters et al., 2017) and suggests we do not yet have a complete
1522 understanding of the underlying carbon cycle processes. Resolving most of this unexplained
1523 variability should be possible through different and complementary approaches. First, as
1524 intended with our annual updates, the imbalance as an error term is reduced by improvements
1525 of individual components of the global carbon budget that follow from improving the
1526 underlying data and statistics and by improving the models through the resolution of some of
1527 the key uncertainties detailed in Table 9. Second, additional clues to the origin and processes
1528 responsible for the variability in the budget imbalance could be obtained through a closer
1529 scrutiny of carbon variability in light of other Earth system data (e.g. heat balance, water
1530 balance), and the use of a wider range of biogeochemical observations to better understand
1531 the land-ocean partitioning of the carbon imbalance (e.g. oxygen, carbon isotopes). Finally,
1532 additional information could also be obtained through higher resolution and process knowledge
1533 at the regional level, and through the introduction of inferred fluxes such as those based on
1534 satellite CO₂ retrievals. The limit of the resolution of the carbon budget imbalance is yet
1535 unclear, but most certainly not yet reached given the possibilities for improvements that lie
1536 ahead.

1537 The assessment of the GOBMs used for S_{OCEAN} with flux products based on observations
1538 highlights substantial discrepancy in the Southern Ocean (Figure 8, Hauck et al., 2020). The
1539 sparse data coverage of pCO₂ observations in the Southern compared to the Northern
1540 Hemisphere (Bakker et al., 2016), leads to substantially higher uncertainty in the S_{OCEAN}
1541 estimate for the Southern Hemisphere (Watson et al., 2020). This discrepancy points to the
1542 need for increased high-quality pCO₂ observations especially in the Southern Ocean. Further

1543 uncertainty stems from the regional distribution of the river flux adjustment term being based
1544 on one model study yielding the largest riverine outgassing flux south of 20°S (Aumont et al.,
1545 2001), with a recent study questioning this distribution (Lacroix et al., 2020). The data-products
1546 suggest an underestimation of variability in the GOBMs globally and consequently, the
1547 variability in S_{OCEAN} appears to be underestimated. The size of the underestimation of the
1548 amplitude of interannual variability (order of $<0.1 \text{ GtC yr}^{-1}$, A-IAV, see Fig. B1) could account for
1549 some of the budget imbalance, but not all. The assessment of the net land-atmosphere
1550 exchange derived from land sink and net land-use change flux with atmospheric inversions also
1551 shows substantial discrepancy, particularly for the estimate of the total land flux over the
1552 northern extra-tropics in the past decade. This discrepancy highlights the difficulty to quantify
1553 complex processes (CO_2 fertilisation, nitrogen deposition, N fertilisers, climate change and
1554 variability, land management, etc.) that collectively determine the net land CO_2 flux. Resolving
1555 the differences in the Northern Hemisphere land sink will require the consideration and
1556 inclusion of larger volumes of observations (Section 3.2.3).

1557 Estimates of E_{LUC} suffer from a range of intertwined issues, including the poor quality of
1558 historical land-cover and land-use change maps, the rudimentary representation of
1559 management processes in most models, and the confusion in methodologies and boundary
1560 conditions used across methods (e.g. Arneeth et al., 2017; Pongratz et al., 2014, see also Section
1561 2.7.4 on the loss of sink capacity). Uncertainties in current and historical carbon stocks in soils
1562 and vegetation also add uncertainty in the LUC flux estimates. Unless a major effort to resolve
1563 these issues is made, little progress is expected in the resolution of E_{LUC} . This is particularly
1564 concerning given the growing importance of E_{LUC} for climate mitigation strategies, and the large
1565 issues in the quantification of the cumulative emissions over the historical period that arise
1566 from large uncertainties in E_{LUC} .

1567 As introduced in 2018, we provide metrics for the evaluation of the ocean and land models and
1568 the atmospheric inversions. These metrics expand the use of observations in the global carbon
1569 budget, helping 1) to support improvements in the ocean and land carbon models that produce
1570 the sink estimates, and 2) to constrain the representation of key underlying processes in the
1571 models and to allocate the regional partitioning of the CO_2 fluxes. However, GOBMs have
1572 changed little since the introduction of the ocean model evaluation. This is an initial step

1573 towards the introduction of a broader range of observations that we hope will support
1574 continued improvements in the annual estimates of the global carbon budget.

1575 We assessed before that a sustained decrease of -1% in global emissions could be detected at
1576 the 66% likelihood level after a decade only (Peters et al., 2017). Similarly, a change in
1577 behaviour of the land and/or ocean carbon sink would take as long to detect, and much longer
1578 if it emerges more slowly. To continue reducing the carbon imbalance on annual to decadal
1579 time scales, regionalising the carbon budget, and integrating multiple variables are powerful
1580 ways to shorten the detection limit and ensure the research community can rapidly identify
1581 issues of concern in the evolution of the global carbon cycle under the current rapid and
1582 unprecedented changing environmental conditions.

1583 **5 Conclusions**

1584 The estimation of global CO₂ emissions and sinks is a major effort by the carbon cycle research
1585 community that requires a careful compilation and synthesis of measurements, statistical
1586 estimates and model results. The delivery of an annual carbon budget serves two purposes.
1587 First, there is a large demand for up-to-date information on the state of the anthropogenic
1588 perturbation of the climate system and its underpinning causes. A broad stakeholder
1589 community relies on the data sets associated with the annual carbon budget including
1590 scientists, policy makers, businesses, journalists, and non-governmental organizations engaged
1591 in adapting to and mitigating human-driven climate change. Second, over the last decade we
1592 have seen unprecedented changes in the human and biophysical environments (e.g. changes in
1593 the growth of fossil fuel emissions, impact of COVID-19 pandemic, Earth's warming, and
1594 strength of the carbon sinks), which call for frequent assessments of the state of the planet, a
1595 better quantification of the causes of changes in the contemporary global carbon cycle, and an
1596 improved capacity to anticipate its evolution in the future. Building this scientific understanding
1597 to meet the extraordinary climate mitigation challenge requires frequent, robust, transparent

1598 and traceable data sets and methods that can be scrutinized and replicated. This paper via
1599 'living data' helps to keep track of new budget updates.

1600 **6 Data availability**

1601 The data presented here are made available in the belief that their wide dissemination will lead
1602 to greater understanding and new scientific insights of how the carbon cycle works, how
1603 humans are altering it, and how we can mitigate the resulting human-driven climate change.
1604 The free availability of these data does not constitute permission for publication of the data.
1605 For research projects, if the data are essential to the work, or if an important result or
1606 conclusion depends on the data, co-authorship may need to be considered for the relevant
1607 data providers. Full contact details and information on how to cite the data shown here are
1608 given at the top of each page in the accompanying database and summarised in Table 2.

1609 The accompanying database includes two Excel files organised in the following spreadsheets:

1610 File [Global_Carbon_Budget_2020v1.0.xlsx](#) includes the following:

- 1611 1. Summary
- 1612 2. The global carbon budget (1959-2019);
- 1613 3. Global CO₂ emissions from fossil fuels and cement production by fuel type, and the per-
1614 capita emissions (1959-2019);
- 1615 4. CO₂ emissions from land-use change from the individual methods and models (1959-2019);
- 1616 5. Ocean CO₂ sink from the individual ocean models and pCO₂-based products (1959-2019);
- 1617 6. Terrestrial CO₂ sink from the DGVMs (1959-2019);
- 1618 7. Additional information on the historical global carbon budget prior to 1959 (1750-2019).

1619 File [National_Carbon_Emissions_2020v1.0.xlsx](#) includes the following:

- 1620 1. Summary
- 1621 2. Territorial country CO₂ emissions from fossil CO₂ emissions (1959-2019) from CDIAC with
1622 UNFCCC data overwritten where available, extended to 2019 using BP data;
- 1623 3. Consumption country CO₂ emissions from fossil CO₂ emissions and emissions transfer from
1624 the international trade of goods and services (1990-2016) using CDIAC/UNFCCC data
1625 (worksheet 3 above) as reference;
- 1626 4. Emissions transfers (Consumption minus territorial emissions; 1990-2016);

- 1627 5. Country definitions;
1628 6. Details of disaggregated countries;
1629 7. Details of aggregated countries.

1630 Both spreadsheets are published by the Integrated Carbon Observation System (ICOS) Carbon
1631 Portal and are available at <https://doi.org/10.18160/gcp-2020> (Friedlingstein et al., 2020).
1632 National emissions data are also available from the Global Carbon Atlas
1633 (<http://www.globalcarbonatlas.org/>, last access: 27 September 2020).

1634 **Author contributions.** PF, MOS, MWJ, CLQ, RMA, JH, GPP, WP, JP, SS, AO, JGC, PC and RBJ
1635 designed the study, conducted the analysis, and wrote the paper. RMA, GPP and JIK produced
1636 the emissions and their uncertainties, 2020 emission projections, and analysed the emissions
1637 data. DG and GM provided emission data. PPT provided key atmospheric CO₂ data. WP, PC, FC,
1638 CR, NC, YN, PIP and LF provided an updated atmospheric inversion, developed the protocol and
1639 produced the evaluation. JP, KH, SB, TG and RAH provided updated bookkeeping land-use
1640 change emissions. LPC, LEOCA, and GRvdW provided forcing data for land-use change. AA, VH,
1641 AKJ, EJ, EK, SL, DLL, JRM, JEMSN, BP, HT, NV, APW, AJW, WY, XY and SZ provided an update of a
1642 DGVM. IH provided the climate forcing data for the DGVMs. ER provided the evaluation of the
1643 DGVMs. JH, LBo, NG, TI, AL, LR, JS, RS, and DW provided an update of a GOBM. MG, LG, PL, CR,
1644 and AJW provided an update of an ocean flux product. SA, NRB, MB, AB, HCB, WE, TG, KK, VK,
1645 NL, NM, DRM, SN, KO, AO, TO, DP, IS, AJS, TT, BT, and RW provided ocean pCO₂ measurements
1646 for the year 2019, with synthesis by AO and KO. PF, MOS, and MWJ revised all figures, tables,
1647 text and/or numbers to ensure the update is clear from the 2019 edition and in phase with the
1648 globalcarbonatlas.org.
1649

1650

1651 **Competing interests.** The authors declare that they have no conflict of interest.

1652 **Acknowledgements.** We thank all people and institutions who provided the data used in this
1653 carbon budget; I.G.C. Ashton, Matthew Chamberlain, Ed Chan, Laique Djeutchouang, Christian

1654 Ethé, Liang Feng, M. Fortier, L. Goddijn-Murphy, T. Holding, Joe Melton, Tristan Quaife, Marine
1655 Remaud, Shijie Shu, J.D. Shutler, Anthony Walker, Ulrich Weber, and D.K. Woolf for their
1656 involvement in the development, use and analysis of the models and data-products used here.
1657 We thank Ed Dlugokencky for providing atmospheric CO₂ measurements; We thank Benjamin
1658 Pfeil, Steve Jones, Rocío Castaño-Primo and Maren Karlsen of the Ocean Thematic Centre of the
1659 EU Integrated Carbon Observation System (ICOS) Research Infrastructure for their contribution,
1660 as well as Karl Smith of NOAA's Pacific Marine Environmental Laboratory; and Kim Currie, Joe
1661 Salisbury, Doug Vandermark, Chris Hunt, Douglas Wallace and Dariia Atamanchuck, who
1662 contributed to the provision of ocean pCO₂ observations for the year 2019 (see Table A5). This
1663 is NOAA-PMEL contribution number 5167. We thank the institutions and funding agencies
1664 responsible for the collection and quality control of the data in SOCAT, and the International
1665 Ocean Carbon Coordination Project (IOCCP) for its support. We thank FAO and its member
1666 countries for the collection and free dissemination of data relevant to this work. We thank data
1667 providers ObsPack GLOBALVIEWplus v5.0 and NRT v5.2 for atmospheric CO₂ observations. We
1668 thank Trang Chau who produced the CMEMS pCO₂-based ocean flux data and designed the
1669 system together with MG, Anna Denvil-Sommer, and FC. We thank the individuals and
1670 institutions that provided the databases used for the model evaluations introduced here, and
1671 Nigel Hawtin for producing Figure 2 and Figure 9. We thank Fortunat Joos, Samar Khatiwala and
1672 Timothy DeVries for providing historical data. We thank all people and institutions who
1673 provided the data used in this carbon budget and the Global Carbon Project members for their
1674 input throughout the development of this update. Finally, we thank all funders who have
1675 supported the individual and joint contributions to this work (see Table A9), as well as the
1676 reviewers of this manuscript and previous versions, and the many researchers who have
1677 provided feedback.

1678 **References**

- 1679 Amante, C. and Eakins, B. W.: ETOPO1 1 Arc-Minute Global Relief Model: Procedures, Data
1680 Sources and Analysis. NOAA Technical Memorandum NESDIS NGDC-24. National
1681 Geophysical Data Center, NOAA. doi:10.7289/V5C8276M, 2009.
- 1682 Andres, R. J., Boden, T. A., Bréon, F. M., Ciais, P., Davis, S., Erickson, D., Gregg, J. S.,
1683 Jacobson, A., Marland, G., Miller, J., Oda, T., Olivier, J. G. J., Raupach, M. R., Rayner, P.
1684 and Treanton, K.: A synthesis of carbon dioxide emissions from fossil-fuel combustion,
1685 Biogeosciences, doi:10.5194/bg-9-1845-2012, 2012.
- 1686 Andres, R. J., Boden, T. A. and Higdon, D.: A new evaluation of the uncertainty associated
1687 with CDIAC estimates of fossil fuel carbon dioxide emission, *Tellus Ser. B-Chemical*
1688 *Phys. Meteorol.*, 66, 23616, doi:ARTN 2361610.3402/tellusb.v66.23616, 2014.
- 1689 Andrew, R. M.: Global CO₂ emissions from cement production, 1928–2018, *Earth Syst. Sci.*
1690 *Data*, 11(4), 1675–1710, doi:10.5194/essd-11-1675-2019, 2019.
- 1691 Andrew, R. M.: A comparison of estimates of global carbon dioxide emissions from fossil
1692 carbon sources, *Earth Syst. Sci. Data*, 12(2), 1437–1465, doi:10.5194/essd-12-1437-
1693 2020, 2020a.
- 1694 Andrew, R. M.: Timely estimates of India’s annual and monthly fossil CO₂ emissions, *Earth*
1695 *Syst. Sci. Data Discuss.*, doi:10.5194/essd-2020-152, 2020b.
- 1696 Andrew, R. M. and Peters, G. P.: A Multi-Region Input-Output Table Based on the Global
1697 Trade Analysis Project Database (Gtap-Mrio), *Econ. Syst. Res.*, 25(1), 99–121,
1698 doi:10.1080/09535314.2012.761953, 2013.
- 1699 Aragão, L. E. O. C., Junior, C. H. L. S., Junior, C. H. L. S. and Anderson, L. O.: O desafio do
1700 Brasil para conter o desmatamento e as queimadas na Amazônia durante a pandemia
1701 por COVID-19 em 2020: implicações ambientais, sociais e sua governança, available

1702 at: <https://doi.org/10.13140/RG.2.2.17256.49921>, São José dos Campos. [online]
1703 Available from: Instituto Nacional de Pesquisas Espaciais, 2020.

1704 Archer, D., Eby, M., Brovkin, V., Ridgwell, A., Cao, L., Mikolajewicz, U., Caldeira, K.,
1705 Matsumoto, K., Munhoven, G., Montenegro, A. and Tokos, K.: Atmospheric Lifetime
1706 of Fossil Fuel Carbon Dioxide, *Annu. Rev. Earth Planet. Sci.*, 37(1), 117–134,
1707 doi:10.1146/annurev.earth.031208.100206, 2009.

1708 Arneeth, A., Sitch, S., Pongratz, J., Stocker, B. D., Ciais, P., Poulter, B., Bayer, A. D., Bondeau,
1709 A., Calle, L., Chini, L. P., Gasser, T., Fader, M., Friedlingstein, P., Kato, E., Li, W.,
1710 Lindeskog, M., Nabel, J. E. M. S., Pugh, T. A. M., Robertson, E., Viovy, N., Yue, C. and
1711 Zaehle, S.: Historical carbon dioxide emissions caused by land-use changes are
1712 possibly larger than assumed, *Nat. Geosci.*, 10(2), 79–84, doi:10.1038/ngeo2882,
1713 2017.

1714 Arora, V. K., Boer, G. J., Christian, J. R., Curry, C. L., Denman, K. L., Zahariev, K., Flato, G. M.,
1715 Scinocca, J. F., Merryfield, W. J. and Lee, W. G.: The Effect of Terrestrial
1716 Photosynthesis Down Regulation on the Twentieth-Century Carbon Budget Simulated
1717 with the CCCma Earth System Model, *J. Clim.*, 22(22), 6066–6088,
1718 doi:10.1175/2009jcli3037.1, 2009.

1719 Aumont, O., Orr, J. C., Monfray, P., Ludwig, W., Amiotte-Suchet, P. and Probst, J. L.:
1720 Riverine-driven interhemispheric transport of carbon, *Global Biogeochem. Cycles*,
1721 15(2), 393–405, doi:10.1029/1999GB001238, 2001.

1722 Aumont, O., Ethé, C., Tagliabue, A., Bopp, L. and Gehlen, M.: PISCES-v2: an ocean
1723 biogeochemical model for carbon and ecosystem studies, *Geosci. Model Dev.*, 8(8),
1724 2465–2513, doi:10.5194/gmd-8-2465-2015, 2015.

1725 Avitabile, V., Herold, M., Heuvelink, G. B. M., Lewis, S. L., Phillips, O. L., Asner, G. P.,

1726 Armston, J., Ashton, P. S., Banin, L., Bayol, N., Berry, N. J., Boeckx, P., de Jong, B. H. J.,
1727 DeVries, B., Girardin, C. A. J., Kearsley, E., Lindsell, J. A., Lopez-Gonzalez, G., Lucas, R.,
1728 Malhi, Y., Morel, A., Mitchard, E. T. A., Nagy, L., Qie, L., Quinones, M. J., Ryan, C. M.,
1729 Ferry, S. J. W., Sunderland, T., Laurin, G. V., Gatti, R. C., Valentini, R., Verbeeck, H.,
1730 Wijaya, A. and Willcock, S.: An integrated pan-tropical biomass map using multiple
1731 reference datasets, *Glob. Chang. Biol.*, 22(4), 1406–1420, doi:10.1111/gcb.13139,
1732 2016.

1733 Baccini, A., Walker, W., Carvalho, L., Farina, M., Sulla-Menashe, D. and Houghton, R. A.:
1734 Tropical forests are a net carbon source based on aboveground measurements of gain
1735 and loss, *Science (80-.)*, 358(6360), 230–234, doi:10.1126/science.aam5962, 2017.

1736 Bakker, D. C. E., Pfeil, B., Landa, C. S., Metz, N., O'Brien, K. M., Olsen, A., Smith, K., Cosca,
1737 C., Harasawa, S., Jones, S. D., Nakaoka, S., Nojiri, Y., Schuster, U., Steinhoff, T.,
1738 Sweeney, C., Takahashi, T., Tilbrook, B., Wada, C., Wanninkhof, R., Alin, S. R.,
1739 Balestrini, C. F., Barbero, L., Bates, N. R., Bianchi, A. A., Bonou, F., Boutin, J., Bozec, Y.,
1740 Burger, E. F., Cai, W. J., Castle, R. D., Chen, L. Q., Chierici, M., Currie, K., Evans, W.,
1741 Featherstone, C., Feely, R. A., Fransson, A., Goyet, C., Greenwood, N., Gregor, L.,
1742 Hankin, S., Hardman-Mountford, N. J., Harlay, J., Hauck, J., Hoppema, M., Humphreys,
1743 M. P., Hunt, C., Huss, B., Ibanhez, J. S. P., Johannessen, T., Keeling, R., Kitidis, V.,
1744 Kortzinger, A., Kozyr, A., Krasakopoulou, E., Kuwata, A., Landschutzer, P., Lauvset, S.
1745 K., Lefevre, N., Lo Monaco, C., Manke, A., Mathis, J. T., Merlivat, L., Millero, F. J.,
1746 Monteiro, P. M. S., Munro, D. R., Murata, A., Newberger, T., Omar, A. M., Ono, T.,
1747 Paterson, K., Pearce, D., Pierrot, D., Robbins, L. L., Saito, S., Salisbury, J., Schlitzer, R.,
1748 Schneider, B., Schweitzer, R., Sieger, R., Skjelvan, I., Sullivan, K. F., Sutherland, S. C.,
1749 Sutton, A. J., Tadokoro, K., Telszewski, M., Tuma, M., van Heuven, S. M. A. C.,

1750 Vandemark, D., Ward, B., Watson, A. J. and Xu, S. Q.: A multi-decade record of high-
1751 quality fCO₂ data in version 3 of the Surface Ocean CO₂ Atlas (SOCAT), *Earth Syst.*
1752 *Sci. Data*, 8(2), 383–413, doi:10.5194/essd-8-383-2016, 2016.

1753 Bakker, D. C. E. , Alin, S. R. , Bates, N., Becker, M., Castaño-Primo, R., Cosca, C. E. , Cronin,
1754 M., Kadono, K., Kozyr, A., Lauvset, S. K. , Metzl, N., Munro, D. R. , Nakaoka, S.,
1755 O’Brien, K. M. , Ólafsson, J., Olsen, A., Pfeil, B., Pierrot, D., Smith, K., Sutton, A. J. ,
1756 Takahashi, T., Tilbrook, B., Wanninkhof, R., Andersson, A., Atamanchuk, D., Benoit-
1757 Cattin, A., Bott, R. B., F., E., Cai, W.-J., Cantoni, C., Collins, A., Corredor, J. E. , Cronin,
1758 M. F. , Cross, J. N. , Currie, K. I. , De Carlo, E. H. , DeGrandpre, M. D. , Dietrich, C.,
1759 Emerson, S., Enright, M. P. , Evans, W., Feely, R. A. , García-Ibáñez, M. I. , Gkritzalis,
1760 T., Glockzin, M., Hales, B., Hartman, S. E. , Hashida, G., Herndon, J., Howden, S. D. ,
1761 Humphreys, M. P. , Hunt, C. W. , Jones, S. D. , Kim, S., Kitidis, V., Landa, C. S. ,
1762 Landschützer, P., Lebon, G. T. , Lefèvre, N., Lo Monaco, C., Luchetta, A., Maenner
1763 Jones, S., Manke, A. B. , Manzello, D., Mears, P., Mickett, J., Monacci, N. M. , Morell,
1764 J. M. , Musielewicz, S., Newberger, T., Newton, J., Noakes, S., Noh, J.-H., Nojiri, Y.,
1765 Ohman, M., Ólafsdóttir, Rósa;, S., Omar, A. M. , Ono, T., Osborne, J., Plueddemann,
1766 A. J. , Rehder, G., Sabine, C. L. , Salisbury, J. E. , Schlitzer, R., Send, U., Skjelvan, I.,
1767 Sparnocchia, S., Steinhoff, T., Sullivan, K. F. , Sutherland, S. C. , Sweeney, C.,
1768 Tadokoro, K., Tanhua, T., Telszewski, M., Tomlinson, M., Tribollet, A., Trull, T.,
1769 Vandemark, D., Wada, C., Wallace, D. W. R. , Weller, R. A. . and Woosley, R. J.:
1770 Surface Ocean CO₂ Atlas Database Version 2020 (SOCATv2020) (NCEI Accession
1771 0210711). NOAA National Centers for Environmental Information. Available at:
1772 <https://doi.org/10.25921/4xkx-ss49>. Last accessed: 27 September 2020, ,
1773 doi:<https://doi.org/10.25921/4xkx-ss49>, 2020.

1774 Ballantyne, A. P., Alden, C. B., Miller, J. B., Tans, P. P. and White, J. W. C.: Increase in
1775 observed net carbon dioxide uptake by land and oceans during the past 50 years,
1776 Nature, 488(7409), 70–72, doi:10.1038/nature11299, 2012.

1777 Ballantyne, A. P., Andres, R., Houghton, R., Stocker, B. D., Wanninkhof, R., Anderegg, W.,
1778 Cooper, L. A., DeGrandpre, M., Tans, P. P., Miller, J. B., Alden, C. and White, J. W. C.:
1779 Audit of the global carbon budget: Estimate errors and their impact on uptake
1780 uncertainty, Biogeosciences, 12(8), 2565–2584, doi:10.5194/bg-12-2565-2015, 2015.

1781 Bastos, A., O’Sullivan, M., Ciais, P., Makowski, D., Sitch, S., Friedlingstein, P., Chevallier, F.,
1782 Rödenbeck, C., Pongratz, J., Luijkx, I. T., Patra, P. K., Peylin, P., Canadell, J. G.,
1783 Lauerwald, R., Li, W., Smith, N. E., Peters, W., Goll, D. S., Jain, A. K., Kato, E., Lienert,
1784 S., Lombardozzi, D. L., Haverd, V., Nabel, J. E. M. S., Poulter, B., Tian, H., Walker, A. P.
1785 and Zaehle, S.: Sources of Uncertainty in Regional and Global Terrestrial CO₂
1786 Exchange Estimates, Global Biogeochem. Cycles, 34(2), 1–21,
1787 doi:10.1029/2019GB006393, 2020.

1788 Berthet, S., Séférian, R., Bricaud, C., Chevallier, M., Voltaire, A. and Ethé, C.: Evaluation of
1789 an Online Grid-Coarsening Algorithm in a Global Eddy-Admitting Ocean
1790 Biogeochemical Model, J. Adv. Model. Earth Syst., 11(6), 1759–1783,
1791 doi:10.1029/2019MS001644, 2019.

1792 Best, M. J., Pryor, M., Clark, D. B., Rooney, G. G., Essery, R. . L. H., Ménard, C. B., Edwards,
1793 J. M., Hendry, M. A., Porson, A., Gedney, N., Mercado, L. M., Sitch, S., Blyth, E.,
1794 Boucher, O., Cox, P. M., Grimmond, C. S. B. and Harding, R. J.: The Joint UK Land
1795 Environment Simulator (JULES), model description – Part 1: Energy and water fluxes,
1796 Geosci. Model Dev., 4(3), 677–699, doi:10.5194/gmd-4-677-2011, 2011.

1797 BP: BP Statistical Review of World Energy June 2020, available at:

1798 <https://www.bp.com/en/global/corporate/energy-economics/statistical-review-of->
1799 [world-energy.html](https://www.bp.com/en/global/corporate/energy-economics/statistical-review-of-world-energy.html), last access: 27 September 2020., 2020.

1800 Broecker, W. S., Spencer, D. W. and Craig, H. C.: GEOSECS Pacific Expedition: Hydrographic
1801 data 1973-1974, available at: <https://doi.org/10.1594/PANGAEA.824127>, last access:
1802 27 September 2020., 1982.

1803 Bruno, M. and Joos, F.: Terrestrial carbon storage during the past 200 years: A Monte Carlo
1804 Analysis of CO₂ data from ice core and atmospheric measurements, *Global*
1805 *Biogeochem. Cycles*, 11(1), 111–124, doi:10.1029/96GB03611, 1997.

1806 Buitenhuis, E. T., Hashioka, T. and Le Quéré, C.: Combined constraints on global ocean
1807 primary production using observations and models, *Global Biogeochem. Cycles*, 27(3),
1808 847–858, doi:10.1002/gbc.20074, 2013.

1809 Bushinsky, S. M., Landschützer, P., Rödenbeck, C., Gray, A. R., Baker, D., Mazloff, M. R.,
1810 Resplandy, L., Johnson, K. S. and Sarmiento, J. L.: Reassessing Southern Ocean Air -
1811 Sea CO₂ Flux Estimates With the Addition of Biogeochemical Float Observations
1812 *Global Biogeochemical Cycles*, , 1370–1388, doi:10.1029/2019GB006176, 2019.

1813 Canadell, J. G., Le Quéré, C., Raupach, M. R., Field, C. B., Buitenhuis, E. T., Ciais, P., Conway,
1814 T. J., Gillett, N. P., Houghton, R. A. and Marland, G.: Contributions to accelerating
1815 atmospheric CO₂ growth from economic activity, carbon intensity, and efficiency of
1816 natural sinks, *Proc. Natl. Acad. Sci.*, 104(47), 18866–18870,
1817 doi:10.1073/pnas.0702737104, 2007.

1818 Cao, Z., Myers, R. J., Lupton, R. C., Duan, H., Sacchi, R., Zhou, N., Reed Miller, T., Cullen, J.
1819 M., Ge, Q. and Liu, G.: The sponge effect and carbon emission mitigation potentials of
1820 the global cement cycle, *Nat. Commun.*, 11(1), 1–9, doi:10.1038/s41467-020-17583-
1821 w, 2020.

1822 Carbontracker Team: obspack_co2_1_NRT_v5.2_2020-06-03, available at:
1823 https://www.esrl.noaa.gov/gmd/ccgg/obspack/release_notes.html, last access: 27
1824 September 2020., 2020.

1825 CGADIP: obspack_co2_1_GLOBALVIEWplus_v5.0_2019-08-12, available at:
1826 https://www.esrl.noaa.gov/gmd/ccgg/obspack/release_notes.html, last access: 27
1827 September 2020., 2020.

1828 Chatfield, C.: The Holt-Winters Forecasting Procedure, *Appl. Stat.*, 27(3), 264–279,
1829 doi:10.2307/2347162, 1978.

1830 Chau, T. T. ., Gehlen, M. and Chevallier, F.: Global Ocean Surface Carbon Product
1831 MULTIOBS_GLO_BIO_CARBON_SURFACE_REP_015_008, E.U. Copernicus Marine
1832 Service Information, available at:
1833 [https://resources.marine.copernicus.eu/?option=com_csw&view=details&product_id](https://resources.marine.copernicus.eu/?option=com_csw&view=details&product_id=MULTIOBS_G)
1834 [=MULTIOBS_G](https://resources.marine.copernicus.eu/?option=com_csw&view=details&product_id=MULTIOBS_G), last access: 27 September., 2020.

1835 Chevallier, F.: On the parallelization of atmospheric inversions of
1836 CO₂ surface fluxes within a variational
1837 framework, *Geosci. Model Dev.*, 6(3), 783–790, doi:10.5194/gmd-6-783-2013, 2013.

1838 Chevallier, F., Fisher, M., Peylin, P., Serrar, S., Bousquet, P., Bréon, F.-M., Chédin, A. and
1839 Ciais, P.: Inferring CO₂ sources and sinks from satellite observations: Method and
1840 application to TOVS data, *J. Geophys. Res.*, 110(D24), D24309,
1841 doi:10.1029/2005JD006390, 2005.

1842 China, G. A. of C. of the P. R. of: Monthly statistics reports (统计月报),
1843 <http://www.customs.gov.cn/customs/302249/302274/302277/3227050/index.html>.
1844 Last access: 27 September 2020., 2020.

1845 Ciais, P., Sabine, C., Bala, G., Bopp, L., Brovkin, V., Canadell, J., Chhabra, A., DeFries, R.,

1846 Galloway, J., Heimann, M., Jones, C., Le Quéré, C., Myneni, R. B., Piao, S., Thornton, P.,
1847 Willem, J., Friedlingstein, P. and Munhoven, G.: Carbon and Other Biogeochemical
1848 Cycles, in Climate Change 2013: The Physical Science Basis. Contribution of Working
1849 Group I to the Fifth Assessment Report of the Intergovernmental Panel on Climate
1850 Change, edited by Intergovernmental Panel on Climate Change, pp. 465–570,
1851 Cambridge University Press, Cambridge, UK., 2013a.

1852 Ciais, P., Sabine, C., Bala, G., Bopp, L., Brovkin, V., Canadell, J., Chhabra, A., DeFries, R.,
1853 Galloway, J., Heimann, M., Jones, C., Le Quéré, C., Myneni, R. B., Piao, S., Thornton, P.,
1854 Willem, J., Friedlingstein, P. and Munhoven, G.: Carbon and Other Biogeochemical
1855 Cycles, in Climate Change 2013: The Physical Science Basis. Contribution of Working
1856 Group I to the Fifth Assessment Report of the Intergovernmental Panel on Climate
1857 Change, edited by T. F. Stocker, D. Qin, G.-K. Plattner, M. Tignor, S. K. Allen, J.
1858 Boschung, A. Nauels, Y. Xia, V. Bex, and P. M. Midgley, pp. 465–570, Cambridge
1859 University Press, Cambridge. [online] Available from:
1860 [https://www.cambridge.org/core/product/identifier/CBO9781107415324A023/type/
1861 book_part](https://www.cambridge.org/core/product/identifier/CBO9781107415324A023/type/book_part), 2013b.

1862 Ciais, P., Tan, J., Wang, X., Roedenbeck, C., Chevallier, F., Piao, S. L., Moriarty, R., Broquet,
1863 G., Le Quéré, C., Canadell, J. G., Peng, S., Poulter, B., Liu, Z. and Tans, P.: Five decades
1864 of northern land carbon uptake revealed by the interhemispheric CO₂ gradient,
1865 Nature, 568(7751), 221–225, doi:10.1038/s41586-019-1078-6, 2019.

1866 Collier, N., Hoffman, F. M., Lawrence, D. M., Keppel-Aleks, G., Koven, C. D., Riley, W. J., Mu,
1867 M. Q. and Randerson, J. T.: The International Land Model Benchmarking (ILAMB)
1868 System: Design, Theory, and Implementation, J. Adv. Model. Earth Syst., 10(11),
1869 2731–2754, doi:10.1029/2018ms001354, 2018.

1870 Cooper, D. J., Watson, A. J. and Ling, R. D.: Variation of pCO₂ along a North Atlantic
1871 shipping route (U.K. to the Caribbean): A year of automated observations, *Mar.*
1872 *Chem.*, 60(1–2), 147–164, doi:10.1016/S0304-4203(97)00082-0, 1998.

1873 Cox, P. M., Pearson, D., Booth, B. B., Friedlingstein, P., Huntingford, C., Jones, C. D. and
1874 Luke, C. M.: Sensitivity of tropical carbon to climate change constrained by carbon
1875 dioxide variability, *Nature*, 494(7437), 341–344, doi:10.1038/nature11882, 2013.

1876 Dai, A. and Trenberth, K. E.: Estimates of Freshwater Discharge from Continents:
1877 Latitudinal and Seasonal Variations, *J. Hydrometeorol.*, 3(6), 660–687,
1878 doi:10.1175/1525-7541(2002)003<0660:EOFDFC>2.0.CO;2, 2002.

1879 Decharme, B., Delire, C., Minvielle, M., Colin, J., Vergnes, J., Alias, A., Saint-Martin, D.,
1880 Séférian, R., Sénési, S. and Voldoire, A.: Recent Changes in the ISBA-CTRIP Land
1881 Surface System for Use in the CNRM-CM6 Climate Model and in Global Off-Line
1882 Hydrological Applications, *J. Adv. Model. Earth Syst.*, 11(5), 1207–1252,
1883 doi:10.1029/2018MS001545, 2019.

1884 Delire, C., Séférian, R., Decharme, B., Alkama, R., Carrer, D., Joetzjer, E., Morel, X. and
1885 Rocher, M.: The global land carbon cycle simulated with ISBA (in review), *J. Adv.*
1886 *Model. Earth Syst.*, 2019.

1887 Delire, C., Séférian, R., Decharme, B., Alkama, R., Calvet, J., Carrer, D., Gibelin, A., Joetzjer,
1888 E., Morel, X., Rocher, M. and Tzanos, D.: The Global Land Carbon Cycle Simulated
1889 With ISBA-CTRIP: Improvements Over the Last Decade, *J. Adv. Model. Earth Syst.*,
1890 12(9), doi:10.1029/2019MS001886, 2020.

1891 Denman, K. L., Brasseur, G., Chidthaisong, A., Ciais, P., Cox, P. M., Dickinson, R. E.,
1892 Hauglustaine, D., Heinze, C., Holland, E., Jacob, D., Lohmann, U., Ramachandran, S.,
1893 Leite da Silva Dias, P., Wofsy, S. C. and Zhang, X.: Couplings Between Changes in the

1894 Climate System and Biogeochemistry, in *Climate Change 2007: The Physical Science*
1895 *Basis. Contribution of Working Group I to the Fourth Assessment Report of the*
1896 *Intergovernmental Panel on Climate Change*, edited by S. Solomon, Qin D., Manning
1897 M., Marquis M., Averyt K., Tignor M. M. B., H. L. Miller, and Chen Z. L., pp. 499–587,
1898 Cambridge University Press, Cambridge, UK and New York, USA., 2007.

1899 Denning, A. S., Fung, I. Y. and Randall, D.: Latitudinal gradient of atmospheric CO₂ due to
1900 seasonal exchange with land biota, *Nature*, 376(6537), 240–243,
1901 doi:10.1038/376240a0, 1995.

1902 Denvil-Sommer, A., Gehlen, M., Vrac, M. and Mejia, C.: LSCE-FFNN-v1: LSCE-FFNN-v1: a
1903 two-step neural network model for the reconstruction of surface ocean pCO₂ over
1904 the global ocean, *Geosci. Model Dev.*, 12(5), 2091–2105, doi:10.5194/gmd-12-2091-
1905 2019, 2019.

1906 DeVries, T., Holzer, M. and Primeau, F.: Recent increase in oceanic carbon uptake driven by
1907 weaker upper-ocean overturning, *Nature*, 542(7640), 215–218,
1908 doi:10.1038/nature21068, 2017.

1909 DeVries, T., Le Quéré, C., Andrews, O., Berthet, S., Hauck, J., Ilyina, T., Landschützer, P.,
1910 Lenton, A., Lima, I. D., Nowicki, M., Schwinger, J. and Séférian, R.: Decadal trends in
1911 the ocean carbon sink, *Proc. Natl. Acad. Sci.*, 116(24), 11646–11651,
1912 doi:10.1073/pnas.1900371116, 2019.

1913 Dickson, A. G., Sabine, C. L. and Christian, J. .: *Guide to best practices for ocean CO₂*
1914 *measurements. Sidney, British Columbia, North Pacific Marine Science Organization,*
1915 *176pp. (PICES Special Publication, 3)., 2007.*

1916 Dlugokencky, E. and Tans, P.: *Trends in atmospheric carbon dioxide*, National Oceanic &
1917 *Atmospheric Administration, Earth System Research Laboratory (NOAA/ESRL),*

1918 available at: <http://www.esrl.noaa.gov/gmd/ccgg/trends/global.html>, last access: 27
1919 September 2020., 2020.

1920 Doney, S. C., Lima, I., Feely, R. A., Glover, D. M., Lindsay, K., Mahowald, N., Moore, J. K. and
1921 Wanninkhof, R.: Mechanisms governing interannual variability in upper-ocean
1922 inorganic carbon system and air-sea CO₂ fluxes: Physical climate and atmospheric
1923 dust, *Deep. Res. Part II-Topical Stud. Oceanogr.*, 56(8–10), 640–655,
1924 doi:10.1016/j.dsr2.2008.12.006, 2009.

1925 Duce, R. A., LaRoche, J., Altieri, K., Arrigo, K. R., Baker, A. R., Capone, D. G., Cornell, S.,
1926 Dentener, F., Galloway, J., Ganeshram, R. S., Geider, R. J., Jickells, T., Kuypers, M. M.,
1927 Langlois, R., Liss, P. S., Liu, S. M., Middelburg, J. J., Moore, C. M., Nickovic, S., Oschlies,
1928 A., Pedersen, T., Prospero, J., Schlitzer, R., Seitzinger, S., Sorensen, L. L., Uematsu, M.,
1929 Ulloa, O., Voss, M., Ward, B. and Zamora, L.: Impacts of Atmospheric Anthropogenic
1930 Nitrogen on the Open Ocean, *Science* (80-.), 320(5878), 893–897,
1931 doi:10.1126/science.1150369, 2008.

1932 Dufour, C. O., Le Sommer, J., Gehlen, M., Orr, J. C., Molines, J. M., Simeon, J. and Barnier,
1933 B.: Eddy compensation and controls of the enhanced sea-to-air CO₂ flux during
1934 positive phases of the Southern Annular Mode, *Global Biogeochem. Cycles*, 27(3),
1935 950–961, doi:10.1002/gbc.20090, 2013.

1936 Durant, A. J., Le Quéré, C., Hope, C. and Friend, A. D.: Economic value of improved
1937 quantification in global sources and sinks of carbon dioxide, *Philos Trans A Math Phys
1938 Eng Sci*, 369(1943), 1967–1979, doi:10.1098/rsta.2011.0002, 2011.

1939 Eakins, B. W. and Sharman, G. F.: Volumes of the World's Oceans from ETOPO1; NOAA
1940 National Geophysical Data Center, available at:
1941 http://www.ngdc.noaa.gov/mgg/global/etopo1_ocean_volumes.html, last accessed:

1942 27 September 2019., 2010.

1943 EIA: U.S. Energy Information Administration, Short-Term Energy Outlook, available at:

1944 <http://www.eia.gov/forecasts/steo/outlook.cfm>, last access: 27 September 2020.,

1945 2020.

1946 Erb, K., Kastner, T., Plutzer, C., Bais, A. L. S., Carvalhais, N., Fetzel, T., Gingrich, S., Haberl,

1947 H., Lauk, C., Niedertscheider, M., Pongratz, J., Thurner, M. and Luysaert, S.:

1948 Unexpectedly large impact of forest management and grazing on global vegetation

1949 biomass, *Nature*, 553(7686), 73–76, doi:10.1038/nature25138, 2018.

1950 Erb, K. H., Kastner, T., Luysaert, S., Houghton, R. A., Kuemmerle, T., Olofsson, P. and

1951 Haberl, H.: COMMENTARY: Bias in the attribution of forest carbon sinks, *Nat. Clim.*

1952 *Chang.*, 3(10), 854–856, doi:10.1038/nclimate2004, 2013.

1953 Eurostat: Supply and transformation of solid fuels - monthly data (nrg_101m), available at:

1954 <https://ec.europa.eu/eurostat/data/database>, last access: 27 September 2020., 2020.

1955 FAO: Food and Agriculture Organization of the United Nations: Global Forest Resources

1956 Assessment 2015, available at: [http://www.fao.org/forest-resources-](http://www.fao.org/forest-resources-assessment/past-assessments/fra-2015/en/)

1957 [assessment/past-assessments/fra-2015/en/](http://www.fao.org/forest-resources-assessment/past-assessments/fra-2015/en/), last access: 27 September 2019, Rome,

1958 Italy., 2015.

1959 FAOSTAT: Food and Agriculture Organization Statistics Division, available at:

1960 <http://faostat.fao.org/>, last access: 27 September 2020., 2015.

1961 Fay, A. R. and McKinley, G. A.: Global open-ocean biomes: mean and temporal variability,

1962 *Earth Syst. Sci. Data*, 6(2), 273–284, doi:10.5194/essd-6-273-2014, 2014.

1963 Feng, L., Palmer, P. I., Bösch, H. and Dance, S.: Estimating surface

1964 CO₂ fluxes from space-borne

1965 CO₂ dry air mole fraction observations

1966 using an ensemble Kalman Filter, *Atmos. Chem. Phys.*, 9(8), 2619–2633,
1967 doi:10.5194/acp-9-2619-2009, 2009.

1968 Feng, L., Palmer, P. I., Parker, R. J., Deutscher, N. M., Feist, D. G., Kivi, R., Morino, I. and
1969 Sussmann, R.: Estimates of European uptake of CO₂ inferred from GOSAT X CO₂
1970 retrievals : sensitivity to measurement bias inside and outside Europe, , 1289–1302,
1971 doi:10.5194/acp-16-1289-2016, 2016.

1972 Forster, P. M., Forster, H. I., Evans, M. J., Gidden, M. J., Jones, C. D., Keller, C. A., Lamboll,
1973 R. D., Quéré, C. Le, Rogelj, J., Rosen, D., Schleussner, C., Richardson, T. B., Smith, C. J.
1974 and Turnock, S. T.: Current and future global climate impacts resulting from COVID-
1975 19, *Nat. Clim. Chang.*, doi:10.1038/s41558-020-0883-0, 2020.

1976 Francey, R. J., Trudinger, C. M., van der Schoot, M., Law, R. M., Krummel, P. B.,
1977 Langenfelds, R. L., Steele, L. P., Allison, C. E., Stavert, A. R., Andres, R. J. and
1978 Rödenbeck, C.: Reply to “Anthropogenic CO₂ emissions,” *Nat. Clim. Chang.*, 3(7), 604,
1979 doi:10.1038/nclimate1925, 2013.

1980 Friedlingstein, P., Houghton, R. A., Marland, G., Hackler, J., Boden, T. A., Conway, T. J.,
1981 Canadell, J. G., Raupach, M. R., Ciais, P. and Le Quéré, C.: Update on CO₂ emissions,
1982 *Nat. Geosci.*, 3(12), 811–812, doi:10.1038/ngeo1022, 2010.

1983 Friedlingstein, P., Andrew, R. M., Rogelj, J., Peters, G. P., Canadell, J. G., Knutti, R., Luderer,
1984 G., Raupach, M. R., Schaeffer, M., van Vuuren, D. P. and Le Quéré, C.: Persistent
1985 growth of CO₂ emissions and implications for reaching climate targets, *Nat. Geosci.*,
1986 7(10), 709–715, doi:10.1038/Ngeo2248, 2014.

1987 Friedlingstein, P., Jones, M. W., O’Sullivan, M., Andrew, R. M., Hauck, J., Peters, G. P.,
1988 Peters, W., Pongratz, J., Sitch, S., Le Quéré, C., Bakker, D. C. E., Canadell, J. G., Ciais, P.,
1989 Jackson, R. B., Anthoni, P., Barbero, L., Bastos, A., Bastrikov, V., Becker, M., Bopp, L.,

1990 Buitenhuis, E., Chandra, N., Chevallier, F., Chini, L. P., Currie, K. I., Feely, R. A., Gehlen,
1991 M., Gilfillan, D., Gkritzalis, T., Goll, D. S., Gruber, N., Gutekunst, S., Harris, I., Haverd,
1992 V., Houghton, R. A., Hurtt, G., Ilyina, T., Jain, A. K., Joetzjer, E., Kaplan, J. O., Kato, E.,
1993 Klein Goldewijk, K., Korsbakken, J. I., Landschützer, P., Lauvset, S. K., Lefèvre, N.,
1994 Lenton, A., Lienert, S., Lombardozzi, D., Marland, G., McGuire, P. C., Melton, J. R.,
1995 Metzl, N., Munro, D. R., Nabel, J. E. M. S., Nakaoka, S.-I., Neill, C., Omar, A. M., Ono,
1996 T., Peregon, A., Pierrot, D., Poulter, B., Rehder, G., Resplandy, L., Robertson, E.,
1997 Rödenbeck, C., Séférian, R., Schwinger, J., Smith, N., Tans, P. P., Tian, H., Tilbrook, B.,
1998 Tubiello, F. N., van der Werf, G. R., Wiltshire, A. J. and Zaehle, S.: Global Carbon
1999 Budget 2019, *Earth Syst. Sci. Data*, 11(4), 1783–1838, doi:10.5194/essd-11-1783-
2000 2019, 2019.

2001 Gasser, T. and Ciais, P.: A theoretical framework for the net land-to-atmosphere
2002 CO₂ flux and its implications in the
2003 definition of “emissions from land-use change”, *Earth Syst.*
2004 *Dyn.*, 4(1), 171–186, doi:10.5194/esd-4-171-2013, 2013.

2005 Gasser, T., Ciais, P., Boucher, O., Quilcaille, Y., Tortora, M., Bopp, L. and Hauglustaine, D.:
2006 The compact Earth system model OSCAR v2.2: description and first results, *Geosci.*
2007 *Model Dev.*, 10(1), 271–319, doi:10.5194/gmd-10-271-2017, 2017.

2008 Gasser, T., Crepin, L., Quilcaille, Y., Houghton, R. A., Ciais, P. and Obersteiner, M.: Historical
2009 CO₂ emissions from land use and land cover change and their uncertainty, , 4075–
2010 4101, 2020.

2011 Gaubert, B., Stephens, B. B., Basu, S., Chevallier, F., Deng, F., Kort, E. A., Patra, P. K., Peters,
2012 W., Rödenbeck, C., Saeki, T., Schimel, D., Van der Laan-Luijkx, I., Wofsy, S. and Yin, Y.:
2013 Global atmospheric CO₂ inverse models

2014 converging on neutral tropical land exchange, but disagreeing on fossil fuel and
2015 atmospheric growth rate, *Biogeosciences*, 16(1), 117–134, doi:10.5194/bg-16-117-
2016 2019, 2019.

2017 GCP: The Global Carbon Budget 2007, available at:
2018 <http://www.globalcarbonproject.org/carbonbudget/archive.htm>, last access: 7
2019 November 2016., 2007.

2020 Giglio, L., Schroeder, W. and Justice, C. O.: The collection 6 MODIS active fire detection
2021 algorithm and fire products, *Remote Sens. Environ.*, 178, 31–41,
2022 doi:10.1016/j.rse.2016.02.054, 2016.

2023 Gilfillan, D., Marland, G., Boden, T. and Andres, R.: Global, Regional, and National Fossil-
2024 Fuel CO₂ Emissions, available at: <https://energy.appstate.edu/CDIAC>, last access: 27
2025 September 2020, 2020.

2026 Goddijn-Murphy, L. M., Woolf, D. K., Land, P. E., Shutler, J. D. and Donlon, C.: The
2027 OceanFlux Greenhouse Gases methodology for deriving a sea surface climatology of
2028 CO₂ fugacity in support of air–sea gas
2029 flux studies, *Ocean Sci.*, 11(4), 519–541, doi:10.5194/os-11-519-2015, 2015.

2030 Goldewijk, K. K., Beusen, A., Doelman, J. and Stehfest, E.: Anthropogenic land use
2031 estimates for the Holocene - HYDE 3.2, *Earth Syst. Sci. Data*, 9(2), 927–953,
2032 doi:10.5194/essd-9-927-2017, 2017a.

2033 Goldewijk, K. K., Dekker, S. C. and van Zanden, J. L.: Per-capita estimations of long-term
2034 historical land use and the consequences for global change research, *J. Land Use Sci.*,
2035 12(5), 313–337, doi:10.1080/1747423x.2017.1354938, 2017b.

2036 Goll, D. S., Vuichard, N., Maignan, F., Jornet-Puig, A., Sardans, J., Violette, A., Peng, S. S.,
2037 Sun, Y., Kvakic, M., Guimberteau, M., Guenet, B., Zaehle, S., Penuelas, J., Janssens, I.

2038 and Ciais, P.: A representation of the phosphorus cycle for ORCHIDEE (revision 4520),
2039 Geosci. Model Dev., 10(10), 3745–3770, doi:10.5194/gmd-10-3745-2017, 2017.

2040 Gregg, J. S., Andres, R. J. and Marland, G.: China: Emissions pattern of the world leader in
2041 CO₂ emissions from fossil fuel consumption and cement production, Geophys. Res.
2042 Lett., 35(8), L08806, doi:Artn L0880610.1029/2007gl032887, 2008.

2043 Gregor, L., Lebehot, A. D., Kok, S. and Scheel Monteiro, P. M.: A comparative assessment of
2044 the uncertainties of global surface ocean CO₂ estimates using a machine-learning
2045 ensemble (CSIR-ML6 version 2019a)-Have we hit the wall?, Geosci. Model Dev.,
2046 12(12), 5113–5136, doi:10.5194/gmd-12-5113-2019, 2019.

2047 Gruber, N., Clement, D., Carter, B. R., Feely, R. A., van Heuven, S., Hoppema, M., Ishii, M.,
2048 Key, R. M., Kozyr, A., Lauvset, S. K., Lo Monaco, C., Mathis, J. T., Murata, A., Olsen, A.,
2049 Perez, F. F., Sabine, C. L., Tanhua, T. and Wanninkhof, R.: The oceanic sink for
2050 anthropogenic CO₂ from 1994 to 2007, Science (80-.), 363(6432), 1193–1199,
2051 doi:10.1126/science.aau5153, 2019.

2052 Hansen, M. C., Potapov, P. V., Moore, R., Hancher, M., Turubanova, S. A., Tyukavina, A.,
2053 Thau, D., Stehman, S. V., Goetz, S. J., Loveland, T. R., Kommareddy, A., Egorov, A.,
2054 Chini, L., Justice, C. O. and Townshend, J. R. G.: High-Resolution Global Maps of 21st-
2055 Century Forest Cover Change, Science (80-.), 342(6160), 850–853,
2056 doi:10.1126/science.1244693, 2013.

2057 Hansen, M. C., Krylov, A., Tyukavina, A., Potapov, P. V., Turubanova, S., Zutta, B., Ifo, S.,
2058 Margono, B., Stolle, F. and Moore, R.: Humid tropical forest disturbance alerts using
2059 Landsat data, Environ. Res. Lett., 11(3), doi:10.1088/1748-9326/11/3/034008, 2016.

2060 Hansis, E., Davis, S. J. and Pongratz, J.: Relevance of methodological choices for accounting
2061 of land use change carbon fluxes, Global Biogeochem. Cycles, 29(8), 1230–1246,

2062 doi:10.1002/2014GB004997, 2015.

2063 Harris, I., Jones, P. D., Osborn, T. J. and Lister, D. H.: Updated high-resolution grids of
2064 monthly climatic observations - the CRU TS3.10 Dataset, *Int. J. Climatol.*, 34(3), 623–
2065 642, doi:10.1002/joc.3711, 2014.

2066 Hertwich, E. G. and Peters, G. P.: Carbon footprint of nations: a global, trade-linked
2067 analysis, *Env. Sci Technol*, 43(16), 6414–6420, doi:10.1021/es803496a, 2009.

2068 Hooijer, A., Page, S., Canadell, J. G., Silvius, M., Kwadijk, J., Wosten, H. and Jauhiainen, J.:
2069 Current and future CO2 emissions from drained peatlands in Southeast Asia,
2070 *Biogeosciences*, 7(5), 1505–1514, doi:10.5194/bg-7-1505-2010, 2010.

2071 Houghton, R. A.: Revised estimates of the annual net flux of carbon to the atmosphere
2072 from changes in land use and land management 1850-2000, *Tellus Ser. B-Chemical*
2073 *Phys. Meteorol.*, 55(2), 378–390, doi:DOI 10.1034/j.1600-0889.2003.01450.x, 2003.

2074 Houghton, R. A. and Nassikas, A. A.: Global and regional fluxes of carbon from land use and
2075 land cover change 1850–2015, *Global Biogeochem. Cycles*, 31(3), 456–472,
2076 doi:10.1002/2016GB005546, 2017.

2077 Houghton, R. A., House, J. I., Pongratz, J., Van Der Werf, G. R., Defries, R. S., Hansen, M. C.,
2078 Le Quéré, C. and Ramankutty, N.: Carbon emissions from land use and land-cover
2079 change, *Biogeosciences*, 9(12), 5125–5142, doi:10.5194/bg-9-5125-2012, 2012.

2080 Houweling, S., Baker, D., Basu, S., Boesch, H., Butz, A., Chevallier, F., Deng, F., Dlugokencky,
2081 E. J., Feng, L., Ganshin, A., Hasekamp, O., Jones, D., Maksyutov, S., Marshall, J., Oda,
2082 T., O’Dell, C. W., Oshchepkov, S., Palmer, P. I., Peylin, P., Poussi, Z., Reum, F., Takagi,
2083 H., Yoshida, Y. and Zhuravlev, R.: An intercomparison of inverse models for estimating
2084 sources and sinks of CO2 using GOSAT measurements, *J. Geophys. Res.*, 120(10),
2085 5253–5266, doi:10.1002/2014jd022962, 2015.

2086 Hugelius, G., Bockheim, J. G., Camill, P., Elberling, B., Grosse, G., Harden, J. W., Johnson, K.,
2087 Jorgenson, T., Koven, C. D., Kuhry, P., Michaelson, G., Mishra, U., Palmtag, J., Ping, C.
2088 L., O'Donnell, J., Schirrmeister, L., Schuur, E. A. G., Sheng, Y., Smith, L. C., Strauss, J.
2089 and Yu, Z.: A new data set for estimating organic carbon storage to 3m depth in soils
2090 of the northern circumpolar permafrost region, *Earth Syst. Sci. Data*, 5(2), 393–402,
2091 doi:10.5194/essd-5-393-2013, 2013.

2092 Huntzinger, D. N., Michalak, A. M., Schwalm, C., Ciais, P., King, A. W., Fang, Y., Schaefer, K.,
2093 Wei, Y., Cook, R. B., Fisher, J. B., Hayes, D., Huang, M., Ito, A., Jain, A. K., Lei, H., Lu, C.,
2094 Maignan, F., Mao, J., Parazoo, N., Peng, S., Poulter, B., Ricciuto, D., Shi, X., Tian, H.,
2095 Wang, W., Zeng, N. and Zhao, F.: Uncertainty in the response of terrestrial carbon sink
2096 to environmental drivers undermines carbon-climate feedback predictions, *Sci. Rep.*,
2097 7(1), 4765, doi:10.1038/s41598-017-03818-2, 2017.

2098 Hurtt, G. C., Chini, L. P., Frohking, S., Betts, R. A., Feddema, J., Fischer, G., Fisk, J. P.,
2099 Hibbard, K., Houghton, R. A., Janetos, A., Jones, C. D., Kindermann, G., Kinoshita, T.,
2100 Goldewijk, K. K., Riahi, K., Shevliakova, E., Smith, S., Stehfest, E., Thomson, A.,
2101 Thornton, P., van Vuuren, D. P. and Wang, Y. P.: Harmonization of land-use scenarios
2102 for the period 1500-2100: 600 years of global gridded annual land-use transitions,
2103 wood harvest, and resulting secondary lands, *Clim. Change*, 109(1–2), 117–161,
2104 doi:10.1007/s10584-011-0153-2, 2011.

2105 Hurtt, G. C., Chini, L., Sahajpal, R., Frohking, S., Bodirsky, B. L., Hasegawa, T., Havlik, P.,
2106 Heinemann, A. and Humpenöder, F.: Harmonization of Global Land-Use Change and
2107 Management for the Period 850-2100 (LUH2) for CMIP6, , (April), 1–65, 2020.

2108 IEA/OECD: International Energy Agency/Organisation for Economic Cooperation and
2109 Development: CO2 emissions from fuel combustion, available at:

2110 <https://webstore.iea.org/co2-emissions-from-fuel-combustion-2019-highlights>, last
2111 access 27 September 2020, Paris., 2019.

2112 IEA: World Energy Statistics (2019 Edition), available at: www.iea.org, last access 27
2113 September 2019, 2019.

2114 IEA: Global Energy Review 2020, available at: [https://www.iea.org/reports/global-energy-](https://www.iea.org/reports/global-energy-review-2020)
2115 [review-2020](https://www.iea.org/reports/global-energy-review-2020), last accessed: 27 September 2020, Paris., 2020.

2116 Ilyina, T., Six, K. D., Segschneider, J., Maier-Reimer, E., Li, H. and Núñez-Riboni, I.: Global
2117 ocean biogeochemistry model HAMOCC: Model architecture and performance as
2118 component of the MPI-Earth system model in different CMIP5 experimental
2119 realizations, *J. Adv. Model. Earth Syst.*, 5(2), 287–315, doi:10.1029/2012MS000178,
2120 2013.

2121 IMF: World Economic Outlook, Available at: www.imf.org. Last accessed 27 September
2122 2020., 2020.

2123 Jackson, R. B., Canadell, J. G., Le Quéré, C., Andrew, R. M., Korsbakken, J. I., Peters, G. P.
2124 and Nakicenovic, N.: Reaching peak emissions, *Nat. Clim. Chang.*, 6(1), 7–10,
2125 doi:10.1038/nclimate2892, 2016.

2126 Jackson, R. B., Le Quéré, C., Andrew, R. M., Canadell, J. G., Korsbakken, J. I., Liu, Z., Peters,
2127 G. P. and Zheng, B.: Global energy growth is outpacing decarbonization, *Environ. Res.*
2128 *Lett.*, 13(12), 120401, doi:10.1088/1748-9326/aaf303, 2018.

2129 Jackson, R. B., Friedlingstein, P., Andrew, R. M., Canadell, J. G., Le Quéré, C. and Peters, G.
2130 P.: Persistent fossil fuel growth threatens the Paris Agreement and planetary health,
2131 *Environ. Res. Lett.*, 14(12), 121001, doi:10.1088/1748-9326/ab57b3, 2019.

2132 Jacobson, A. R., Mikaloff Fletcher, S. E., Gruber, N., Sarmiento, J. L. and Gloor, M.: A joint
2133 atmosphere-ocean inversion for surface fluxes of carbon dioxide: 2. Regional results,

2134 Global Biogeochem. Cycles, 21(1), GB1020, doi:10.1029/2006GB002703, 2007.

2135 Janssens-Maenhout, G., Crippa, M., Guizzardi, D., Muntean, M., Schaaf, E., Dentener, F.,
2136 Bergamaschi, P., Pagliari, V., Olivier, J. G. J., Peters, J. A. H. W., van Aardenne, J. A.,
2137 Monni, S., Doering, U., Petrescu, A. M. R., Solazzo, E. and Oreggioni, G. D.: EDGAR
2138 v4.3.2 Global Atlas of the three major greenhouse gas emissions for the period 1970–
2139 2012, Earth Syst. Sci. Data, 11(3), 959–1002, doi:10.5194/essd-11-959-2019, 2019.

2140 JODI: Joint Organisations Data Initiative, available at: <https://www.jodidata.org>, last
2141 access: 327 September 2020., 2020.

2142 Jones, M. W., Andrew, R. M., Peters, G. P., Janssens-Maenhout, G., De-Gol, A. J., Ciais, P.,
2143 Patra, P. K., Chevallier, F. and Le Quéré, C.: Gridded fossil CO₂ emissions and related
2144 O₂ combustion consistent with national inventories 1959-2018 (in revision), Sci. Data,
2145 2020.

2146 Joos, F. and Spahni, R.: Rates of change in natural and anthropogenic radiative forcing over
2147 the past 20,000 years, Proc. Natl. Acad. Sci., 105(5), 1425–1430,
2148 doi:10.1073/pnas.0707386105, 2008.

2149 Jung, M., Reichstein, M., Ciais, P., Seneviratne, S. I., Sheffield, J., Goulden, M. L., Bonan, G.,
2150 Cescatti, A., Chen, J., de Jeu, R., Dolman, A. J., Eugster, W., Gerten, D., Gianelle, D.,
2151 Gobron, N., Heinke, J., Kimball, J., Law, B. E., Montagnani, L., Mu, Q., Mueller, B.,
2152 Oleson, K., Papale, D., Richardson, A. D., Roupsard, O., Running, S., Tomelleri, E.,
2153 Viovy, N., Weber, U., Williams, C., Wood, E., Zaehle, S. and Zhang, K.: Recent decline
2154 in the global land evapotranspiration trend due to limited moisture supply, Nature,
2155 467(7318), 951–954, doi:10.1038/nature09396, 2010.

2156 Kalnay, E., Kanamitsu, M., Kistler, R., Collins, W., Deaven, D., Gandin, L., Iredell, M., Saha,
2157 S., White, G., Woollen, J., Zhu, Y., Leetmaa, A., Reynolds, R., Chelliah, M., Ebisuzaki,

2158 W., Higgins, W., Janowiak, J., Mo, K. C., Ropelewski, C., Wang, J., Jenne, R. and Joseph,
2159 D.: The NCEP/NCAR 40-Year Reanalysis Project, *Bull. Am. Meteorol. Soc.*, 77(3), 437–
2160 471, doi:10.1175/1520-0477(1996)077<0437:TNYRP>2.0.CO;2, 1996.

2161 Kato, E., Kinoshita, T., Ito, A., Kawamiya, M. and Yamagata, Y.: Evaluation of spatially
2162 explicit emission scenario of land-use change and biomass burning using a process-
2163 based biogeochemical model, *J. Land Use Sci.*, 8(1), 104–122,
2164 doi:10.1080/1747423x.2011.628705, 2013.

2165 De Kauwe, M. G., Disney, M. I., Quaife, T., Lewis, P. and Williams, M.: An assessment of the
2166 MODIS collection 5 leaf area index product for a region of mixed coniferous forest,
2167 *Remote Sens. Environ.*, 115(2), 767–780, doi:10.1016/j.rse.2010.11.004, 2011.

2168 Keeling, C. D., Bacastow, R. B., Bainbridge, A. E., Ekdahl, C. A., Guenther, P. R., Waterman,
2169 L. S. and Chin, J. F. S.: Atmospheric Carbon-Dioxide Variations at Mauna-Loa
2170 Observatory, Hawaii, *Tellus*, 28(6), 538–551, doi:10.1111/j.2153-
2171 3490.1976.tb00701.x, 1976.

2172 Keeling, R. F. and Manning, A. C.: Studies of Recent Changes in Atmospheric O₂ Content, in
2173 *Treatise on Geochemistry*, vol. 5, edited by H. D. Holland and K. K. Turekian, pp. 385–
2174 404, Elsevier, Oxford., 2014.

2175 Khatiwala, S., Primeau, F. and Hall, T.: Reconstruction of the history of anthropogenic CO₂
2176 concentrations in the ocean, *Nature*, 462(7271), 346-U110, doi:10.1038/nature08526,
2177 2009.

2178 Khatiwala, S., Tanhua, T., Fletcher, S. M., Gerber, M., Doney, S. C., Graven, H. D., Gruber,
2179 N., McKinley, G. A., Murata, A., Rios, A. F. and Sabine, C. L.: Global ocean storage of
2180 anthropogenic carbon, *Biogeosciences*, 10(4), 2169–2191, doi:10.5194/bg-10-2169-
2181 2013, 2013.

2182 Kobayashi, S., Ota, Y., Harada, Y., Ebita, A., Moriya, M., Onoda, H., Onogi, K., Kamahori, H.,
2183 Kobayashi, C., Endo, H., Miyaoka, K. and Takahashi, K.: The JRA-55 Reanalysis: General
2184 Specifications and Basic Characteristics, *J. Meteorol. Soc. Japan*, 93(1), 5–48,
2185 doi:10.2151/jmsj.2015-001, 2015.

2186 Korsbakken, J. I., Peters, G. P. and Andrew, R. M.: Uncertainties around reductions in
2187 China’s coal use and CO₂ emissions, *Nat. Clim. Chang.*, 6(7), 687–690,
2188 doi:10.1038/nclimate2963, 2016.

2189 Krinner, G., Viovy, N., de Noblet-Ducoudre, N., Ogee, J., Polcher, J., Friedlingstein, P., Ciais,
2190 P., Sitch, S. and Prentice, I. C.: A dynamic global vegetation model for studies of the
2191 coupled atmosphere-biosphere system, *Global Biogeochem. Cycles*, 19(1), 1–33,
2192 doi:Artn Gb101510.1029/2003gb002199, 2005.

2193 Van Der Laan-Luijkx, I. T., Van Der Velde, I. R., Van Der Veen, E., Tsuruta, A., Stanislawski,
2194 K., Babenhauserheide, A., Fang Zhang, H., Liu, Y., He, W., Chen, H., Masarie, K. A.,
2195 Krol, M. C. and Peters, W.: The CarbonTracker Data Assimilation Shell (CTDAS) v1.0:
2196 Implementation and global carbon balance 2001-2015, *Geosci. Model Dev.*, 10(7),
2197 2785–2800, doi:10.5194/gmd-10-2785-2017, 2017.

2198 Lacroix, F., Ilyina, T. and Hartmann, J.: Oceanic CO₂ outgassing and biological production
2199 hotspots induced by pre-industrial river loads of nutrients and carbon in a global
2200 modeling approach, , 55–88, 2020.

2201 Landschützer, P., Gruber, N., Bakker, D. C. E., Schuster, U., Nakaoka, S., Payne, M. R., Sasse,
2202 T. P. and Zeng, J.: A neural network-based estimate of the seasonal to inter-annual
2203 variability of the Atlantic Ocean carbon sink, , 2, 7793–7815, doi:10.5194/bg-10-7793-
2204 2013, 2013.

2205 Landschützer, P., Gruber, N., Bakker, D. C. E. and Schuster, U.: Recent variability of the

2206 global ocean carbon sink, *Global Biogeochem. Cycles*, 28(9), 927–949,
2207 doi:10.1002/2014gb004853, 2014.

2208 Landschützer, P., Gruber, N., Haumann, F. A., Rödenbeck, C., Bakker, D. C. E., van Heuven,
2209 S., Hoppema, M., Metzl, N., Sweeney, C., Takahashi, T., Tilbrook, B. and Wanninkhof,
2210 R.: The reinvigoration of the Southern Ocean carbon sink, *Science* (80-.), 349(6253),
2211 1221–1224, doi:10.1126/science.aab2620, 2015.

2212 Landschützer, P., Gruber, N. and Bakker, D. C. E.: Decadal variations and trends of the
2213 global ocean carbon sink, *Global Biogeochem. Cycles*, 30(10), 1396–1417,
2214 doi:10.1002/2015gb005359, 2016.

2215 Lasslop, G., Reichstein, M., Papale, D., Richardson, A. D., Arneeth, A., Barr, A., Stoy, P. and
2216 Wohlfahrt, G.: Separation of net ecosystem exchange into assimilation and
2217 respiration using a light response curve approach: critical issues and global
2218 evaluation, *Glob. Chang. Biol.*, 16(1), 187–208, doi:10.1111/j.1365-
2219 2486.2009.02041.x, 2010.

2220 Law, R. M., Ziehn, T., Matear, R. J., Lenton, A., Chamberlain, M. A., Stevens, L. E., Wang, Y.-
2221 P., Srbinovsky, J., Bi, D., Yan, H. and Vohralik, P. F.: The carbon cycle in the Australian
2222 Community Climate and Earth System Simulator (ACCESS-ESM1) – Part 1: Model
2223 description and pre-industrial simulation, *Geosci. Model Dev.*, 10(7), 2567–2590,
2224 doi:10.5194/gmd-10-2567-2017, 2017.

2225 Lawrence, D. M., Fisher, R. A., Koven, C. D., Oleson, K. W., Swenson, S. C., Bonan, G.,
2226 Collier, N., Ghimire, B., Kampenhout, L., Kennedy, D., Kluzek, E., Lawrence, P. J., Li, F.,
2227 Li, H., Lombardozzi, D., Riley, W. J., Sacks, W. J., Shi, M., Vertenstein, M., Wieder, W.
2228 R., Xu, C., Ali, A. A., Badger, A. M., Bisht, G., Broeke, M., Brunke, M. A., Burns, S. P.,
2229 Buzan, J., Clark, M., Craig, A., Dahlin, K., Drewniak, B., Fisher, J. B., Flanner, M., Fox, A.

2230 M., Gentine, P., Hoffman, F., Keppel-Aleks, G., Knox, R., Kumar, S., Lenaerts, J., Leung,
2231 L. R., Lipscomb, W. H., Lu, Y., Pandey, A., Pelletier, J. D., Perket, J., Randerson, J. T.,
2232 Ricciuto, D. M., Sanderson, B. M., Slater, A., Subin, Z. M., Tang, J., Thomas, R. Q., Val
2233 Martin, M. and Zeng, X.: The Community Land Model version 5: Description of new
2234 features, benchmarking, and impact of forcing uncertainty (accepted), *J. Adv. Model.*
2235 *Earth Syst.*, 2018MS001583, doi:10.1029/2018MS001583, 2019.

2236 Li, H. and Ilyina, T.: Current and Future Decadal Trends in the Oceanic Carbon Uptake Are
2237 Dominated by Internal Variability, *Geophys. Res. Lett.*, 45(2), 916–925,
2238 doi:10.1002/2017gl075370, 2018.

2239 Li, W., Ciais, P., Peng, S., Yue, C., Wang, Y., Thurner, M., Saatchi, S. S., Arneeth, A., Avitabile,
2240 V., Carvalhais, N., Harper, A. B., Kato, E., Koven, C., Liu, Y. Y., Nabel, J. E. M. S., Pan, Y.,
2241 Pongratz, J., Poulter, B., Pugh, T. A. M., Santoro, M., Sitch, S., Stocker, B. D., Viovy, N.,
2242 Wiltshire, A., Yousefpour, R. and Zaehle, S.: Land-use and land-cover change carbon
2243 emissions between 1901 and 2012 constrained by biomass observations,
2244 *Biogeosciences*, 14(22), doi:10.5194/bg-14-5053-2017, 2017.

2245 Liao, E., Resplandy, L., Liu, J. and Bowman, K. W.: Amplification of the Ocean Carbon Sink
2246 During El Niños: Role of Poleward Ekman Transport and Influence on Atmospheric CO
2247 2, *Global Biogeochem. Cycles*, 34(9), doi:10.1029/2020GB006574, 2020.

2248 Lienert, S. and Joos, F.: A Bayesian ensemble data assimilation to constrain model
2249 parameters and land-use carbon emissions, *Biogeosciences*, 15(9), 2909–2930,
2250 doi:10.5194/bg-15-2909-2018, 2018.

2251 Liu, Z., Guan, D., Wei, W., Davis, S. J., Ciais, P., Bai, J., Peng, S., Zhang, Q., Hubacek, K.,
2252 Marland, G., Andres, R. J., Crawford-Brown, D., Lin, J., Zhao, H., Hong, C., Boden, T. A.,
2253 Feng, K., Peters, G. P., Xi, F., Liu, J., Li, Y., Zhao, Y., Zeng, N. and He, K.: Reduced

2254 carbon emission estimates from fossil fuel combustion and cement production in
2255 China, *Nature*, 524(7565), 335–338, doi:10.1038/nature14677, 2015.

2256 Liu, Z., Ciais, P., Deng, Z., Lei, R., Davis, S. J., Feng, S., Zheng, B., Cui, D., Dou, X., He, P., Zhu,
2257 B., Lu, C., Ke, P., Sun, T., Wang, Y., Yue, X., Wang, Y., Lei, Y., Zhou, H., Cai, Z., Wu, Y.,
2258 Guo, R., Han, T., Xue, J., Boucher, O., Boucher, E., Chevallier, F., Wei, Y., Zhong, H.,
2259 Kang, C., Zhang, N., Chen, B., Xi, F., Marie, F., Zhang, Q., Guan, D., Gong, P., Kammen,
2260 D. M., He, K. and Schellnhuber, H. J.: COVID-19 causes record decline in global CO₂
2261 emissions, [online] Available from: <http://arxiv.org/abs/2004.13614>, 2020.

2262 Ma, L., Hurtt, G. C., Chini, L. P., Sahajpal, R., Pongratz, J., Frohking, S., Stehfest, E.,
2263 Goldewijk, K. K., Leary, D. O. and Doelman, J. C.: Global rules for translating land-use
2264 change (LUH2) to land-cover change for CMIP6 using GLM2, , 3203–3220, 2020.

2265 Manning, A. C. and Keeling, R. F.: Global oceanic and land biotic carbon sinks from the
2266 Scripps atmospheric oxygen flask sampling network, *Tellus Ser. B-Chemical Phys.*
2267 *Meteorol.*, 58(2), 95–116, doi:DOI 10.1111/j.1600-0889.2006.00175.x, 2006.

2268 Marland, G.: Uncertainties in Accounting for CO₂ From Fossil Fuels, *J. Ind. Ecol.*, 12(2),
2269 136–139, doi:10.1111/j.1530-9290.2008.00014.x, 2008.

2270 Marland, G. and Rotty, R. M.: Carbon-Dioxide Emissions from Fossil-Fuels - a Procedure for
2271 Estimation and Results for 1950-1982, *Tellus Ser. B-Chemical Phys. Meteorol.*, 36(4),
2272 232–261, doi:DOI 10.1111/j.1600-0889.1984.tb00245.x, 1984.

2273 Marland, G., Hamal, K. and Jonas, M.: How Uncertain Are Estimates of CO₂ Emissions?, *J.*
2274 *Ind. Ecol.*, 13(1), 4–7, doi:10.1111/j.1530-9290.2009.00108.x, 2009.

2275 Masarie, K. A. and Tans, P. P.: Extension and Integration of Atmospheric Carbon-Dioxide
2276 Data into a Globally Consistent Measurement Record, *J. Geophys. Res.*, 100(D6),
2277 11593–11610, doi:Doi 10.1029/95jd00859, 1995.

2278 Mauritsen, T., Bader, J., Becker, T., Behrens, J., Bittner, M., Brokopf, R., Brovkin, V.,
 2279 Claussen, M., Crueger, T., Esch, M., Fast, I., Fiedler, S., Fläschner, D., Gayler, V.,
 2280 Giorgetta, M., Goll, D. S., Haak, H., Hagemann, S., Hedemann, C., Hohenegger, C.,
 2281 Ilyina, T., Jahns, T., Jimenéz-de-la-Cuesta, D., Jungclaus, J., Kleinen, T., Kloster, S.,
 2282 Kracher, D., Kinne, S., Kleberg, D., Lasslop, G., Kornblueh, L., Marotzke, J., Matei, D.,
 2283 Meraner, K., Mikolajewicz, U., Modali, K., Möbis, B., Müller, W. A., Nabel, J. E. M. S.,
 2284 Nam, C. C. W., Notz, D., Nyawira, S., Paulsen, H., Peters, K., Pincus, R., Pohlmann, H.,
 2285 Pongratz, J., Popp, M., Raddatz, T. J., Rast, S., Redler, R., Reick, C. H., Rohrschneider,
 2286 T., Schemann, V., Schmidt, H., Schnur, R., Schulzweida, U., Six, K. D., Stein, L.,
 2287 Stemmler, I., Stevens, B., Storch, J., Tian, F., Voigt, A., Vrese, P., Wieners, K.,
 2288 Wilkenskjaeld, S., Winkler, A. and Roeckner, E.: Developments in the MPI-M Earth
 2289 System Model version 1.2 (MPI-ESM1.2) and Its Response to Increasing CO₂, *J. Adv.*
 2290 *Model. Earth Syst.*, 11(4), 998–1038, doi:10.1029/2018MS001400, 2019.

2291 McKinley, G. A., Pilcher, D. J., Fay, A. R., Lindsay, K., Long, M. C. and Lovenduski, N. S.:
 2292 Timescales for detection of trends in the ocean carbon sink, *Nature*, 530(7591), 469–
 2293 472, doi:10.1038/nature16958, 2016.

2294 McKinley, G. A., Fay, A. R., Eddebbar, Y. A., Gloege, L. and Lovenduski, N. S.: External
 2295 Forcing Explains Recent Decadal Variability of the Ocean Carbon Sink, *AGU Adv.*, 1(2),
 2296 1–10, doi:10.1029/2019av000149, 2020.

2297 McNeil, B. I., Matear, R. J., Key, R. M., Bullister, J. L. and Sarmiento, J. L.: Anthropogenic
 2298 CO₂ uptake by the ocean based on the global chlorofluorocarbon data set, *Science*
 2299 (80-.), 299(5604), 235–239, doi:10.1126/science.1077429, 2003.

2300 Meiyappan, P., Jain, A. K. and House, J. I.: Increased influence of nitrogen limitation on CO₂
 2301 emissions from future land use and land use change, *Global Biogeochem. Cycles*,

2302 29(9), 1524–1548, doi:10.1002/2015gb005086, 2015.

2303 Melton, J. R., Arora, V. K., Wisernig-cojoc, E., Seiler, C., Fortier, M. and Chan, E.: CLASSIC v1
2304 . 0 : the open-source community successor to the Canadian Land Surface Scheme (
2305 CLASS) and the Canadian Terrestrial Ecosystem Model (CTEM) – Part 1 : Model
2306 framework and site-level performance, , 2825–2850, 2020.

2307 Mercado, L. M., Bellouin, N., Sitch, S., Boucher, O., Huntingford, C., Wild, M. and Cox, P.
2308 M.: Impact of changes in diffuse radiation on the global land carbon sink, *Nature*,
2309 458(7241), 1014–1017, doi:10.1038/nature07949, 2009.

2310 Mikaloff Fletcher, S. E., Gruber, N., Jacobson, A. R., Doney, S. C., Dutkiewicz, S., Gerber, M.,
2311 Follows, M., Joos, F., Lindsay, K., Menemenlis, D., Mouchet, A., Müller, S. A. and
2312 Sarmiento, J. L.: Inverse estimates of anthropogenic CO₂ uptake, transport, and
2313 storage by the ocean, *Global Biogeochem. Cycles*, 20(2), GB2002,
2314 doi:10.1029/2005GB002530, 2006.

2315 Millar, R. J., Fuglestedt, J. S., Friedlingstein, P., Rogelj, J., Grubb, M. J., Matthews, H. D.,
2316 Skeie, R. B., Forster, P. M., Frame, D. J. and Allen, M. R.: Emission budgets and
2317 pathways consistent with limiting warming to 1.5 °C, *Nat. Geosci.*, 10(10), 741–747,
2318 doi:10.1038/ngeo3031, 2017.

2319 Van Minnen, J. G., Klein Goldewijk, K., Stehfest, E., Eickhout, B., van Drecht, G. and
2320 Leemans, R.: The importance of three centuries of land-use change for the global and
2321 regional terrestrial carbon cycle, *Clim. Change*, 97(1–2), 123–144,
2322 doi:10.1007/s10584-009-9596-0, 2009.

2323 Myhre, G., Alterskjær, K. and Lowe, D.: A fast method for updating global fossil fuel carbon
2324 dioxide emissions, *Environ. Res. Lett.*, 4(3), 034012, doi:10.1088/1748-
2325 9326/4/3/034012, 2009.

2326 Myneni, R. B., Ramakrishna, R., Nemani, R. and Running, S. W.: Estimation of global leaf
2327 area index and absorbed par using radiative transfer models, IEEE Trans. Geosci.
2328 Remote Sens., 35(6), 1380–1393, doi:10.1109/36.649788, 1997.

2329 Naegler, T. and Levin, I.: Biosphere-atmosphere gross carbon exchange flux and the δ^{13}
2330 CO₂ and Δ^{14} CO₂ disequilibria constrained by the biospheric excess radiocarbon
2331 inventory, J. Geophys. Res., 114(D17), D17303, doi:10.1029/2008JD011116, 2009.

2332 Narayanan, B., Aguiar, A. and McDougall, R.: Global Trade, Assistance, and Production: The
2333 GTAP 9 Data Base, Cent. Glob. Trade Anal. Purdue Univ., 2015(September) [online]
2334 Available from: <https://www.gtap.agecon.purdue.edu/databases/v9/default.asp>,
2335 2015.

2336 NBS: National Bureau of Statistics, 2019. Statistical Communiqué of the People’s Republic
2337 of China on the 2018 National Economic and Social Development, available at:
2338 http://www.stats.gov.cn/english/PressRelease/201902/t20190228_1651335.html.
2339 Last access: 23 S., 2019.

2340 NBS: National Bureau of Statistics (NBS): National Data (online database). availalble at:
2341 <http://data.stats.gov.cn/>, Last access: 27 September 2020, National Bureau of
2342 Statistics., 2020a.

2343 NBS: Statistical Communiqué of the People’s Republic of China on the 2019 National
2344 Economic and Social Development, available at:
2345 http://www.stats.gov.cn/english/PressRelease/202002/t20200228_1728917.html.,
2346 2020b.

2347 Nightingale, P. D., Malin, G., Law, C. S., Watson, A. J., Liss, P. S., Liddicoat, M. I., Boutin, J.
2348 and Upstill-Goddard, R. C.: In situ evaluation of air-sea gas exchange
2349 parameterizations using novel conservative and volatile tracers, Global Biogeochem.

2350 Cycles, 14(1), 373–387, doi:10.1029/1999GB900091, 2000.

2351 Niwa, Y., Fujii, Y., Sawa, Y., Iida, Y., Ito, A., Satoh, M., Imasu, R., Tsuboi, K., Matsueda, H.
2352 and Saigusa, N.: A 4D-Var inversion system based on the icosahedral grid model
2353 (NICAM-TM 4D-Var v1.0) - Part 2: Optimization scheme and identical twin experiment
2354 of atmospheric CO₂ inversion, *Geosci. Model Dev.*, 10(6), 2201–2219,
2355 doi:10.5194/gmd-10-2201-2017, 2017.

2356 Orr, J. C., Najjar, R. G., Aumont, O., Bopp, L., Bullister, J. L., Danabasoglu, G., Doney, S. C.,
2357 Dunne, J. P., Dutay, J.-C., Graven, H., Griffies, S. M., John, J. G., Joos, F., Levin, I.,
2358 Lindsay, K., Matear, R. J., McKinley, G. A., Mouchet, A., Oschlies, A., Romanou, A.,
2359 Schlitzer, R., Tagliabue, A., Tanhua, T. and Yool, A.: Biogeochemical protocols and
2360 diagnostics for the CMIP6 Ocean Model Intercomparison Project (OMIP), *Geosci.*
2361 *Model Dev.*, 10(6), 2169–2199, doi:10.5194/gmd-10-2169-2017, 2017.

2362 Palmer, P. I., Feng, L., Baker, D., Chevallier, F., Bösch, H. and Somkuti, P.: dominate pan-
2363 tropical atmospheric CO₂ signal, *Nat. Commun.*, 1–9, doi:10.1038/s41467-019-
2364 11097-w, 2019.

2365 Patra, P. K., Takigawa, M., Watanabe, S., Chandra, N., Ishijima, K. and Yamashita, Y.:
2366 Improved Chemical Tracer Simulation by MIROC4.0-based Atmospheric Chemistry-
2367 Transport Model (MIROC4-ACTM), *Sola*, 14(0), 91–96, doi:10.2151/sola.2018-016,
2368 2018.

2369 Paulsen, H., Ilyina, T., Six, K. D. and Stemmler, I.: Incorporating a prognostic representation
2370 of marine nitrogen fixers into the global ocean biogeochemical model HAMOCC, *J.*
2371 *Adv. Model. Earth Syst.*, 9(1), 438–464, doi:10.1002/2016MS000737, 2017.

2372 Peters, G. P., Minx, J. C., Weber, C. L. and Edenhofer, O.: Growth in emission transfers via
2373 international trade from 1990 to 2008, *Proc. Natl. Acad. Sci. U. S. A.*, 108(21), 8903–

2374 8908, doi:10.1073/pnas.1006388108, 2011.

2375 Peters, G. P., Davis, S. J. and Andrew, R.: A synthesis of carbon in international trade,
2376 Biogeosciences, 9(8), 3247–3276, doi:10.5194/bg-9-3247-2012, 2012a.

2377 Peters, G. P., Marland, G., Le Quéré, C., Boden, T., Canadell, J. G. and Raupach, M. R.: Rapid
2378 growth in CO₂ emissions after the 2008–2009 global financial crisis, Nat. Clim. Chang.,
2379 2(1), 2–4, doi:10.1038/nclimate1332, 2012b.

2380 Peters, G. P., Andrew, R. M., Boden, T., Canadell, J. G., Ciais, P., Le Quéré, C., Marland, G.,
2381 Raupach, M. R. and Wilson, C.: The challenge to keep global warming below 2 °C, Nat.
2382 Clim. Chang., 3(1), 4–6, doi:10.1038/nclimate1783, 2013.

2383 Peters, G. P., Le Quéré, C., Andrew, R. M., Canadell, J. G., Friedlingstein, P., Ilyina, T.,
2384 Jackson, R. B., Joos, F., Korsbakken, J. I., McKinley, G. A., Sitch, S. and Tans, P.:
2385 Towards real-time verification of CO₂ emissions, Nat. Clim. Chang., 7(12), 848–850,
2386 doi:10.1038/s41558-017-0013-9, 2017.

2387 Peters, G. P., Andrew, R. M., Canadell, J. G., Friedlingstein, P., Jackson, R. B., Korsbakken, J.
2388 I., Le Quéré, C. and Peregón, A.: Carbon dioxide emissions continue to grow amidst
2389 slowly emerging climate policies, Nat. Clim. Chang., 10(1), 3–6, doi:10.1038/s41558-
2390 019-0659-6, 2019.

2391 Peylin, P., Law, R. M., Gurney, K. R., Chevallier, F., Jacobson, A. R., Maki, T., Niwa, Y., Patra,
2392 P. K., Peters, W., Rayner, P. J., Rödenbeck, C., van der Laan-Luijkx, I. T. and Zhang, X.:
2393 Global atmospheric carbon budget: results from an ensemble of atmospheric CO₂
2394 inversions, Biogeosciences, 10(10), 6699–6720, doi:10.5194/bg-10-6699-2013, 2013.

2395 Pfeil, B., Olsen, A., Bakker, D. C. E., Hankin, S., Koyuk, H., Kozyr, A., Malczyk, J., Manke, A.,
2396 Metzl, N., Sabine, C. L., Aki, J., Alin, S. R., Bates, N., Bellerby, R. G. J., Borges, A.,
2397 Boutin, J., Brown, P. J., Cai, W. J., Chavez, F. P., Chen, A., Cosca, C., Fassbender, A. J.,

2398 Feely, R. A., Gonzalez-Davila, M., Goyet, C., Hales, B., Hardman-Mountford, N.,
2399 Heinze, C., Hood, M., Hoppema, M., Hunt, C. W., Hydes, D., Ishii, M., Johannessen, T.,
2400 Jones, S. D., Key, R. M., Kortzinger, A., Landschutzer, P., Lauvset, S. K., Lefevre, N.,
2401 Lenton, A., Lourantou, A., Merlivat, L., Midorikawa, T., Mintrop, L., Miyazaki, C.,
2402 Murata, A., Nakadate, A., Nakano, Y., Nakaoka, S., Nojiri, Y., Omar, A. M., Padin, X. A.,
2403 Park, G. H., Paterson, K., Perez, F. F., Pierrot, D., Poisson, A., Rios, A. F., Santana-
2404 Casiano, J. M., Salisbury, J., Sarma, V. V. S. S., Schlitzer, R., Schneider, B., Schuster, U.,
2405 Sieger, R., Skjelvan, I., Steinhoff, T., Suzuki, T., Takahashi, T., Tedesco, K., Telszewski,
2406 M., Thomas, H., Tilbrook, B., Tjiputra, J., Vandemark, D., Veness, T., Wanninkhof, R.,
2407 Watson, A. J., Weiss, R., Wong, C. S. and Yoshikawa-Inoue, H.: A uniform, quality
2408 controlled Surface Ocean CO₂ Atlas (SOCAT), *Earth Syst. Sci. Data*, 5(1), 125–143,
2409 doi:10.5194/essd-5-125-2013, 2013.

2410 Pongratz, J., Reick, C. H., Raddatz, T. and Claussen, M.: Effects of anthropogenic land cover
2411 change on the carbon cycle of the last millennium, *Global Biogeochem. Cycles*, 23(4),
2412 GB4001, doi:10.1029/2009GB003488, 2009.

2413 Pongratz, J., Reick, C. H., Houghton, R. A. and House, J. I.: Terminology as a key uncertainty
2414 in net land use and land cover change carbon flux estimates, *Earth Syst. Dyn.*, 5(1),
2415 177–195, doi:10.5194/esd-5-177-2014, 2014.

2416 Poulter, B., Frank, D. C., Hodson, E. L. and Zimmermann, N. E.: Impacts of land cover and
2417 climate data selection on understanding terrestrial carbon dynamics and the CO₂
2418 airborne fraction, *Biogeosciences*, 8(8), 2027–2036, doi:10.5194/bg-8-2027-2011,
2419 2011.

2420 Prentice, I. C., Farquhar, G. D., Fasham, M. J. R., Goulden, M. L., Heimann, M., Jaramillo, V.
2421 J., Kheshgi, H. S., Le Quéré, C., Scholes, R. J., Wallace, D. W. R. and Press, C. U.: The

2422 Carbon Cycle and Atmospheric Carbon Dioxide, in *Climate Change 2001: The Scientific*
2423 *Basis. Contribution of Working Group I to the Third Assessment Report of the*
2424 *Intergovernmental Panel on Climate Change*, edited by J. T. Houghton, Y. Ding, D. J.
2425 Griggs, M. Noguer, P. J. van der Linden, X. Dai, K. Maskell, and C. A. Johnson, pp. 183–
2426 237, Cambridge University Press, Cambridge, United Kingdom and New York, NY,
2427 USA., 2001.

2428 Price, J. T. and Warren, R.: Review of the Potential of “Blue Carbon” Activities to Reduce
2429 Emissions; available at: [http://avoid-net-uk.cc.ic.ac.uk/wp-](http://avoid-net-uk.cc.ic.ac.uk/wp-content/uploads/delightful-downloads/2016/03/Literature-review-of-the-potential-of-blue-carbon-activities-to-reduce-emissions-AVOID.)
2430 [content/uploads/delightful-](http://avoid-net-uk.cc.ic.ac.uk/wp-content/uploads/delightful-downloads/2016/03/Literature-review-of-the-potential-of-blue-carbon-activities-to-reduce-emissions-AVOID.) downloads/2016/03/Literature-review-of-the-potential-
2431 of-blue- carbon-activities-to-reduce-emissions-AVOID., 2016.

2432 Le Quéré, C., Raupach, M. R., Canadell, J. G., Marland, G., Bopp, L., Ciais, P., Conway, T. J.,
2433 Doney, S. C., Feely, R. A., Foster, P., Friedlingstein, P., Gurney, K., Houghton, R. A.,
2434 House, J. I., Huntingford, C., Levy, P. E., Lomas, M. R., Majkut, J., Metzler, N., Ometto, J.
2435 P., Peters, G. P., Prentice, I. C., Randerson, J. T., Running, S. W., Sarmiento, J. L.,
2436 Schuster, U., Sitch, S., Takahashi, T., Viovy, N., Van Der Werf, G. R. and Woodward, F.
2437 I.: Trends in the sources and sinks of carbon dioxide, *Nat. Geosci.*, 2(12), 831–836,
2438 doi:10.1038/ngeo689, 2009.

2439 Le Quéré, C., Andres, R. J., Boden, T., Conway, T., Houghton, R. A., House, J. I., Marland, G.,
2440 Peters, G. P., van der Werf, G. R., Ahlström, A., Andrew, R. M., Bopp, L., Canadell, J.
2441 G., Ciais, P., Doney, S. C., Enright, C., Friedlingstein, P., Huntingford, C., Jain, A. K.,
2442 Jourdain, C., Kato, E., Keeling, R. F., Klein Goldewijk, K., Levis, S., Levy, P., Lomas, M.,
2443 Poulter, B., Raupach, M. R., Schwinger, J., Sitch, S., Stocker, B. D., Viovy, N., Zaehle, S.
2444 and Zeng, N.: The global carbon budget 1959–2011, *Earth Syst. Sci. Data*, 5(1), 165–
2445 185, doi:10.5194/essd-5-165-2013, 2013.

2446 Le Quéré, C., Peters, G. P., Andres, R. J., Andrew, R. M., Boden, T. A., Ciais, P.,
2447 Friedlingstein, P., Houghton, R. A., Marland, G., Moriarty, R., Sitch, S., Tans, P., Arneth,
2448 A., Arvanitis, A., Bakker, D. C. E., Bopp, L., Canadell, J. G., Chini, L. P., Doney, S. C.,
2449 Harper, A., Harris, I., House, J. I., Jain, A. K., Jones, S. D., Kato, E., Keeling, R. F., Klein
2450 Goldewijk, K., Körtzinger, A., Koven, C., Lefèvre, N., Maignan, F., Omar, A., Ono, T.,
2451 Park, G.-H., Pfeil, B., Poulter, B., Raupach, M. R., Regnier, P., Rödenbeck, C., Saito, S.,
2452 Schwinger, J., Segschneider, J., Stocker, B. D., Takahashi, T., Tilbrook, B., van Heuven,
2453 S., Viovy, N., Wanninkhof, R., Wiltshire, A. and Zaehle, S.: Global carbon budget 2013,
2454 Earth Syst. Sci. Data, 6(1), 235–263, doi:10.5194/essd-6-235-2014, 2014a.

2455 Le Quéré, C., Peters, G. P., Andres, R. J., Andrew, R. M., Boden, T. a., Ciais, P.,
2456 Friedlingstein, P., Houghton, R. a., Marland, G., Moriarty, R., Sitch, S., Tans, P., Arneth,
2457 A., Arvanitis, A., Bakker, D. C. E., Bopp, L., Canadell, J. G., Chini, L. P., Doney, S. C.,
2458 Harper, A., Harris, I., House, J. I., Jain, a. K., Jones, S. D., Kato, E., Keeling, R. F., Klein
2459 Goldewijk, K., Körtzinger, A., Koven, C., Lefèvre, N., Maignan, F., Omar, A., Ono, T.,
2460 Park, G.-H., Pfeil, B., Poulter, B., Raupach, M. R., Regnier, P., Rödenbeck, C., Saito, S.,
2461 Schwinger, J., Segschneider, J., Stocker, B. D., Takahashi, T., Tilbrook, B., van Heuven,
2462 S., Viovy, N., Wanninkhof, R., Wiltshire, A. and Zaehle, S.: Global carbon budget 2013,
2463 Earth Syst. Sci. Data, 6(1), 235–263, doi:10.5194/essd-6-235-2014, 2014b.

2464 Le Quéré, C., Moriarty, R., Andrew, R. M., Peters, G. P., Ciais, P., Friedlingstein, P., Jones, S.
2465 D., Sitch, S., Tans, P., Arneth, A., Boden, T. A., Bopp, L., Bozec, Y., Canadell, J. G., Chini,
2466 L. P., Chevallier, F., Cosca, C. E., Harris, I., Hoppema, M., Houghton, R. A., House, J. I.,
2467 Jain, A. K., Johannessen, T., Kato, E., Keeling, R. F., Kitidis, V., Klein Goldewijk, K.,
2468 Koven, C., Landa, C. S., Landschützer, P., Lenton, A., Lima, I. D., Marland, G., Mathis, J.
2469 T., Metzl, N., Nojiri, Y., Olsen, A., Ono, T., Peng, S., Peters, W., Pfeil, B., Poulter, B.,

2470 Raupach, M. R., Regnier, P., Rödenbeck, C., Saito, S., Salisbury, J. E., Schuster, U.,
2471 Schwinger, J., Séférian, R., Segschneider, J., Steinhoff, T., Stocker, B. D., Sutton, A. J.,
2472 Takahashi, T., Tilbrook, B., van der Werf, G. R., Viovy, N., Wang, Y. P., Wanninkhof, R.,
2473 Wiltshire, A. and Zeng, N.: Global carbon budget 2014, *Earth Syst. Sci. Data*, 7(1), 47–
2474 85, doi:10.5194/essd-7-47-2015, 2015a.

2475 Le Quéré, C., Moriarty, R., Andrew, R. M., Canadell, J. G., Sitch, S., Korsbakken, J. I.,
2476 Friedlingstein, P., Peters, G. P., Andres, R. J., Boden, T. A., Houghton, R. A., House, J. I.,
2477 Keeling, R. F., Tans, P., Arneeth, A., Bakker, D. C. E., Barbero, L., Bopp, L., Chang, J.,
2478 Chevallier, F., Chini, L. P., Ciais, P., Fader, M., Feely, R. A., Gkritzalis, T., Harris, I.,
2479 Hauck, J., Ilyina, T., Jain, A. K., Kato, E., Kitidis, V., Klein Goldewijk, K., Koven, C.,
2480 Landschützer, P., Lauvset, S. K., Lefèvre, N., Lenton, A., Lima, I. D., Metzl, N., Millero,
2481 F., Munro, D. R., Murata, A., S. Nabel, J. E. M., Nakaoka, S., Nojiri, Y., O'Brien, K.,
2482 Olsen, A., Ono, T., Pérez, F. F., Pfeil, B., Pierrot, D., Poulter, B., Rehder, G., Rödenbeck,
2483 C., Saito, S., Schuster, U., Schwinger, J., Séférian, R., Steinhoff, T., Stocker, B. D.,
2484 Sutton, A. J., Takahashi, T., Tilbrook, B., Van Der Laan-Luijkx, I. T., Van Der Werf, G. R.,
2485 Van Heuven, S., Vandemark, D., Viovy, N., Wiltshire, A., Zaehle, S. and Zeng, N.: Global
2486 Carbon Budget 2015, *Earth Syst. Sci. Data*, doi:10.5194/essd-7-349-2015, 2015b.

2487 Le Quéré, C., Andrew, R. M., Canadell, J. G., Sitch, S., Ivar Korsbakken, J., Peters, G. P.,
2488 Manning, A. C., Boden, T. A., Tans, P. P., Houghton, R. A., Keeling, R. F., Alin, S.,
2489 Andrews, O. D., Anthoni, P., Barbero, L., Bopp, L., Chevallier, F., Chini, L. P., Ciais, P.,
2490 Currie, K., Delire, C., Doney, S. C., Friedlingstein, P., Gkritzalis, T., Harris, I., Hauck, J.,
2491 Haverd, V., Hoppema, M., Klein Goldewijk, K., Jain, A. K., Kato, E., Körtzinger, A.,
2492 Landschützer, P., Lefèvre, N., Lenton, A., Lienert, S., Lombardozi, D., Melton, J. R.,
2493 Metzl, N., Millero, F., Monteiro, P. M. S., Munro, D. R., Nabel, J. E. M. S., Nakaoka, S.

2494 I., O'Brien, K., Olsen, A., Omar, A. M., Ono, T., Pierrot, D., Poulter, B., Rödenbeck, C.,
 2495 Salisbury, J., Schuster, U., Schwinger, J., Séférian, R., Skjelvan, I., Stocker, B. D., Sutton,
 2496 A. J., Takahashi, T., Tian, H., Tilbrook, B., Van Der Laan-Luijkx, I. T., Van Der Werf, G.
 2497 R., Viovy, N., Walker, A. P., Wiltshire, A. J. and Zaehle, S.: Global Carbon Budget 2016,
 2498 Earth Syst. Sci. Data, doi:10.5194/essd-8-605-2016, 2016.

2499 Le Quéré, C., Andrew, R. M., Friedlingstein, P., Sitch, S., Pongratz, J., Manning, A. C.,
 2500 Korsbakken, J. I., Peters, G. P., Canadell, J. G., Jackson, R. B., Boden, T. A., Tans, P. P.,
 2501 Andrews, O. D., Arora, V. K., Bakker, D. C. E., Barbero, L., Becker, M., Betts, R. A.,
 2502 Bopp, L., Chevallier, F., Chini, L. P., Ciais, P., Cosca, C. E., Cross, J., Currie, K., Gasser, T.,
 2503 Harris, I., Hauck, J., Haverd, V., Houghton, R. A., Hunt, C. W., Hurtt, G., Ilyina, T., Jain,
 2504 A. K., Kato, E., Kautz, M., Keeling, R. F., Klein Goldewijk, K., Körtzinger, A.,
 2505 Landschützer, P., Lefèvre, N., Lenton, A., Lienert, S., Lima, I., Lombardozzi, D., Metzl,
 2506 N., Millero, F., Monteiro, P. M. S., Munro, D. R., Nabel, J. E. M. S., Nakaoka, S., Nojiri,
 2507 Y., Padin, X. A., Peregon, A., Pfeil, B., Pierrot, D., Poulter, B., Rehder, G., Reimer, J.,
 2508 Rödenbeck, C., Schwinger, J., Séférian, R., Skjelvan, I., Stocker, B. D., Tian, H., Tilbrook,
 2509 B., Tubiello, F. N., van der Laan-Luijkx, I. T., van der Werf, G. R., van Heuven, S., Viovy,
 2510 N., Vuichard, N., Walker, A. P., Watson, A. J., Wiltshire, A. J., Zaehle, S. and Zhu, D.:
 2511 Global Carbon Budget 2017, Earth Syst. Sci. Data, 10(1), 405–448, doi:10.5194/essd-
 2512 10-405-2018, 2018a.

2513 Le Quéré, C., Andrew, R. M., Friedlingstein, P., Sitch, S., Hauck, J., Pongratz, J., Pickers, P.
 2514 A., Korsbakken, J. I., Peters, G. P., Canadell, J. G., Arneeth, A., Arora, V. K., Barbero, L.,
 2515 Bastos, A., Bopp, L., Chevallier, F., Chini, L. P., Ciais, P., Doney, S. C., Gkritzalis, T., Goll,
 2516 D. S., Harris, I., Haverd, V., Hoffman, F. M., Hoppema, M., Houghton, R. A., Hurtt, G.,
 2517 Ilyina, T., Jain, A. K., Johannessen, T., Jones, C. D., Kato, E., Keeling, R. F., Goldewijk, K.

2518 K., Landschützer, P., Lefèvre, N., Lienert, S., Liu, Z., Lombardozzi, D., Metzl, N., Munro,
2519 D. R., Nabel, J. E. M. S., Nakaoka, S., Neill, C., Olsen, A., Ono, T., Patra, P., Peregon, A.,
2520 Peters, W., Peylin, P., Pfeil, B., Pierrot, D., Poulter, B., Rehder, G., Resplandy, L.,
2521 Robertson, E., Rocher, M., Rödenbeck, C., Schuster, U., Schwinger, J., Séférian, R.,
2522 Skjelvan, I., Steinhoff, T., Sutton, A., Tans, P. P., Tian, H., Tilbrook, B., Tubiello, F. N.,
2523 van der Laan-Luijkx, I. T., van der Werf, G. R., Viovy, N., Walker, A. P., Wiltshire, A. J.,
2524 Wright, R., Zaehle, S. and Zheng, B.: Global Carbon Budget 2018, *Earth Syst. Sci. Data*,
2525 10(4), 2141–2194, doi:10.5194/essd-10-2141-2018, 2018b.

2526 Le Quéré, C., Korsbakken, J. I., Wilson, C., Tosun, J., Andrew, R., Andres, R. J., Canadell, J.
2527 G., Jordan, A., Peters, G. P. and van Vuuren, D. P.: Drivers of declining CO₂ emissions
2528 in 18 developed economies, *Nat. Clim. Chang.*, 9(3), 213–217, doi:10.1038/s41558-
2529 019-0419-7, 2019.

2530 Le Quéré, C., Jackson, R. B., Jones, M. W., Smith, A. J. P., Abernethy, S., Andrew, R. M., De-
2531 Gol, A. J., Willis, D. R., Shan, Y., Canadell, J. G., Friedlingstein, P., Creutzig, F. and
2532 Peters, G. P.: Temporary reduction in daily global CO₂ emissions during the COVID-19
2533 forced confinement, *Nat. Clim. Chang.*, 10(7), 647–653, doi:10.1038/s41558-020-
2534 0797-x, 2020.

2535 Raupach, M. R., Marland, G., Ciais, P., Le Quéré, C., Canadell, J. G., Klepper, G. and Field, C.
2536 B.: Global and regional drivers of accelerating CO₂ emissions, *Proc Natl Acad Sci U S A*,
2537 104(24), 10288–10293, doi:10.1073/pnas.0700609104, 2007.

2538 Regnier, P., Friedlingstein, P., Ciais, P., Mackenzie, F. T., Gruber, N., Janssens, I. A., Laruelle,
2539 G. G., Lauerwald, R., Luysaert, S., Andersson, A. J., Arndt, S., Arnosti, C., Borges, A. V.,
2540 Dale, A. W., Gallego-Sala, A., Goddérís, Y., Goossens, N., Hartmann, J., Heinze, C.,
2541 Ilyina, T., Joos, F., LaRowe, D. E., Leifeld, J., Meysman, F. J. R., Munhoven, G.,

2542 Raymond, P. A., Spahni, R., Suntharalingam, P. and Thullner, M.: Anthropogenic
2543 perturbation of the carbon fluxes from land to ocean, *Nat. Geosci.*, 6(8), 597–607,
2544 doi:10.1038/ngeo1830, 2013.

2545 Remaud, M., Chevallier, F., Cozic, A., Lin, X. and Bousquet, P.: On the impact of recent
2546 developments of the LMDz atmospheric general circulation model on the simulation
2547 of CO₂ transport, *Geosci. Model Dev.*, 11(11), 4489–4513, doi:10.5194/gmd-11-4489-
2548 2018, 2018.

2549 Resplandy, L., Keeling, R. F., Rödenbeck, C., Stephens, B. B., Khatiwala, S., Rodgers, K. B.,
2550 Long, M. C., Bopp, L. and Tans, P. P.: Revision of global carbon fluxes based on a
2551 reassessment of oceanic and riverine carbon transport, *Nat. Geosci.*, 11(7), 504–509,
2552 doi:10.1038/s41561-018-0151-3, 2018.

2553 Rhein, M., Rintoul, S. R., Aoki, S., Campos, E., Chambers, D., Feely, R. A., Gulev, S., Johnson,
2554 G. C., Josey, S. A., Kostianoy, A., Mauritzen, C., Roemmich, D., Talley, L. D., Wang, F.,
2555 Stocker, T., Qin, D. and Platner, G.-K.: Chapter 3: Observations: Ocean, in *Climate
2556 Change 2013 The Physical Science Basis*, Cambridge University Press., 2013.

2557 Rödenbeck, C., Houweling, S., Gloor, M. and Heimann, M.: CO₂ flux history
2558 1982–2001 inferred from atmospheric data using a global inversion of
2559 atmospheric transport, *Atmos. Chem. Phys. Discuss.*, 3(3), 2575–2659,
2560 doi:10.5194/acpd-3-2575-2003, 2003.

2561 Rödenbeck, C., Bakker, D. C. E., Metzl, N., Olsen, A., Sabine, C., Cassar, N., Reum, F.,
2562 Keeling, R. F. and Heimann, M.: Interannual sea–air CO₂ flux
2563 variability from an observation-driven ocean mixed-layer scheme, *Biogeosciences*,
2564 11(17), 4599–4613, doi:10.5194/bg-11-4599-2014, 2014.

2565 Rödenbeck, C., Bakker, D. C. E., Gruber, N., Iida, Y., Jacobson, A. R., Jones, S., Landschützer,

2566 P., Metzl, N., Nakaoka, S., Olsen, A., Park, G.-H., Peylin, P., Rodgers, K. B., Sasse, T. P.,
2567 Schuster, U., Shutler, J. D., Valsala, V., Wanninkhof, R. and Zeng, J.: Data-based
2568 estimates of the ocean carbon sink variability – first results of the Surface Ocean
2569 pCO₂ Mapping intercomparison (SOCOM), *Biogeosciences*, 12(23), 7251–7278,
2570 doi:10.5194/bg-12-7251-2015, 2015.

2571 Rödenbeck, C., Zaehle, S., Keeling, R. and Heimann, M.: How does the terrestrial carbon
2572 exchange respond to inter-annual climatic variations? A quantification based on
2573 atmospheric CO₂ data, *Biogeosciences*, 15(8), 2481–2498, doi:10.5194/bg-15-2481-
2574 2018, 2018.

2575 Rogelj, J., Schaeffer, M., Friedlingstein, P., Gillett, N. P., van Vuuren, D. P., Riahi, K., Allen,
2576 M. and Knutti, R.: Differences between carbon budget estimates unravelled, *Nat.*
2577 *Clim. Chang.*, 6(3), 245–252, doi:10.1038/Nclimate2868, 2016.

2578 Rogelj, J., Forster, P. M., Kriegler, E., Smith, C. J. and Séférian, R.: Estimating and tracking
2579 the remaining carbon budget for stringent climate targets, *Nature*, 571(7765), 335–
2580 342, doi:10.1038/s41586-019-1368-z, 2019.

2581 Saatchi, S. S., Harris, N. L., Brown, S., Lefsky, M., Mitchard, E. T. A., Salas, W., Zutta, B. R.,
2582 Buermann, W., Lewis, S. L., Hagen, S., Petrova, S., White, L., Silman, M. and Morel, A.:
2583 Benchmark map of forest carbon stocks in tropical regions across three continents,
2584 *Proc. Natl. Acad. Sci.*, 108(24), 9899–9904, doi:10.1073/pnas.1019576108, 2011.

2585 Sabine, C. L., Feely, R. A., Gruber, N., Key, R. M., Lee, K., Bullister, J. L., Wanninkhof, R.,
2586 Wong, C. S., Wallace, D. W. R., Tilbrook, B., Millero, F. J., Peng, T.-H., Kozyr, A., Ono, T.
2587 and Rio, A. F.: The Oceanic Sink for Anthropogenic CO₂, *Science* (80-.), 305(5682),
2588 367–371, doi:10.1126/science.1097403, 2004.

2589 Sarmiento, J. L., Orr, J. C. and Siegenthaler, U.: A perturbation simulation of CO₂ uptake in

2590 an ocean general circulation model, *J. Geophys. Res.*, 97(C3), 3621,
2591 doi:10.1029/91JC02849, 1992.

2592 Saunio, M., R. Stavert, A., Poulter, B., Bousquet, P., G. Canadell, J., B. Jackson, R., A.
2593 Raymond, P., J. Dlugokencky, E., Houweling, S., K. Patra, P., Ciais, P., K. Arora, V.,
2594 Bastviken, D., Bergamaschi, P., R. Blake, D., Brailsford, G., Bruhwiler, L., M. Carlson, K.,
2595 Carrol, M., Castaldi, S., Chandra, N., Crevoisier, C., M. Crill, P., Covey, K., L. Curry, C.,
2596 Etiope, G., Frankenberg, C., Gedney, N., I. Hegglin, M., Höglund-Isaksson, L., Hugelius,
2597 G., Ishizawa, M., Ito, A., Janssens-Maenhout, G., M. Jensen, K., Joos, F., Kleinen, T., B.
2598 Krummel, P., L. Langenfelds, R., G. Laruelle, G., Liu, L., MacHida, T., Maksyutov, S., C.
2599 McDonald, K., McNorton, J., A. Miller, P., R. Melton, J., Morino, I., Müller, J., Murguia-
2600 Flores, F., Naik, V., Niwa, Y., Noce, S., O’Doherty, S., J. Parker, R., Peng, C., Peng, S., P.
2601 Peters, G., Prigent, C., Prinn, R., Ramonet, M., Regnier, P., J. Riley, W., A. Rosentreter,
2602 J., Segers, A., J. Simpson, I., Shi, H., J. Smith, S., Paul Steele, L., F. Thornton, B., Tian, H.,
2603 Tohjima, Y., N. Tubiello, F., Tsuruta, A., Viovy, N., Voulgarakis, A., S. Weber, T., Van
2604 Weele, M., R. Van Der Werf, G., F. Weiss, R., Worthy, D., Wunch, D., Yin, Y., Yoshida,
2605 Y., Zhang, W., Zhang, Z., Zhao, Y., Zheng, B., Zhu, Q., Zhu, Q. and Zhuang, Q.: The
2606 global methane budget 2000-2017, *Earth Syst. Sci. Data*, 12(3), 1561–1623,
2607 doi:10.5194/essd-12-1561-2020, 2020.

2608 Schimel, D., Alves, D., Enting, I., Heimann, M., Joos, F., Raynaud, D., Wigley, T., Prater, M.,
2609 Derwent, R., Ehhalt, D., Fraser, P., Sanhueza, E., Zhou, X., Jonas, P., Charlson, R.,
2610 Rodhe, H., Sadasivan, S., Shine, K. P., Fouquart, Y., Ramaswamy, V., Solomon, S.,
2611 Srinivasan, J., Albritton, D., Derwent, R., Isaksen, I., Lal, M., Wuebbles, D. and Press, C.
2612 U.: Radiative Forcing of Climate Change, in *Climate Change 1995 The Science of*
2613 *Climate Change. Contribution of Working Group I to the Second Assessment Report of*

2614 the Intergovernmental Panel on Climate Change, edited by J. T. Houghton, L. G. Meira
2615 Rilho, B. A. Callander, N. Harris, A. Kattenberg, and K. Maskell, Cambridge University
2616 Press, Cambridge, United Kingdom and New York, NY, USA., 1995.

2617 Schimel, D., Stephens, B. B. and Fisher, J. B.: Effect of increasing CO₂ on the terrestrial
2618 carbon cycle, *Proc Natl Acad Sci U S A*, 112(2), 436–441,
2619 doi:10.1073/pnas.1407302112, 2015.

2620 Schourup-Kristensen, V., Sidorenko, D., Wolf-Gladrow, D. A. and Völker, C.: A skill
2621 assessment of the biogeochemical model REcoM2 coupled to the Finite Element Sea
2622 Ice–Ocean Model (FESOM 1.3), *Geosci. Model Dev.*, 7(6), 2769–2802,
2623 doi:10.5194/gmd-7-2769-2014, 2014.

2624 Schwinger, J., Goris, N., Tjiputra, J. F., Kriest, I., Bentsen, M., Bethke, I., Ilicak, M., Assmann,
2625 K. M. and Heinze, C.: Evaluation of NorESM-OC (versions 1 and 1.2), the ocean
2626 carbon-cycle stand-alone configuration of the Norwegian Earth System Model
2627 (NorESM1), *Geosci. Model Dev.*, 9(8), 2589–2622, doi:10.5194/gmd-9-2589-2016,
2628 2016.

2629 Séférian, R., Nabat, P., Michou, M., Saint-Martin, D., Voldoire, A., Colin, J., Decharme, B.,
2630 Delire, C., Berthet, S., Chevallier, M., Sénési, S., Franchisteguy, L., Vial, J., Mallet, M.,
2631 Joetzjer, E., Geoffroy, O., Guérémy, J., Moine, M., Msadek, R., Ribes, A., Rocher, M.,
2632 Roehrig, R., Salas-y-Méllia, D., Sanchez, E., Terray, L., Valcke, S., Waldman, R., Aumont,
2633 O., Bopp, L., Deshayes, J., Éthé, C. and Madec, G.: Evaluation of CNRM Earth System
2634 Model, CNRM-ESM2-1: Role of Earth System Processes in Present-Day and Future
2635 Climate, *J. Adv. Model. Earth Syst.*, 11(12), 4182–4227, doi:10.1029/2019MS001791,
2636 2019.

2637 Sellar, A. A., Jones, C. G., Mulcahy, J., Tang, Y., Yool, A., Wiltshire, A., O’Connor, F. M.,

2638 Stringer, M., Hill, R., Palmieri, J., Woodward, S., Mora, L., Kuhlbrodt, T., Rumbold, S.,
2639 Kelley, D. I., Ellis, R., Johnson, C. E., Walton, J., Abraham, N. L., Andrews, M. B.,
2640 Andrews, T., Archibald, A. T., Berthou, S., Burke, E., Blockley, E., Carslaw, K., Dalvi, M.,
2641 Edwards, J., Folberth, G. A., Gedney, N., Griffiths, P. T., Harper, A. B., Hendry, M. A.,
2642 Hewitt, A. J., Johnson, B., Jones, A., Jones, C. D., Keeble, J., Liddicoat, S., Morgenstern,
2643 O., Parker, R. J., Predoi, V., Robertson, E., Siahann, A., Smith, R. S., Swaminathan, R.,
2644 Woodhouse, M. T., Zeng, G. and Zerroukat, M.: UKESM1: Description and evaluation
2645 of the UK Earth System Model (accepted), *J. Adv. Model. Earth Syst.*, 2019MS001739,
2646 doi:10.1029/2019MS001739, 2019.

2647 Shevliakova, E., Pacala, S. W., Malyshev, S., Hurtt, G. C., Milly, P. C. D., Caspersen, J. P.,
2648 Sentman, L. T., Fisk, J. P., Wirth, C. and Crevoisier, C.: Carbon cycling under 300 years
2649 of land use change: Importance of the secondary vegetation sink, *Global Biogeochem.*
2650 *Cycles*, 23(2), GB2022, doi:10.1029/2007GB003176, 2009.

2651 Sitch, S., Huntingford, C., Gedney, N., Levy, P. E., Lomas, M., Piao, S. L., Betts, R., Ciais, P.,
2652 Cox, P., Friedlingstein, P., Jones, C. D., Prentice, I. C. and Woodward, F. I.: Evaluation
2653 of the terrestrial carbon cycle, future plant geography and climate-carbon cycle
2654 feedbacks using five Dynamic Global Vegetation Models (DGVMs), *Glob. Chang. Biol.*,
2655 14(2008), 2015–2039, doi:10.1111/j.1365-2486.2008.01626.x, 2008.

2656 Smith, B., Warlind, D., Arneth, A., Hickler, T., Leadley, P., Siltberg, J. and Zaehle, S.:
2657 Implications of incorporating N cycling and N limitations on primary production in an
2658 individual-based dynamic vegetation model, *Biogeosciences*, 11(7), 2027–2054,
2659 doi:10.5194/bg-11-2027-2014, 2014.

2660 Stephens, B. B., Gurney, K. R., Tans, P. P., Sweeney, C., Peters, W., Bruhwiler, L., Ciais, P.,
2661 Ramonet, M., Bousquet, P., Nakazawa, T., Aoki, S., Machida, T., Inoue, G.,

2662 Vinnichenko, N., Lloyd, J., Jordan, A., Heimann, M., Shibistova, O., Langenfelds, R. L.,
2663 Steele, L. P., Francey, R. J. and Denning, A. S.: Weak northern and strong tropical land
2664 carbon uptake from vertical profiles of atmospheric CO₂, *Science* (80-.), 316(5832),
2665 1732–1735, doi:10.1126/science.1137004, 2007.

2666 Stocker, T., Qin, D. and Plattner, G.-K.: *Climate Change 2013 The Physical Science Basis*,
2667 Cambridge University Press., 2013.

2668 Swart, N. C., Fyfe, J. C., Saenko, O. A. and Eby, M.: Wind-driven changes in the ocean
2669 carbon sink, *Biogeosciences*, 11(21), 6107–6117, doi:10.5194/bg-11-6107-2014, 2014.

2670 Tian, H., Xu, X., Lu, C., Liu, M., Ren, W., Chen, G., Melillo, J. and Liu, J.: Net exchanges of CO
2671 ₂, CH₄, and N₂O between China's terrestrial ecosystems and the atmosphere and
2672 their contributions to global climate warming, *J. Geophys. Res.*, 116(G2), G02011,
2673 doi:10.1029/2010JG001393, 2011.

2674 Tian, H., Chen, G., Lu, C., Xu, X., Hayes, D. J., Ren, W., Pan, S., Huntzinger, D. N. and Wofsy,
2675 S. C.: North American terrestrial CO₂ uptake largely offset by CH₄ and N₂O emissions:
2676 toward a full accounting of the greenhouse gas budget, *Clim Chang.*, 129(3–4), 413–
2677 426, doi:10.1007/s10584-014-1072-9, 2015.

2678 Todd-Brown, K. E. O., Randerson, J. T., Post, W. M., Hoffman, F. M., Tarnocai, C., Schuur, E.
2679 A. G. and Allison, S. D.: Causes of variation in soil carbon simulations from CMIP5
2680 Earth system models and comparison with observations, *Biogeosciences*, 10(3), 1717–
2681 1736, doi:10.5194/bg-10-1717-2013, 2013.

2682 UN: United Nations Statistics Division: Energy Statistics, available at:
2683 <http://unstats.un.org/unsd/energy/>, last access: 27 September 2019., 2020.

2684 UNFCCC: National Inventory Submissions, available at: [https://unfccc.int/process-and-](https://unfccc.int/process-and-meetings/transparency-and-reporting/reporting-and-review-under-the-)
2685 [meetings/transparency-and-reporting/reporting-and-review-under-the-](https://unfccc.int/process-and-meetings/transparency-and-reporting/reporting-and-review-under-the-)

2686 convention/greenhouse-gas-inventories-annex-i-parties/national-inventory-
2687 submissions-2020, last access: 27 Sept., 2020.

2688 van der Velde, I. R., Miller, J. B., Schaefer, K., van der Werf, G. R., Krol, M. C. and Peters,
2689 W.: Terrestrial cycling of ^{13}C and CO_2 by
2690 photosynthesis, respiration, and biomass burning in SiBCASA, *Biogeosciences*, 11(23),
2691 6553–6571, doi:10.5194/bg-11-6553-2014, 2014.

2692 Viovy, N.: CRUNCEP data set, available at:
2693 [ftp://nacp.ornl.gov/synthesis/2009/frescati/temp/land_use_change/original/readme.](ftp://nacp.ornl.gov/synthesis/2009/frescati/temp/land_use_change/original/readme.htm)
2694 [htm](ftp://nacp.ornl.gov/synthesis/2009/frescati/temp/land_use_change/original/readme.htm), last access: June 2016., 2016.

2695 Vuichard, N., Messina, P., Luyssaert, S., Guenet, B., Zaehle, S., Ghattas, J., Iqbal, L. and Paris-
2696 saclay, U.: Accounting for carbon and nitrogen interactions in the global terrestrial
2697 ecosystem model ORCHIDEE (trunk version , rev 4999): multi-scale evaluation of
2698 gross primary production, , 4751–4779, 2019.

2699 Walker, A. P., Quaipe, T., van Bodegom, P. M., De Kauwe, M. G., Keenan, T. F., Joiner, J.,
2700 Lomas, M. R., MacBean, N., Xu, C. G., Yang, X. J. and Woodward, F. I.: The impact of
2701 alternative trait-scaling hypotheses for the maximum photosynthetic carboxylation
2702 rate (V_{cmax}) on global gross primary production, *New Phytol.*, 215(4), 1370–1386,
2703 doi:10.1111/nph.14623, 2017.

2704 Wanninkhof, R.: Relationship between wind speed and gas exchange over the ocean, *J.*
2705 *Geophys. Res.*, 97(C5), 7373, doi:10.1029/92JC00188, 1992.

2706 Wanninkhof, R.: Relationship between wind speed and gas exchange over the ocean
2707 revisited, *Limnol. Oceanogr. Methods*, 12(6), 351–362, doi:10.4319/lom.2014.12.351,
2708 2014.

2709 Wanninkhof, R., Park, G. H., Takahashi, T., Sweeney, C., Feely, R., Nojiri, Y., Gruber, N.,

2710 Doney, S. C., McKinley, G. A., Lenton, A., Le Quéré, C., Heinze, C., Schwinger, J.,
2711 Graven, H. and Khatiwala, S.: Global ocean carbon uptake: magnitude, variability and
2712 trends, *Biogeosciences*, 10(3), 1983–2000, doi:10.5194/bg-10-1983-2013, 2013.

2713 Watson, A. J., Schuster, U., Shutler, J. D., Holding, T., Ashton, I. G. C., Landschützer, P.,
2714 Woolf, D. K. and Goddijn-Murphy, L.: Revised estimates of ocean-atmosphere CO₂
2715 flux are consistent with ocean carbon inventory, *Nat. Commun.*, 11(1), 1–6,
2716 doi:10.1038/s41467-020-18203-3, 2020.

2717 Watson, R. T., Rodhe, H., Oeschger, H., Siegenthaler, U. and Press, C. U.: Greenhouse Gases
2718 and Aerosols, in *Climate Change: The IPCC Scientific Assessment*. Intergovernmental
2719 Panel on Climate Change (IPCC), edited by J. T. Houghton, G. J. Jenkins, and J. J.
2720 Ephraums, pp. 1–40, Cambridge University Press, Cambridge., 1990.

2721 Weiss, R. F. and Price, B. A.: Nitrous oxide solubility in water and seawater, *Mar. Chem.*,
2722 8(4), 347–359, doi:10.1016/0304-4203(80)90024-9, 1980.

2723 Wenzel, S., Cox, P. M., Eyring, V. and Friedlingstein, P.: Projected land photosynthesis
2724 constrained by changes in the seasonal cycle of atmospheric CO₂, *Nature*, 538(7626),
2725 499–501, doi:10.1038/nature19772, 2016.

2726 van der Werf, G. R., Randerson, J. T., Giglio, L., Collatz, G. J., Mu, M., Kasibhatla, P. S.,
2727 Morton, D. C., DeFries, R. S., Jin, Y. and van Leeuwen, T. T.: Global fire emissions and
2728 the contribution of deforestation, savanna, forest, agricultural, and peat fires (1997–
2729 2009), *Atmos. Chem. Phys.*, 10(23), 11707–11735, doi:10.5194/acp-10-11707-2010,
2730 2010.

2731 van der Werf, G. R., Randerson, J. T., Giglio, L., van Leeuwen, T. T., Chen, Y., Rogers, B. M.,
2732 Mu, M., van Marle, M. J. E., Morton, D. C., Collatz, G. J., Yokelson, R. J. and Kasibhatla,
2733 P. S.: Global fire emissions estimates during 1997–2016, *Earth Syst. Sci. Data*, 9(2),

2734 697–720, doi:10.5194/essd-9-697-2017, 2017.

2735 Wilkenskield, S., Kloster, S., Pongratz, J., Raddatz, T. and Reick, C. H.: Comparing the
2736 influence of net and gross anthropogenic land-use and land-cover changes on the
2737 carbon cycle in the MPI-ESM, *Biogeosciences*, 11(17), 4817–4828, doi:10.5194/bg-11-
2738 4817-2014, 2014.

2739 Wiltshire, A. J., Burke, E. J., Chadburn, S. E., Jones, C. D., Cox, P. M., Davies-barnard, T.,
2740 Friedlingstein, P., Harper, A. B., Liddicoat, S., Sitch, S. and Zaehle, S.: JULES-CN : a
2741 coupled terrestrial Carbon-Nitrogen Scheme (JULES vn5 . 1), , (July), 1–40, 2020.

2742 Xi, F., Davis, S. J., Ciais, P., Crawford-Brown, D., Guan, D., Pade, C., Shi, T., Syddall, M., Lv, J.,
2743 Ji, L., Bing, L., Wang, J., Wei, W., Yang, K. H., Lagerblad, B., Galan, I., Andrade, C.,
2744 Zhang, Y. and Liu, Z.: Substantial global carbon uptake by cement carbonation, *Nat.*
2745 *Geosci.*, 9(12), 880–883, doi:10.1038/ngeo2840, 2016.

2746 Yin, X. W.: Responses of leaf nitrogen concentration and specific leaf area to atmospheric
2747 CO₂ enrichment: a retrospective synthesis across 62 species, *Glob. Chang. Biol.*, 8(7),
2748 631–642, doi:DOI 10.1046/j.1365-2486.2002.00497.x, 2002.

2749 Yue, X. and Unger, N.: The Yale Interactive terrestrial Biosphere model version 1 . 0 :
2750 description , evaluation and implementation into NASA GISS, , 2399–2417,
2751 doi:10.5194/gmd-8-2399-2015, 2015.

2752 Zaehle, S. and Friend, A. D.: Carbon and nitrogen cycle dynamics in the O-CN land surface
2753 model: 1. Model description, site-scale evaluation, and sensitivity to parameter
2754 estimates, *Global Biogeochem. Cycles*, 24(1), GB1005, doi:10.1029/2009GB003521,
2755 2010.

2756 Zaehle, S., Ciais, P., Friend, A. D. and Prieur, V.: Carbon benefits of anthropogenic reactive
2757 nitrogen offset by nitrous oxide emissions, *Nat. Geosci.*, 4(9), 601–605,

2758 doi:10.1038/ngeo1207, 2011.

2759 Zheng, B., Chevallier, F., Yin, Y., Ciais, P., Fortems-Cheiney, A., Deeter, M. N., Parker, R. J.,
2760 Wang, Y., Worden, H. M. and Zhao, Y.: Global atmospheric carbon monoxide budget
2761 2000–2017 inferred from multi-species atmospheric inversions, *Earth Syst. Sci. Data*,
2762 11(3), 1411–1436, doi:10.5194/essd-11-1411-2019, 2019.

2763 Zscheischler, J., Mahecha, M. D., Avitabile, V., Calle, L., Carvalhais, N., Ciais, P., Gans, F.,
2764 Gruber, N., Hartmann, J., Herold, M., Ichii, K., Jung, M., Landschutzer, P., Laruelle, G.
2765 G., Lauerwald, R., Papale, D., Peylin, P., Poulter, B., Ray, D., Regnier, P., Rödenbeck, C.,
2766 Roman-Cuesta, R. M., Schwalm, C., Tramontana, G., Tyukavina, A., Valentini, R., van
2767 der Werf, G., West, T. O., Wolf, J. E. and Reichstein, M.: Reviews and syntheses: An
2768 empirical spatiotemporal description of the global surface-atmosphere carbon fluxes:
2769 opportunities and data limitations, *Biogeosciences*, 14(15), 3685–3703,
2770 doi:10.5194/bg-14-3685-2017, 2017.

2771

2772

2773

2774 **Tables**

2775

2776

Table 1. Factors used to convert carbon in various units (by convention, Unit 1 = Unit 2 × conversion).

Unit 1	Unit 2	Conversion	Source
GtC (gigatonnes of carbon)	ppm (parts per million) ^a	2.124 ^b	Ballantyne et al. (2012)
GtC (gigatonnes of carbon)	PgC (petagrams of carbon)	1	SI unit conversion
GtCO ₂ (gigatonnes of carbon dioxide)	GtC (gigatonnes of carbon)	3.664	44.01/12.011 in mass equivalent
GtC (gigatonnes of carbon)	MtC (megatonnes of carbon)	1000	SI unit conversion

^a Measurements of atmospheric CO₂ concentration have units of dry-air mole fraction. ‘ppm’ is an abbreviation for micromole/mol, dry air.

^bThe use of a factor of 2.124 assumes that all the atmosphere is well mixed within one year. In reality, only the troposphere is well mixed and the growth rate of CO₂ concentration in the less well-mixed stratosphere is not measured by sites from the NOAA network. Using a factor of 2.124 makes the approximation that the growth rate of CO₂ concentration in the stratosphere equals that of the troposphere on a yearly basis.

2777

2778

2779

Table 2. How to cite the individual components of the global carbon budget presented here.	
Component	Primary reference
Global fossil CO ₂ emissions (EFOS), total and by fuel type	Global Carbon Project (2020)
National territorial fossil CO ₂ emissions (EFOS)	CDIAC source: Gilfillan et al. (2020)
	UNFCCC (2020)
National consumption-based fossil CO ₂ emissions (EFOS) by country (consumption)	Peters et al. (2011b) updated as described in this paper
Net land-use change flux (ELUC)	Average from Houghton and Nassikas (2017), Hansis et al. (2015), Gasser et al. (2020), all updated as described in this paper
Growth rate in atmospheric CO ₂ concentration (GATM)	Dlugokencky and Tans (2020)
Ocean and land CO ₂ sinks (SOCEAN and SLAND)	This paper for SOCEAN and SLAND and references in Table 4 for individual models.

2780

Table 3. Main methodological changes in the global carbon budget since 2016. Methodological changes introduced in one year are kept for the following years unless noted. Empty cells mean there were no methodological changes introduced that year. Table A7 lists methodological changes from the first global carbon budget publication up to 2015.

Publication year	Fossil fuel emissions			LUC emissions	Reservoirs			Uncertainty & other changes
	Global	Country (territorial)	Country (consumption)		Atmosphere	Ocean	Land	
2016	Two years of BP data	Added three small countries; China's emissions from 1990 from BP data (this release only)		Preliminary ELUC using FRA-2015 shown for comparison ; use of five DGVMs		Based on seven models	Based on fourteen models	Discussion of projection for full budget for current year
Le Quéré et al. (2016)								
2017	Projection includes India-specific data			Average of two bookkeeping models; use of twelve DGVMs		Based on eight models that match the observed sink for the 1990s; no longer normalised	Based on fifteen models that meet observation-based criteria (see Sect. 2.5)	Land multi-model average now used in main carbon budget, with the carbon imbalance presented separately; new table of key uncertainties
Le Quéré et al. (2018a) GCB2017								
2018	Revision in cement emissions; Projection includes EU-specific data	Aggregation of overseas territories into governing nations for total of 213 countries a		Use of sixteen DGVMs	Use of four atmospheric inversions	Based on seven models	Based on sixteen models; revised atmospheric forcing from CRUNCEP to CRU-JRA-55	Introduction of metrics for evaluation of individual models using observations
Le Quéré et al. (2018b) GCB2018								

2019	Global emissions calculated as sum of all countries plus bunkers, rather than taken directly from CDIAC.							
Friedlingstein et al. (2019) GCB2019				Use of fifteen DGVMs (a)	Use of three atmospheric inversions	Based on nine models	Based on sixteen models	
2020	Cement carbonation now included in the EFOS estimate, reducing EFOS by about 0.2GtC yr-1 for the last decade	India's emissions from Andrew (2020: India); Corrections to Netherland Antilles and Aruba and Soviet emissions before 1950 as per Andrew (2020: CO2); China's coal emissions in 2019 derived from official statistics, emissions now shown for EU27 instead of EU28. Projection for 2020 based on assessment of four approaches						
(this study) GCB2020			Average of three bookkeeping models; use of 17 DGVMs (a)	Use of five atmospheric inversions	Based on nine models. River flux revised and partitioned NH, Tropics, SH	Based on seventeen models		

(a) ELUC is still estimated based on bookkeeping models, as in 2018 (Le Quéré et al., 2018b), but the number of DGVMs used to characterise the uncertainty has changed.								

Table 4. References for the process models, pCO₂-based ocean flux products, and atmospheric inversions included in Figs. 6-8. All models and products are updated with new data to end of year 2019, and the atmospheric forcing for the DGVMs has been updated as described in Section 2.2.2.

Model/data name	Reference	Change from Global Carbon Budget 2019 (Friedlingstein et al., 2019)
<i>Bookkeeping models for land-use change emissions</i>		
BLUE	Hansis et al. (2015)	No change.
H&N2017	Houghton and Nassikas (2017)	No change.
OSCAR	Gasser et al. (2020) (a)	Newly included.
<i>Dynamic global vegetation models</i>		
CABLE-POP	Haverd et al. (2018)	no change
CLASSIC	Melton et al. (2020)	Formerly called CLASS-CTEM. Evaporation from top soil layer is reduced which increases soil moisture and yields better GPP especially in dry and semi-arid regions.
CLM5.0	Lawrence et al. (2019)	No Change.
DLEM	Tian et al. (2015) (b)	Updated algorithms for land use change processes.
ISAM	Meiyappan et al. (2015)	No Change.
ISBA-CTRIP	Delire et al. (2020) (c)	Updated spinup protocol + model name updated (SURFEXv8 in GCB2017) + inclusion of crop harvesting module
JSBACH	Mauritsen et al. (2019)	No Change.
JULES-ES	Sellar et al., (2019), Wiltshire et al., (2020) (d)	No Change.
LPJ-GUESS	Smith et al. (2014) (e)	Bug fixes and output code restructuring.
LPJ	Poulter et al. (2011) (f)	No Change.

LPX-Bern	Lienert and Joos (2018)	Changed compiler to Intel Fortran from PGI.
OCN	Zaehle and Friend (2010) (g)	No change (uses r294).
ORCHIDEE-CNP	Goll et al. (2017) (h)	No major changes, except some small bug corrections linked to the implementation of land cover changes. PFT specific parameters refined.
ORCHIDEEv3	Vuichard et al. (2019), Zaehle and Friend (2010), Krinner et al. (2005)	Inclusion of N cycle and CN interactions in ORCHIDEE2.2 (ie CMIP6) version
SDGVM	Walker et al. (2017) (i)	No changes from version used in Friedlingstein et al. (2019).
VISIT	Kato et al. (2013) (j)	Change to distinguish managed pasture/rangeland information when conversion from natural vegetation to pasture occurs. Add upper limit of deforested biomass from secondary land using the mean biomass density data of LUH2.
YIBs	Yue and Unger (2015)	New this year.
<i>Global ocean biogeochemistry models</i>		
NEMO-PlankTOM5	Buitenhuis et al. (2013)	No change
MICOM-HAMOCC (NorESM-OCv1.2)	Schwinger et al. (2016)	No change
MPIOM-HAMOCC6	Paulsen et al. (2017)	No change
NEMO3.6-PISCESv2-gas (CNRM)	Berthet et al. (2019) (k)	minor bug fixes and updated spin-up procedures
CSIRO	Law et al (2017)	small bug fixes and revised model-spin-up
FESOM-1.4-REcoM2	Hauck et al. (2020) (l)	new physical model this year
MOM6-COBALT (Princeton)	Liao et al. (2020)	No change
CESM-ETHZ	Doney et al. (2009)	included water vapor correction when converting from xCO2 to pCO2.
NEMO-PISCES (IPSL)	Aumont et al. (2015)	updated spin-up procedure
<i>pCO2-based flux ocean products</i>		
Landschützer (MPI-SOMFFN)	Landschützer et al. (2016)	update to SOCATv2020 measurements and timeperiod 1982-2019; Now use of ERA5 winds instead of ERA interim

Rödenbeck (Jena-MLS)	Rödenbeck et al. (2014)	update to SOCATv2020 measurements, involvement of a multi-linear regression for extrapolation (combined with an explicitly interannual correction), use of OCIM (deVries et al., 2014) as decadal prior, carbonate chemistry parameterization now time-dependent, grid resolution increased to 2.5*2 degrees, adjustable degrees of freedom now also covering shallow areas and Arctic
CMEMS	Chau et al. (2020)	Update to SOCATv2020 measurements and extend time period 1985-2019. Use the parameterization of air-sea CO2 fluxes as in Wanninkhof 2014 instead of Wanninkhof 1992
CSIR-ML6	Gregor et al. (2019)	New this year
Watson et al.	Watson et al. (2020)	New this year
<i>Atmospheric inversions</i>		
CAMS	Chevallier et al. (2005) with updates given in https://atmosphere.copernicus.eu/ (m)	No change.
CarbonTracker Europe (CTE)	van der Laan-Luijkx et al. (2017)	Model transport driven by ERA5 reanalysis. GFAS fire emissions applied instead of SIBCASA-GFED. Rodenbeck et al ocean fluxes used as priors instead of Jacobson et al., (2007)
Jena CarboScope	Rödenbeck et al. (2003, 2018)	No change.
UoE in-situ	Feng et al., (2016) (n)	new this year
NISMON-CO2	Niwa et al., (2017)	new this year
MIROC4-ACTM	Patra et al., (2018)	new this year
(a) see also Gasser et al. (2017)		
(b) See also Tian et al. (2011)		
(c) See also Decharme et al. (2019) and Séférian et al. (2019)		
(d) JULES-ES is the Earth System configuration of the Joint UK Land Environment Simulator. See also Best et al. (2011) and Clark et al. (2011).		
(e) To account for the differences between the derivation of shortwave radiation from CRU cloudiness and DSWRF from CRUJRA, the photosynthesis scaling parameter α_a was modified (-15%) to yield similar results.		
(f) Lund-Potsdam-Jena. Compared to published version, decreased LPJ wood harvest efficiency so that 50 % of biomass was removed off-site compared to 85 % used in the 2012 budget. Residue management of managed grasslands increased so that 100 % of harvested grass enters the litter pool.		
(g) See also Zaehle et al. (2011).		
(h) See also Goll et al (2018)		

(i) See also Woodward and Lomas (2004)
(j) See also Ito and Inatomi (2012)
(k) See also Seferian et al (2019)
(l) Longer spin-up than in Hauck et al (2020); see also Schourup-Kristensen et al (2014)
(m) See also Remaud et al. (2018) GMD: doi.org/10.5194/gmd-11-4489-2018
(n) See also Feng et al., (2009), Palmer et al., (2019)

Table 5. Comparison of results from the bookkeeping method and budget residuals with results from the DGVMs and inverse estimates for different periods, the last decade, and the last year available. All values are in GtCyr⁻¹. The DGVM uncertainties represent $\pm 1\sigma$ of the decadal or annual (for 2019 only) estimates from the individual DGVMs: for the inverse models the range of available results is given. All values are rounded to the nearest 0.1 GtC and therefore columns do not necessarily add to zero.

Mean (GtC yr ⁻¹)							
	1960-1969	1970-1979	1980-1989	1990-1999	2000-2009	2010-2019	2019
<i>Land-use change emissions (ELUC)</i>							
Bookkeeping methods - Net flux (1a)	1.5±0.7	1.3±0.7	1.3±0.7	1.4±0.7	1.4±0.7	1.6±0.7	1.8±0.7
Bookkeeping methods - Source	3.5±1.2	3.3±1.1	3.5±1.3	3.8±0.9	4.1±1.2	4.4±1.6	4.6±1.8
Bookkeeping methods - Sink	-2±0.7	- 2.1±0.7	- 2.2±0.8	- 2.4±0.9	- 2.7±1.1	- 2.9±1.2	- 2.9±1.2
DGVMs - Net flux (1b)	1.4±0.5	1.4±0.5	1.5±0.5	1.4±0.5	1.6±0.5	2.1±0.5	2.2±0.7
<i>Terrestrial sink (SLAND)</i>							
Residual sink from global budget (EFF+ELUC-GATM-SOCEAN) (2a)	1.7±0.8	1.9±0.8	1.6±0.9	2.6±0.9	2.9±0.9	3.3±1.0	3.5±1.1
DGVMs (2b)	1.3±0.4	2.1±0.4	2.0±0.7	2.6±0.7	2.9±0.8	3.4±0.9	3.1±1.2
<i>Total land fluxes (SLAND – ELUC)</i>							
GCB2020 Budget (2b - 1a)	- 0.2±0.9	0.8±0.8	0.7±1.0	1.2±1.0	1.5±1.1	1.9±1.1	1.3±1.4
Budget constraint (2a - 1a)	0.3±0.6	0.6±0.6	0.3±0.7	1.2±0.7	1.5±0.7	1.8±0.8	1.7±0.7
DGVMs (2b - 1b)	- 0.2±0.5	0.7±0.4	0.5±0.6	1.2±0.4	1.3±0.6	1.3±0.6	1.0±1.1
Inversions*	-	-	0.1 - 0.6 (2)	0.6 - 1.1 (3)	1.0 - 1.8 (4)	1.2 - 2.3 (5)	0.7-1.9 (5)
*Estimates are adjusted for the pre-industrial influence of river fluxes and adjusted to common EFOS (Sect. 2.6.1). The ranges given include varying numbers (in parentheses) of inversions in each decade (Table A4).							

Table 6. Decadal mean in the five components of the anthropogenic CO₂ budget for different periods, and last year available. All values are in GtC yr⁻¹, and uncertainties are reported as $\pm 1\sigma$. The table also shows the budget imbalance (BIM), which provides a measure of the discrepancies among the nearly independent estimates and has an uncertainty exceeding ± 1 GtC yr⁻¹. A positive imbalance means the emissions are overestimated and/or the sinks are too small. All values are rounded to the nearest 0.1 GtC and therefore columns do not necessarily add to zero.

	Mean (GtC yr ⁻¹)						
	1960-1969	1970-1979	1980-1989	1990-1999	2000-2009	2010-2019	2019
<i>Total emissions (EFOS+ELUC)</i>							
Fossil CO ₂ emissions (EFOS)	3±0.2	4.7±0.2	5.4±0.3	6.3±0.3	7.7±0.4	9.4±0.5	9.7±0.5
Land-use change emissions (ELUC)	1.5±0.7	1.3±0.7	1.3±0.7	1.4±0.7	1.4±0.7	1.6±0.7	1.8±0.7
Total emissions	4.5±0.7	5.9±0.7	6.7±0.8	7.6±0.8	9.1±0.8	10.9±0.9	11.5±0.9
<i>Partitioning</i>							
Growth rate in atmospheric CO ₂ concentration (GATM)	1.8±0.07	2.8±0.07	3.4±0.02	3.2±0.02	4.1±0.02	5.1±0.02	5.4±0.2
Ocean sink (SOCEAN)	1±0.3	1.3±0.4	1.7±0.4	2±0.5	2.1±0.5	2.5±0.6	2.6±0.6
Terrestrial sink (SLAND)	1.3±0.4	2.1±0.4	2.0±0.7	2.6±0.7	2.9±0.8	3.4±0.9	3.1±1.2
<i>Budget imbalance</i>							
BIM = EFOS+ELUC - (GATM+SOCEAN+SLAND)	0.5	-0.2	-0.4	-0.1	0	-0.1	0.3

Table 7. Comparison of the projection with realised fossil CO₂ emissions (E_{FOS}). The ‘Actual’ values are first the estimate available using actual data, and the ‘Projected’ values refers to estimates made before the end of the year for each publication. Projections based on a different method from that described here during 2008-2014 are available in Le Quéré et al., (2016). All values are adjusted for leap years.

	World		China		USA		EU28		India		Rest of World	
	Project ed	Actual	Project ed	Actual	Project ed	Actual	Project ed	Actual	Project ed	Actual	Project ed	Actual
2015 (a)	-0.6%	0.06%	-3.9%	-0.7%	-1.5%	-2.5%	-	-	-	-	1.2%	1.2%
	(-1.6 to 0.5)		(-4.6 to -1.1)		(-5.5 to 0.3)						(-0.2 to 2.6)	
2016 (b)	-0.2%	0.20%	-0.5%	-0.3%	-1.7%	-2.1%	-	-	-	-	1.0%	1.3%
	(-1.0 to +1.8)		(-3.8 to +1.3)		(-4.0 to +0.6)						(-0.4 to +2.5)	
2017 (c)	2.0%	1.6%	3.5%	1.5%	-0.4%	-0.5%	-	-	2.00%	3.9%	1.6%	1.9%
	(+0.8 to +3.0)		(+0.7 to +5.4)		(-2.7 to +1.0)				(+0.2 to +3.8)		(0.0 to +3.2)	
2018 (d)	2.7%	2.1%	4.7%	2.3%	2.5%	2.8%	-0.7%	-2.1%	6.3%	8.0%	1.8%	1.7%
	(+1.8 to +3.7)		(+2.0 to +7.4)		(+0.5 to +4.5)		(-2.6 to +1.3)		(+4.3 to +8.3)		(+0.5 to +3.0)	
2019 (e)	0.5%	0.1%	2.6%	2.2%	-2.4%	-2.6%	-1.7%	-4.3%	1.8%	1.0%	0.5%	0.5%
	(-0.3 to +1.4)		(+0.7 to +4.4)		(-4.7 to -0.1)		(-5.1% to +1.8%)		(-0.7 to +3.7)		(-0.8 to +1.8)	
2020 (f)	-6.0%		-1.5%		-11.5%		-10.4% (EU27)		-11.0%		-7.3%	

(a) Jackson et al. (2016) and Le Quéré et al. (2015a). (b) Le Quéré et al. (2016). (c) Le Quéré et al. (2018a). (d) Le Quéré et al. (2018b). (e) Friedlingstein et al., (2019), (f) This study

Table 8. Cumulative CO₂ for different time periods in gigatonnes of carbon (GtC). All uncertainties are reported as $\pm 1\sigma$. The budget imbalance provides a measure of the discrepancies among the nearly independent estimates. Its uncertainty exceeds ± 60 GtC. The method used here does not capture the loss of additional sink capacity from reduced forest cover, which is about 20 GtC and would exacerbate the budget imbalance (see Sect. 2.7.4). All values are rounded to the nearest 5 GtC and therefore columns do not necessarily add to zero.

Units of GtC	1750-2019	1850-2014	1959-2019	1850-2019	1850-2020 (a)
<i>Emissions</i>					
Fossil CO ₂ emissions (EFOS)	445±20	395±20	365±20	445±20	455±20
Land-use change CO ₂ emissions (ELUC)	255±70 ^b	200±60 ^c	85±45 ^d	210±60 ^c	210±60
Total emissions	700±75	595±65	450±50	650±65	665±65
<i>Partitioning</i>					
Growth rate in atmospheric CO ₂ concentration (GATM)	285±5	235±5	205±5	265±5	270±5
Ocean sink (SOCEAN) (e)	170±20	145±20	105±20	160±20	165±20
Terrestrial sink (SLAND)	230±60	195±50	145±35	210±55	215±55
<i>Budget imbalance</i>					
BIM = EFOS+ELUC - (GATM+SOCEAN+SLAND)	20	20	0	20	20

a Using projections for year 2020 (Sect. 3.4). Uncertainties are the same as 1850-2019 period

b Cumulative ELUC 1750-1849 of 30 GtC based on multi-model mean of Pongratz et al. (2009), Shevliakova et al. (2009), Zaehle et al. (2011), Van Minnen et al. (2009). 1850-2019 from mean of H&N (Houghton and Nassikas, 2017) and BLUE (Hansis et al., 2015). 1750-2019 uncertainty is estimated from standard deviation of DGVMs over 1870-2019 scaled by 1750-2019 emissions.

c Cumulative ELUC based on H&N, BLUE, and OSCAR. Uncertainty is estimated from the standard deviation of DGVM estimates

d Cumulative ELUC based on H&N, BLUE, and OSCAR. Uncertainty is formed from the uncertainty in annual ELUC over 1959-2019, which is 0.7 GtC/yr multiplied by length of the time series

e Ocean sink uncertainty from IPCC (Denman et al., 2007)

Table 9. Major known sources of uncertainties in each component of the Global Carbon Budget, defined as input data or processes that have a demonstrated effect of at least ± 0.3 GtC yr⁻¹.

Source of uncertainty	Time scale (years)	Location	Status	Evidence
Fossil CO ₂ emissions (EFOS; Section 2.1)				
energy statistics	annual to decadal	global, but mainly China & major developing countries	see Sect. 2.1	(Korsbakken et al., 2016)
carbon content of coal	annual to decadal	global, but mainly China & major developing countries	see Sect. 2.1	(Liu et al., 2015)
system boundary	annual to decadal	all countries	see Sect. 2.1	
Net land-use change flux (ELUC; section 2.2)				
land-cover and land-use change statistics	continuous	global; in particular tropics	see Sect. 2.2	(Houghton et al., 2012; Gasser et al., 2020)
sub-grid-scale transitions	annual to decadal	global	see Table A1	(Wilkenskjeld et al., 2014)
vegetation biomass	annual to decadal	global; in particular tropics	see Table A1	(Houghton et al., 2012)
wood and crop harvest	annual to decadal	global; SE Asia	see Table A1	(Arneth et al., 2017, Erb et al., 2018)
peat burning (a)	multi-decadal trend	global	see Table A1	(van der Werf et al., 2010)
loss of additional sink capacity	multi-decadal trend	global	not included; Section 2.7.4	(Pongratz et al, 2014, Gasser et al, 2020)
Atmospheric growth rate (GATM; section 2.3) no demonstrated uncertainties larger than ± 0.3 GtC yr ⁻¹ (b)				
Ocean sink (SOCEAN; section 2.4)				
variability in oceanic circulation (c)	semi-decadal to decadal	global	see Sect. 2.4	(DeVries et al., 2017, 2019)

internal variability	annual to decadal	high latitudes; Equatorial Pacific	no ensembles/ coarse resolution	(McKinley et al., 2016)
anthropogenic changes in nutrient supply	multi-decadal trend	global	not included	(Duce et al., 2008)
Land sink (SLAND; section 2.5)				
strength of CO2 fertilisation	multi-decadal trend	global	see Sect. 2.5	(Wenzel et al., 2016)
response to variability in temperature and rainfall	annual to decadal	global; in particular tropics	see Sect. 2.5	(Cox et al., 2013)
nutrient limitation and supply				
response to diffuse radiation	annual	global	see Sect. 2.5	(Mercado et al., 2009)
a As result of interactions between land-use and climate				
b The uncertainties in GATM have been estimated as ± 0.2 GtC yr ⁻¹ , although the conversion of the growth rate into a global annual flux assuming instantaneous mixing throughout the atmosphere introduces additional errors that have not yet been quantified.				
c Could in part be due to uncertainties in atmospheric forcing (Swart et al., 2014)				

Appendix A. Supplementary tables.

Table A1. Comparison of the processes included in the bookkeeping method and DGVMs in their estimates of ELUC and SLAND. See Table 4 for model references. All models include deforestation and forest regrowth after abandonment of agriculture (or from afforestation activities on agricultural land). Processes relevant for ELUC are only described for the DGVMs used with land-cover change in this study (Fig. 6 top panel).

	Bookkeeping Models			DGVMs																
	H&N	BLUE	OSCAR	CABLE-POP	CLASSIC	CLM5.0	DLEM	ISAM	ISBA-CTRIP(h)	JSBACH	JULES-ES	LPJ-GUESS	LPJ	LPX-Berlin	OCN	ORCHIDEEv3	SDGVM	VISIT	YIBs	
Processes relevant for ELUC																				
Wood harvest and forest degradation (a)	yes	yes	yes	yes	no	yes	yes	yes	no	yes	no	yes	yes	no (d)	yes	yes	no	yes	no	
Shifting cultivation / Subgrid scale transitions	no (b)	yes	yes	yes	no	yes	no	no	no	yes	no	yes	yes	no (d)	no	no	no	yes	no	
Cropland harvest (removed, R, or added to litter, L)	yes (R) (z)	yes (R) (z)	yes (R)	yes (R)	yes (L)	yes (R)	yes	yes	yes (R+L)	yes (R+L)	yes (R)	yes (R)	yes (L)	yes (R)	yes (R+L)	yes (R)	yes (R)	yes (R)	no	
Peat fires	yes	yes	yes	no	no	yes	no	no	no	no	no	no	no	no	no	no	no	no	no	
fire as a management tool	yes (z)	yes (z)	yes (j)	no	no	no	no	no	no	no	no	no	no	no	no	no	no	no	no	
N fertilization	yes (z)	yes (z)	yes (j)	no	no	yes	yes	yes	no	no	yes (k)	yes	no	yes	yes	yes	yes	no	no	
tillage	yes (z)	yes (z)	yes (j)	yes	yes (g)	no	no	no	no	no	no	yes	no	no	no	yes (g)	no	no	no	
irrigation	yes (z)	yes (z)	yes (j)	no	no	yes	yes	yes	no	no	no	yes	no	no	no	no	no	no	no	
wetland drainage	yes (z)	yes (z)	yes (j)	no	no	no	no	no	no	no	no	no	no	no	no	no	no	no	no	
erosion	yes (z)	yes (z)	yes (j)	no	no	no	yes	no	no	no	no	no	no	no	no	no	no	yes	no	
peat drainage	yes	yes	yes	no	no	no	no	no	no	no	no	no	no	no	no	no	no	no	no	
Grazing and mowing Harvest (removed, r, or added to litter, l)	yes (r) (z)	yes (r) (z)	yes (r)	yes (r)	no	no	no	yes (l)	no	yes (l)	no	yes (r)	yes (l)	no	yes (r+l)	no	no	no	no	
Processes also relevant for SLAND																				
Fire simulation and/or suppression	for US only	no	yes (m)	no	yes	yes	yes	no	yes	yes	no	yes	yes	yes	no	no	yes	yes	no	
Climate and variability	no	no	yes	yes	yes	yes	yes	yes	yes	yes	yes	yes	yes	yes	yes	yes	yes	yes	yes	
CO2 fertilisation	no (i)	no (i)	yes	yes	yes	yes	yes	yes	yes	yes	yes	yes	yes	yes	yes	yes	yes	yes	yes	

Carbon-nitrogen interactions, including N deposition	no (z)	no (z)	no (j)	yes	no (f)	yes	yes	yes	no (e)	yes	yes	yes	no	yes	yes	yes	yes (c)	no	no
(z) Process captured implicitly by use of observed carbon densities.																			
(a) Refers to the routine harvest of established managed forests rather than pools of harvested products.																			
(b) No back- and forth-transitions between vegetation types at the country-level, but if forest loss based on FRA exceeded agricultural expansion based on FAO, then this amount of area was cleared for cropland and the same amount of area of old croplands abandoned.																			
(c) Limited. Nitrogen uptake is simulated as a function of soil C, and Vcmax is an empirical function of canopy N. Does not consider N deposition.																			
(d) Available but not active.																			
(e) Simple parameterization of nitrogen limitation based on Yin (2002; assessed on FACE experiments)																			
(f) Although C-N cycle interactions are not represented, the model includes a parameterization of down-regulation of photosynthesis as CO2 increases to emulate nutrient constraints (Arora et al., 2009)																			
(g) Tillage is represented over croplands by increased soil carbon decomposition rate and reduced humification of litter to soil carbon.																			
(h) ISBA-CTRIP corresponds to SURFEXv8 in GCB2018																			
(i) Bookkeeping models include the effect of CO2-fertilization as captured by present-day carbon densities, but not as an effect transient in time.																			
(j) as far as the DGVMs that OSCAR is calibrated to include it																			
(k) perfect fertilisation assumed, i.e. crops are not nitrogen limited and the implied fertiliser diagnosed																			
(m) fire intensity responds to climate and CO2, but no fire suppression																			

Table A2. Comparison of the processes and model set up for the Global Ocean Biogeochemistry Models for their estimates of SOCEAN. See Table 4 for model references.

	NEMO-PlankTOM5	NEMO-PISCES (IPSL)	MICOM-HAMOCC (NorESM1-OCv1.2)	MPIOM-HAMOCC 6	CSIRO	FESOM-1.4-REcoM2	NEMO3.6-PISCESv2-gas (CNRM)	MOM6-COBALT (Princeton)	CESM-ETHZ
SPIN-UP procedure									
Initialisation of carbon chemistry	GLODAPv1 corrected for anthropogenic carbon from Sabine et al (2004)	GLODAPv2	GLODAPv1 (preindustrial DIC)	initialization from previous model simulations	GLODAPv1 preindustrial	GLODAPv2 alkalinity and preindustrial DIC	GLODAPv2	GLODAPv2 for Alkalinity and DIC. DIC is corrected to 1959 level for simulation A and corrected to pre-industrial level for simulation B using Khatiwala et al 2009, 2013	GLODAPv2 preindustrial
Preindustrial spin-up prior to 1850	spin-up 1750-1947	spin-up starting in 1836 with 3 loops of JRA55	1000 year spin up	spin-up with ERA20C	800 years	no	long spin-up (> 1000 years)	Other biogeochemical tracers are initialized from a GFDL-ESM2M spin-up (> 1000 years)	spinup 1655-1849

Atmospheric forcing for pre-industrial spin-up	looping NCEP year 1980	JRA55	CORE-I (normal year) forcing	ERA20C	CORE+JRA55	not applicable	NCEP2 repeat year 1948 perpetually	GFDL-ESM2M internal forcing	COREv2 forcing until 1835, three cycles of conditions from 1949-2009. from 1835-1850: JRA forcing
Atmospheric forcing for historical spin-up 1850-1958 for simulation A	1750-1947: looping NCEP year 1980; 1948-2019: NCEP	1836-1958 : looping full JRA55 reanalysis	CORE-I (normal year) forcing; from 1948 onwards NCEP-R1 with CORE-II corrections	NCEP / ERA20C (spin-up)	JRA55do cyclic 1958	JRA55do-v1.3.1 repeat year 1961	NCEP2 repeat year 1948 perpetually	JRA55do-v1.4 repeat year 1959 (81 years)	JRA55 version 1.3, repeat cycle between 1958-2018.
Atmospheric CO2 for historical spin-up 1850-1958 for simulation A	provided by the GCP; converted to pCO2 temperature formulation (Sarmiento et al., JGR 1992), monthly resolution	xCO2 as provided by the GCB, global mean, annual resolution, converted to pCO2 with sea-level pressure and water vapour pressure	xCO2 as provided by the GCB, converted to pCO2 assuming constant standard sea level pressure	provided by the GCB	provided by GCP	xCO2 as provided by the GCB, converted to pCO2 with sea-level pressure and water vapour pressure, global mean, monthly resolution	xCO2 as provided by the GCB, converted to pCO2 with constant sea-level pressure and water vapour pressure, global mean, yearly resolution	xCO2 at year 1959 level (315 ppm), converted to pCO2 with sea-level pressure and water vapour pressure, global mean, yearly resolution	xCO2 as provided by the GCB, converted to pCO2 with atmospheric pressure, and locally determined water vapour pressure from SST and SSS (100% saturation)
Atmospheric forcing for control spin-up 1850-1958 for simulation B	1750-2019: looping NCEP 1980	not available	CORE-I (normal year) forcing	spin-up initial restart file with cyclic 1957 NCEP; run 1957-2017	JRA55do cyclic 1958	JRA55do-v1.3.1 repeat year 1961	NCEP2 repeat year 1948 perpetually	JRA55do-v1.4 repeat year 1959 (81 years)	normal year forcing created from JRA55 version 1.3, NYF = climatology with anomalies from the year 2001
Atmospheric CO2 for control spin-up 1850-1958 for simulation B (ppm)	constant 278ppm; converted to pCO2 temperature formulation	N/A	xCO2 of 278 ppm, converted to pCO2 assuming constant standard sea level	278, no conversion, assuming constant standard sea level pressure	280	xCO2 of 278ppm, converted to pCO2 with sea-level pressure and water	xCO2 of 278ppm, converted to pCO2 with constant sea-level pressure	xCO2 of 278ppm, converted to pCO2 with sea-level pressure and water	xCO2 as provided by the GCB for 1850, converted to pCO2 with

	(Sarmiento et al., JGR 1992), monthly resolution		pressure			vapour pressure	and water vapour pressure	vapour pressure	atmospheric pressure, and locally determined water vapour pressure from SST and SSS (100% saturation)
Simulation A									
Atmospheric forcing for simulation A	NCEP	JRA55	NCEP-R1 with CORE-II corrections	NCEP / NCEP+ERA-20C (spin-up)	JRA55do	JRA55-do-v1.4.0 1958-2018 and JRA55-do-v1.4.0.1b for 2019	NCEP with CORE-II corrections	JRA55-do-v1.4.0 1959-2018 and JRA55-do-v1.4.0.1b for 2019	JRA-55 version 1.3
Atmospheric CO2 for simulation A	provided by the GCP; converted to pCO2 temperature formulation (Sarmiento et al., JGR 1992), monthly resolution	xCO2 as provided by the GCB, global mean, annual resolution, converted to pCO2 with sea-level pressure and water vapour pressure	xCO2 as provided by the GCB, converted to pCO2 assuming constant standard sea level pressure		provided by GCP	xCO2 as provided by the GCB, converted to pCO2 with sea-level pressure and water vapour pressure, global mean, monthly resolution	xCO2 as provided by the GCB, converted to pCO2 with constant sea-level pressure and water vapour pressure, global mean, yearly resolution	xCO2 as provided by the GCB, converted to pCO2 with sea-level pressure and water vapour pressure, global mean, yearly resolution	xCO2 as provided by the GCB, converted to pCO2 with atmospheric pressure, and locally determined water vapour pressure from SST and SSS (100% saturation)
Simulation B									
Atmospheric forcing for simulation B	NCEP 1980	N/A	CORE-I (normal year) forcing	spin-up initial restart file (278) with cyclic 1957 NCEP; run 1957-2017 with 278	JRA55do cyclic 1958	JRA55-do-v1.3.1 repeat year 1961	NCEP with CORE-II corrections cycling over 1948-1957	JRA55-do-v1.4.0 repeat year 1959	normal year forcing created from JRA-55 version 1.3, NYF = climatology with anomalies from the year 2001

Atmospheric CO2 for simulation B	constant 278ppm; converted to pCO2 temperature formulation (Sarmiento et al., JGR 1992), monthly resolution	N/A	xCO2 of 278 ppm, converted to pCO2 assuming constant standard seal level pressure		280	xCO2 of 278ppm, converted to pCO2with sea-level pressure and water vapour pressure	xCO2 of 278ppm, converted to pCO2 with constant sea-level pressure and water vapour pressure	xCO2 of 278ppm, converted to pCO2 with sea-level pressure and water vapour pressure	xCO2 as provided by the GCB for 1850, converted to pCO2 with atmospheric pressure, and locally determined water vapour pressure from SST and SSS (100% saturation)
Model specifics									
Physical ocean model	NEMOv2.3-ORCA2	NEMOv3.6-eORCA1L75	MICOM (NorESM1-OCv1.2)	MPIOM	MOM5	FESOM-1.4	NEMOv3.6-GELATOV6-eORCA1L75	MOM6-SIS2	CESMv1.4 (ocean model based on POP2)
Biogeochemistry model	PlankTOM5.3	PISCESv2	HAMOCC (NorESM1-OCv1.2)	HAMOCC6	WOMBAT	REcoM-2	PISCESv2-gas	COBALTv2	BEC (modified & extended)
Horizontal resolution	2o lon, 0.3 to 1.5o lat	1° lon, 0.3 to 1° lat	1° lon, 0.17 to 0.25 lat (nominally 1°)	1.5°	1o x1o with enhanced resolution at the tropics and in the high lat Southern Ocean	unstructured multi-resolution mesh. CORE-mesh, with 20-120 km resolution. Highest resolution north of 50N, intermediate in the equatorial belt and Southern Ocean, lowest in the subtropical gyres	1° lon, 0.3 to 1° lat	0.5° lon, 0.25 to 0.5° lat	Lon: 1.125°, Lat varying from 0.53° in the extratropics to 0.27° near the equator
Vertical resolution	31 levels	75 levels, 1m at the surface	51 isopycnic layers + 2 layers representing a bulk mixed layer	40 levels, layer thickness increase with depth	50 levels, 20 in the 200m	46 levels, 10 m spacing in the top 100 m	75 levels, 1m at surface	75 levels hybrid coordinates, 2 m at surface	60 levels (z-coordinates)
Total ocean area	3.6080E+	3.6270E+	3.6006E+	3.6598E+	3.6134E+	3.6475E+	3.6270E+	3.6110E+	3.5926E+

on native grid (km2)	08	08	08	08	08	08	08	08	08
Gas-exchange parameterization	Quadratic exchange formulation (function of $T + 0.3 \cdot U^2$) * $(Sc/660)^{-0.5}$; Wanninkh of et al. 1992 (Equation 8)	see Orr et al 2017: kw parameterized from Wanninkh of 1992, with $kw = a \cdot (Sc/660)^{-0.5} \cdot u^2 \cdot (1 - f_{ice})$ with a from Wanninkh of et al 2014	see Orr et al 2017: kw parameterized from Wanninkh of 1992, with $kw = a \cdot (Sc/660)^{-0.5} \cdot u^2 \cdot (1 - f_{ice})$ with $a=0.337$ following the OCMIP2 protocols	Gas transfer velocity formulation and parameter setup of Wanninkh of (2014), including updated Schmidt number parameterizations for CO2 to comply with OMIP protocol (Orr et al., 2017)	Quadratic exchange formulation (function of $T + 0.3 \cdot U^2$) * $(Sc/660)^{-0.5}$; Wanninkh of et al. 1992 (Equation 8)	see Orr et al 2017: kw parameterized from Wanninkh of 1992, with $kw = a \cdot (Sc/660)^{-0.5} \cdot u^2 \cdot (1 - f_{ice})$ with a from Wanninkh of et al 2014	see Orr et al 2017: kw parameterized from Wanninkh of 1992, with $kw = a \cdot (Sc/660)^{-0.5} \cdot u^2 \cdot (1 - f_{ice})$ with a from Wanninkh of et al 2014	see Orr et al 2017: kw parameterized from Wanninkh of 1992, with $kw = a \cdot (Sc/660)^{-0.5} \cdot u^2 \cdot (1 - f_{ice})$ with a from Wanninkh of et al 2014	Gas exchange is parameterized using the Wanninkh of (1992) quadratic wind speed dependency formulation, but with the coefficient scaled down to reflect the recent 14C inventories. Concretely, we used a coefficient a of 0:31 cm hr ⁻¹ s ² m ⁻² to read $kw = 0:31 \text{ ws}^2 (1-f_{ice}) (Sc=660)^{-1/2}$
Time-step	96 mins	45 min	3200 sec	60 mins	15 min	15 min	15min	30 min	3757 sec
Output frequency	Monthly	monthly	monthly/daily	monthly	monthly	monthly	monthly	monthly	monthly
CO2 chemistry routines	Following Broecker et al. (1982)	mocsy	Following Dickson et al. (2007)	as in Ilyina et al. (2013) adapted to comply with OMIP protocol (Orr et al., 2017).	OCMIP2 (Orr et al.)	mocsy	mocsy	mocsy	OCMIP2 (Orr et al.)
River carbon input (GtC/yr)	60.24 Tmol/yr; 0.723 GtC/yr	0.61 GtC y-1	0	none	0	0	~0.6 GtC y-1	~0.11 GtC y-1	0.33 Gt C yr-1
Burial/net flux into the sediment (GtC/yr)	0.723 GtC/yr	0.59 GtC y-1		around 0.4 GtC/yr	0	0	~0.7 GtC y-1	~0.21 GtC y-1	0.25 Gt C yr-1

Table A3: Description of ocean data-products used for assessment of SOCEAN. See Table 4 for references.

data-products	Jena-MLS	MPI-SOMFFN	CMEMS	CSIR	Watson et al
Method	<p>Spatio-temporal interpolation (update of Rödenbeck et al., 2013, version oc_v2020). Specifically, the sea-air CO₂ fluxes and the pCO₂ field are numerically linked to each other and to the spatio-temporal field of ocean-internal carbon sources/sinks through process parametrizations, and the ocean-internal sources/sink field is then fit to the SOCATv2020 pCO₂ data (Bakker et al. 2020). The fit includes a multi-linear regression against environmental drivers to bridge data gaps, and interannually explicit corrections to represent the data signals more completely.</p>	<p>2-step neural network method where in a first step the global ocean is clustered into 16 biogeochemical provinces using a self-organizing map (SOM). In a second step, the non-linear relationship between available pCO₂ measurements from the SOCAT database (Bakker et al 2016) and environmental predictor data (SST, SSS, MLD, CHL-a, atmospheric CO₂ - references see Landschützer et al 2016) are established using a feed-forward neural network (FFN) for each province separately. The established relationship is then used to fill the existing data gaps (see Landschützer et al 2013, Landschützer et al 2016).</p>	<p>An ensemble of neural network models trained on 100 subsampled datasets from the Surface Ocean CO₂ Atlas (SOCAT, Bakker et al 2016) . Like the original data, subsamples are distributed after interpolation on 1x1 grid cells along ship tracks. Sea surface salinity, temperature, sea surface height, mixed layer depth, atmospheric CO₂ mole fraction, chlorophyll, spco2 climatology, latitude and longitude are used as predictors. The models are used to reconstruct sea surface pCO₂, and then convert to air-sea CO₂ fluxes.</p>	<p>An ensemble average of six machine learning estimates of pCO₂ using the approach described in Gregor et al. (2019) with the updated product using SOCAT v2020. All ensemble members use a cluster-regression approach. Two different cluster configurations are used: 1) based on K-means clustering; 2) Fay and McKinley (2014) 's CO₂ biomes. Three regression algorithms are used: 1) gradient boosted decision trees, 2) feed-forward neural network, 3) support vector regression. The product of the cluster configurations and the regression algorithms results in an ensemble with six members.</p>	<p>Derived from the the SOCAT(v2020) pCO₂ database, but corrected to the subskin temperature of the ocean as measured by satellite, using the methodology described by Goddijn-Murphy et al (2015). A correction to the flux calculation is also applied for the cool and salty surface skin. In other respects the product uses interpolation of the data using the two step neural network based on MPI-SOMFFN :in the first step the ocean is divided into a monthly climatology of 16 biogeochemical provinces using a SOM, In the second step a feed-forward neural network establishes non-linear relationships between pCO₂ and SST, SSS, mixed layer depth(MLD) and atmospheric xCO₂ in each of the 16 provinces. Further description in Watson et al (2020).</p>
Gas-exchange parameterization	<p>Quadratic exchange formulation ($k \cdot U^{2 \cdot (Sc/660)^{-0.5}}$) (Wanninkhof 1992) with the transfer coefficient k scaled to match a global mean transfer rate of 16 cm/hr by Naegler (2009)</p>	<p>Quadratic exchange formulation ($k \cdot U^{2 \cdot (Sc/660)^{-0.5}}$) (Wanninkhof 1992) with the transfer coefficient k scaled to match a global mean transfer rate of 16 cm/hr (calculated myself over the full period 1982-2019 - not following Naegler)</p>	<p>Quadratic exchange formulation ($k \cdot U^{2 \cdot (Sc/660)^{-0.5}}$) (Wanninkhof et al. 2014) with the transfer coefficient k scaled to match a global mean transfer rate of 16 cm/hr by Naegler (2009)</p>	<p>Quadratic exchange formulation ($k \cdot U^{2 \cdot (Sc/660)^{-0.5}}$) (Wanninkhof 1992) with the transfer coefficient k scaled to match a global mean transfer rate of 16 cm/hr by Naegler (2009)</p>	<p>Nightingale et al. (2000) formulation : $K = ((Sc/600)^{-0.5}) \cdot (0.333 \cdot U + 0.222 \cdot U^2)$</p>

Wind product	NCEP reanalysis (Kalnay et al., 1996)	ERA 5	ERA5	ERA5	CCMP wind product, 0.25 x 0.25 degrees x 6-hourly, from which we calculate mean and mean square winds over 1 x 1 degree and 1 month intervals. CCMP product does not cover years 1985-1987, for which we use a monthly climatology calculated as the means of 1988-1991.
Spatial resolution	2.5 degrees longitude * 2 degrees latitude	1x1 degree	1x1 degree	1x1 degree	1x1 degree
Temporal resolution	daily	monthly	monthly	monthly	monthly
Atmospheric CO2	spatially and temporally varying field based on atmospheric CO2 data from 156 stations (Jena CarboScope atmospheric inversion sEXTALL_v2020)	atmospheric pCO2_wet calculated from the NOAA ESRL marine boundary layer xCO2 and the NCEP sea level pressure with the moisture correction by Dickson et al 2007 (details and references can be obtained from Appendix A3 in Landschützer et al 2013)	Spatially and monthly varying fields of atmospheric pCO2 computed from CO2 mole fraction (Chevallier, 2013), and atmospheric dry-air pressure which is derived from monthly surface pressure (ERA5) and water vapour pressure fitted by Weiss and Price (1980)	Mole fraction of CO2 from NOAA marine boundary layer product interpolated longitudinally onto ERA5 monthly mean sea level pressure (MSLP). A water vapour pressure correction is applied to MSLP using the equation from Dickson et al. (2007).	Atmospheric pCO2 (wet) calculated from NOAA marine boundary layer XCO2 and NCEP sea level pressure, with pH2O calculated from Cooper et al, 1998. (2019 XCO2 marine boundary values were not available at submission so we used preliminary values, estimated from 2018 values and increase at Mauna Loa.)
Total ocean area on native grid (km2)	3.63E+08	3.21E+08	3.21E+08	3.35E+08	3.48E+08

Table A4. Comparison of the inversion set up and input fields for the atmospheric inversions. Atmospheric inversions see the full CO₂ fluxes, including the anthropogenic and pre-industrial fluxes. Hence they need to be adjusted for the pre-industrial flux of CO₂ from the land to the ocean that is part of the natural carbon cycle before they can be compared with SOCEAN and SLAND from process models. See Table 4 for references.

	CarbonTracker Europe (CTE)	Jena CarboScope	Copernicus Atmosphere Monitoring Service (CAMS)	UoE	MIROC	NISMO N-CO ₂
Version number	CTE2020	sEXTocNEET_v2020	v19r1	in-situ	4	
Observations						
Atmospheric observations	Hourly resolution (well-mixed conditions) obspack GLOBALVIEWplus v5.0 and NRT_v5.2 (a)	Flasks and hourly (outliers removed by 2-sigma criterion)	Daily averages of well-mixed conditions - OBSPACK GLOBALVIEWplus v5.0& NRT v5.2, WDCGG, RAMCES and ICOS ATC	Hourly resolution (well-mixed conditions) obspack GLOBALVIEW plus v5.0 and NRT_v 5.2 (a)	34 surface sites from obspack GLOBALVIEW plus v5.0 and NRT_v 5.2 (a)	Hourly resolution (well-mixed conditions) obspack GLOBALVIEW plus v5.0 and NRT_v 5.2 (a) + NIES observations
Prior fluxes						
Biosphere and fires	SIBCASA biosphere (b) with 2019 climatological, GFAS fires	No prior	ORCHIDEE (climatological), GFEDv4.1 & GFAS after 2019	CASA v1.0, climatology after 2016 & GFED4.0	CASA	VISIT & GFEDv 4.1s
Ocean	oc_v1.7 (Rodenbeck et al., 2014) with updates, 2019 climatology + anomalies from oc_v2020	oc_v2020 (Rodenbeck et al., 2014) with updates	CMEMS Copernicus ocean fluxes (Denvil-Sommer et al., 2019), with updates	Takahashi climatology	Takahashi climatology	JMA global ocean mapping (Iida et al., 2015)

Fossil fuels	GridFED v2020 (Jones et al., 2020)	GridFED v2020 (Jones et al., 2020)	GridFED v2020 (Jones et al., 2020)	ODIAC v2016, after 2015 constant	GridFE D v2020 (Jones et al., 2020)	GridFE D v2020 (Jones et al., 2020)
Transport and optimization						
Transport model	TM5	TM3	LMDZ v6	GEOS- CHEM	ACTM	NICAM -TM
Weather forcing	ECMWF	NCEP	ECMWF	MERRA 2	JRA55	JRA55
Horizontal Resolution	Global: 3° x 2°, Europe: 1° x 1°, North America: 1° x 1°	Global: 4° x 5°	Global: 3.75° x 1.875°	Global: 4° x 5°	Global: 2.8° x 2.8°	isocahedral gl5: ~225k mx225 km
Optimization	Ensemble Kalman filter	Conjugate gradient (re-orthonormalization) (c)	Variational	Ensemble Kalman filter	Matrix inversion with 84 big regions	Variational
a (GLOBALVIEW, 2020; Carbontracker Team, 2020)						
b (van der Velde et al., 2014)						
c ocean prior not optimised						

Table A5 Attribution of fCO₂ measurements for the year 2019 included in SOCATv2020 (Bakker et al., 2016, 2020) to inform ocean pCO₂-based flux products.

Platform	Regions	No. of samples	Principal Investigators	No. of data sets	Platform type
<i>Allure of the Seas</i>	Tropical Atlantic	110103	Wanninkhof, R.; Pierrot, D.	46	Ship
<i>Atlantic Condor</i>	North Atlantic	5051	Wallace, D.; Atamanchuk, D.	1	Ship
<i>Atlantic Explorer</i>	North Atlantic	24534	Bates, N. R.	19	Ship
<i>Aurora Australis</i>	Southern Ocean	24269	Tilbrook, B.	2	Ship
<i>Bell M. Shimada</i>	North Pacific	20176	Alin, S.; Feely, R. A.	6	Ship
<i>Bjarni Saemundsson</i>	North Atlantic	17364	Benoit-Cattin, A.; Ólafsdóttir, S. R.	3	Ship
<i>Bluefin</i>	North Pacific, tropical Pacific	40110	Alin, S. R.; Feely, R. A.	6	Ship
<i>Cap San Lorenzo</i>	North Atlantic, tropical Atlantic	17496	Lefèvre, N.	4	Ship
CB-06_125W_43N	North Pacific	223	Sutton, A.; Hales, B.	1	Mooring
<i>Colibri</i>	North Atlantic; tropical Atlantic	27823	Lefèvre, N.	5	Ship
<i>Columbia</i>	North Pacific	76458	Evans, W.; Lebon, G. T.; Harrington, C. D.; Bidlack, A.	1	Ship
<i>Discovery</i>	North Atlantic	1457	Kitidis, V.	1	Ship
<i>Equinox</i>	Tropical Atlantic	84273	Wanninkhof, R.; Pierrot, D.	41	Ship
<i>Finnmaid</i>	North Atlantic	144037	Rehder, G.; Glockzin, M.; Bittig, H. C.	3	Ship
<i>Flora</i>	North Atlantic, tropical Atlantic, tropical Pacific	58550	Wanninkhof, R.; Pierrot, D.	21	Ship
<i>G.O. Sars</i>	North Atlantic	93203	Skjelvan, I.	11	Ship
<i>Gordon Gunter</i>	North Atlantic	48162	Wanninkhof, R.; Pierrot, D.	9	Ship
<i>Gulf Challenger</i>	North Atlantic	6072	Salisbury, J.; Vandemark, D.; Hunt, C.	6	Ship
<i>Healy</i>	North Pacific, Arctic	28988	Takahashi, T.; Sweeney, C.; Newberger, T.; Sutherland S. C.; Munro, D. R.	2	Ship
<i>Henry B. Bigelow</i>	North Atlantic	66186	Wanninkhof, R.; Pierrot, D.	12	Ship
<i>Investigator</i>	Indian Ocean, South Pacific, Southern Ocean	126943	Tilbrook, B.	7	Ship
<i>James Clark Ross</i>	North Atlantic, Southern Ocean	10305	Kitidis, V.	3	Ship
<i>Keifu Maru II</i>	North Pacific, Tropical Pacific	8935	Kadono, K.	6	Ship
<i>Laurence M. Gould</i>	Southern Ocean	38380	Sweeney, C.; Takahashi, T.; Newberger, T.; Sutherland, S. C.;	4	Ship

			Munro, D. R.		
<i>Malizia</i>	North Atlantic	88495	Landschützer, P.; Tanhua, T.	3	Ship
<i>Marion Dufresne</i>	Indian, Southern oceans	9107	Lo Monaco, C.; Metzl, N.; Tribollet, A.	2	Ship
<i>New Century 2</i>	North Pacific, tropical Pacific, North Atlantic	28434	Nakaoka, S.-I.	13	Ship
<i>Newrest - Art and Fenêtres</i>	North Atlantic, tropical Atlantic	37651	Tanhua, T.; Landschützer, P.	2	Ship
<i>Nuka Arctica</i>	North Atlantic	65462	Becker, M.; Olsen, A.	20	Ship
<i>Oscar Dyson</i>	North Pacific	30373	Alin, S.; Feely, R. A.	6	Ship
<i>R/V Sikuliaq</i>	North Pacific, Arctic	68540	Takahashi, T.; Sweeney, C.; Newberger, T.; Sutherland, S. C.; Munro, D. R.	11	Ship
<i>Ronald H. Brown</i>	North Atlantic, tropical Atlantic	25605	Wanninkhof, R.; Pierrot, D.	4	Ship
<i>RVIB Nathaniel B. Palmer</i>	Southern Ocean	22759	Takahashi, T.; Sweeney, C.; Newberger, T.; Sutherland, S. C.; Munro D. R.	2	Ship
<i>Ryofu Maru III</i>	North Pacific, tropical Pacific	9981	Kadono, K.	6	Ship
<i>Simon Stevin</i>	North Atlantic	26389	Gkritzalis, T.	6	Ship
<i>Tangaroa</i>	Southern Ocean	34	Currie, K. I.	2	Ship
TAO110W_0N	Tropical Pacific	180	Sutton, A.	1	Mooring
<i>Thomas G. Thompson</i>	North Atlantic, tropical Atlantic, South Atlantic, Southern Ocean	28965	Alin, S.; Feely, R. A.	3	Ship
<i>Trans Carrier</i>	North Atlantic	10767	Omar, A.	1	Ship
<i>Trans Future 5</i>	North Pacific, tropical Pacific, South Pacific,	16694	Nakaoka, S.-I.; Nojiri, Y.	16	Ship
<i>Wakataka Maru</i>	North Pacific	69661	Tadokoro, K.; Ono, T.	4	Ship
Waveglider1741	South Pacific	2287	Sutton, A.	1	ASV

Table A6. Aircraft measurement programs archived by Cooperative Global Atmospheric Data Integration Project (CGADIP, 2019) that contribute to the evaluation of the atmospheric inversions (Figure B3).

Site code	Measurement program name in Obspack	Specific doi	Data providers
AAO	Airborne Aerosol Observatory, Bondville, Illinois		Sweeney, C.; Dlugokencky, E.J.
ACG	Alaska Coast Guard		Sweeney, C.; McKain, K.; Karion, A.; Dlugokencky, E.J.
ALF	Alta Floresta		Gatti, L.V.; Gloor, E.; Miller, J.B.;
AOA	Aircraft Observation of Atmospheric trace gases by JMA		ghg_obs@met.kishou.go.jp
ACT	Atmospheric Carbon and Transport - America		Sweeney, C.; Dlugokencky, E.J.; Baier, B; Montzka, S.; Davis, K.
BNE	Beaver Crossing, Nebraska		Sweeney, C.; Dlugokencky, E.J.
BGI	Bradgate, Iowa		Sweeney, C.; Dlugokencky, E.J.
CAR	Briggsdale, Colorado		Sweeney, C.; Dlugokencky, E.J.
CMA	Cape May, New Jersey		Sweeney, C.; Dlugokencky, E.J.
CON	CONTRAIL (Comprehensive Observation Network for TRace gases by AirLiner)	http://dx.doi.org/10.17595/20180208.001	Machida, T.; Matsueda, H.; Sawa, Y. Niwa, Y.
CRV	Carbon in Arctic Reservoirs Vulnerability Experiment (CARVE)		Sweeney, C.; Karion, A.; Miller, J.B.; Miller, C.E.; Dlugokencky, E.J.
DND	Dahlen, North Dakota		Sweeney, C.; Dlugokencky, E.J.
ESP	Estevan Point, British Columbia		Sweeney, C.; Dlugokencky, E.J.
ETL	East Trout Lake, Saskatchewan		Sweeney, C.; Dlugokencky, E.J.
FWI	Fairchild, Wisconsin		Sweeney, C.; Dlugokencky, E.J.
GSFC	NASA Goddard Space Flight Center Aircraft Campaign		Kawa, S.R.; Abshire, J.B.; Riris, H.
HAA	Molokai Island, Hawaii		Sweeney, C.; Dlugokencky, E.J.
HFM	Harvard University Aircraft Campaign		Wofsy, S.C.
HIL	Homer, Illinois		Sweeney, C.; Dlugokencky, E.J.
HIP	HIPPO (HIAPER Pole-to-Pole Observations)	https://doi.org/10.3334/CDIAC/HIPPO_010	Wofsy, S.C.; Stephens, B.B.; Elkins, J.W.; Hints, E.J.; Moore, F.
INX	INFLUX (Indianapolis Flux Experiment)		Sweeney, C.; Dlugokencky, E.J.; Shepson, P.B.; Turnbull, J.
LEF	Park Falls, Wisconsin		Sweeney, C.; Dlugokencky, E.J.
NHA	Offshore Portsmouth, New Hampshire (Isles of Shoals)		Sweeney, C.; Dlugokencky, E.J.
OIL	Oglesby, Illinois		Sweeney, C.; Dlugokencky, E.J.
PFA	Poker Flat, Alaska		Sweeney, C.; Dlugokencky, E.J.
RBA-B	Rio Branco		Gatti, L.V.; Gloor, E.; Miller, J.B.

RTA	Rarotonga		Sweeney, C.; Dlugokencky, E.J.
SCA	Charleston, South Carolina		Sweeney, C.; Dlugokencky, E.J.
SGP	Southern Great Plains, Oklahoma		Sweeney, C.; Dlugokencky, E.J.; Biraud, S.
TAB	Tabatinga		Gatti, L.V.; Gloor, E.; Miller, J.B.
THD	Trinidad Head, California		Sweeney, C.; Dlugokencky, E.J.
TGC	Offshore Corpus Christi, Texas		Sweeney, C.; Dlugokencky, E.J.
WBI	West Branch, Iowa		Sweeney, C.; Dlugokencky, E.J.

Table A7. Main methodological changes in the global carbon budget since first publication. Methodological changes introduced in one year are kept for the following years unless noted. Empty cells mean there were no methodological changes introduced that year.

Publication year	Fossil fuel emissions			LUC emissions	Reservoirs			Uncertainty & other changes
	Global	Country (territorial)	Country (consumption)		Atmosphere	Ocean	Land	
2006 (a)		Split in regions						
2007 (b)				ELUC based on FAO-FRA 2005; constant ELUC for 2006	1959-1979 data from Mauna Loa; data after 1980 from global average	Based on one ocean model tuned to reproduced observed 1990s sink		$\pm 1\sigma$ provided for all components
2008 (c)				Constant ELUC for 2007				
2009 (d)		Split between Annex B and non-Annex B	Results from an independent study discussed	Fire-based emission anomalies used for 2006-2008		Based on four ocean models normalised to observations with constant delta	First use of five DGVMs to compare with budget residual	
2010 (e)	Projection for current year based on GDP	Emissions for top emitters		ELUC updated with FAO-FRA 2010				
2011 (f)			Split between Annex B and non-Annex B					

2012 (g)		129 countries from 1959	129 countries and regions from 1990-2010 based on GTAP8.0	ELUC for 1997-2011 includes interannual anomalies from fire-based emissions	All years from global average	Based on 5 ocean models normalised to observations with ratio	Ten DGVMs available for SLAND; First use of four models to compare with ELUC	
2013 (h)		250 countries b	134 countries and regions 1990-2011 based on GTAP8.1, with detailed estimates for years 1997, 2001, 2004, and 2007	ELUC for 2012 estimated from 2001-2010 average		Based on six models compared with two data-products to year 2011	Coordinated DGVM experiments for SLAND and ELUC	Confidence levels; cumulative emissions; budget from 1750
2014 (i)	Three years of BP data	Three years of BP data	Extended to 2012 with updated GDP data	ELUC for 1997-2013 includes interannual anomalies from fire-based emissions		Based on seven models	Based on ten models	Inclusion of breakdown of the sinks in three latitude bands and comparison with three atmospheric inversions

2015 (j)	Projection for current year based Jan-Aug data	National emissions from UNFCCC extended to 2014 also provided	Detailed estimates introduced for 2011 based on GTAP9			Based on eight models	Based on ten models with assessment of minimum realism	The decadal uncertainty for the DGVM ensemble mean now uses $\pm 1\sigma$ of the decadal spread across models
a Raupach et al. (2007)								
b Canadell et al. (2007)								
c Online								
d Le Quéré et al. (2009)								
e Friedlingstein et al. (2010)								
f Peters et al. (2012b)								
g Le Quéré et al. (2013), Peters et al. (2013)								
h Le Quéré et al. (2014)								
i Le Quéré et al. (2015b)								
j Le Quéré et al. (2016)								

Table A8 Relative changes in fossil CO2 emissions (EFOS) for the year 2020 to date and projections for the full year. Methods of the four approaches are described in Section 2.1.5 and Appendix C.

2020 Year to Date fossil emissions										
	UEA	Priestley	Carbon Monitor	GCB		Media n	Avera ge	Min	Max	Range
China (August)	-4.6	-10.8	-2.4			-4.6	-5.9	-10.8	-2.4	8.4
USA (August)	-12.3	-16.8	-13.3	-12.0		-12.8	-13.6	-16.8	-12.0	4.8
EU27 (June)	-10.0	-15.4	-12.6	-16.8		-14.0	-13.7	-16.8	-10.0	6.7
India (August)	-13.7	-21.5	-13.7	-13.5		-13.7	-15.6	-21.5	-13.5	8.0
RoW (August)	-7.6	-14.3	-8.8			-8.8	-10.2	-14.3	-7.6	6.7
World (August)	-8.0	-14.3	-8.1			-8.1	-10.1	-14.3	-8.0	6.3
2020 projection of fossil emissions										
	UEA	Priestley	Carbon Monitor	GCB		Media n	Avera ge	Min	Max	Range
China	-3.1	-9.0	0.1	1.4		-1.5	-2.6	-9.0	1.4	10.3
USA	-8.8	-15.4	-12.7	-10.3		-11.5	-11.8	-15.4	-8.8	6.7
EU27	-6.1	-12.3	-8.4	-16.9		-10.4	-10.9	-16.9	-6.1	10.8
India	-9.4	-19.6	-10.5	-11.4		-11.0	-12.7	-19.6	-9.4	10.2
Rest of the World	-5.5	-12.9	-8.2	-6.5		-7.3	-8.3	-12.9	-5.5	7.4
World	-5.6	-12.7	-6.6	-6.0		-6.3	-7.7	-12.7	-5.6	7.1

Table A9. Funder and grant number (where relevant)	Author Initials
Australia, Integrated Marine Observing System (IMOS)	BT
Australian Government as part of the Antarctic Science Collaboration Initiative program	AL
Australian Government National Environment Science Program (NESP)	JGC, VH
Belgium Research Foundation – Flanders (FWO) (grant number UA C130206-18)	TG
BNP Paribas Foundation through Climate & Biodiversity initiative, philanthropic grant for developments of the Global Carbon Atlas	PC
China, National Natural Science Foundation (grant no. 41975155)	XY
China, National Natural Science Foundation (grant no. 71874097 and 41921005) and Beijing Natural Science Foundation (JQ19032)	ZL
EC Copernicus Atmosphere Monitoring Service implemented by ECMWF on behalf of the European Commission	FC
EC Copernicus Marine Environment Monitoring Service implemented by Mercator Ocean	MG
EC H2020 (4C; grant no 821003)	PF, RMA, SS, GPP, MOS, JIK, SL, NG, PL, TI
EC H2020 (CHE; grant no 776186)	LF
EC H2020 (CRESCENDO: grant no. 641816)	RS, EJ, AJPS, TI
EC H2020 (CONSTRAIN: grant no 820829)	RS, PMF
EC H2020 European Research Council (ERC) Synergy grant (IMBALANCE-P; grant no. ERC-2013-SyG-610028)	TG
EC H2020 (QUINCY; grant no 647204)	SZ
EC H2020 project (VERIFY: grant no. 776810)	CLQ, GPP, JIK, RMA, MWJ, PC, NV
European Space Agency Climate Change Initiative ESA-CCI RECCAP2 project 655 (ESRIN/4000123002/18/I-NB)	PF, PC, SS, MOS
French Institut National des Sciences de l'Univers (INSU) and Institut Pau- Emile Victor (IPEV), Sorbonne Universités (OSU Ecce-Terra), TAAF (Terres Australes et Antarctique Françaises), Museum National d'Histoire Naturelle (MNHN)	NM
French Institut de Recherche pour le Développement (IRD)	NL, NM
German Integrated Carbon Observation System (ICOS), Federal Ministry for Education and Research (BMBF); BONUS INTEGRAL (BONUS Blue Ocean and Federal Ministry of Education and Research Grant No. 03F0773A)	HCB
German Helmholtz Association in its ATMO programme and the state Baden-Württemberg, Germany, through bwHPC	AA
German Helmholtz Young Investigator Group Marine Carbon and Ecosystem Feedbacks in the Earth System (MarESys), grant number VH-NG-1301	JH
German Research Foundation's Emmy Noether Programme (grant no. PO1751/1-1)	JP
German Stifterverband für die Deutsche Wissenschaft e.V. in collaboration with Volkswagen AG	SB
Icelandic Ministry for the Environment and Natural Resources	ABC
Japan Global Environmental Research Coordination System, Ministry of the Environment (grant number E1751)	SN, TO
Japan Environment Research and Technology Development Fund of the Ministry of the Environment (JPMEERF20142001 and JPMEERF20172001)	YN, NC

Japan Meteorological Agency (JMA)	KK
Kuehne + Nagel	TT
Monaco Fondation Prince Albert II de Monaco (www.fpa2.org)	NM, TT
Monaco, Yacht Club de Monaco	TT
Norwegian Research Council (grant no. 270061)	JS
Norwegian ICOS Norway and OTC Research Infrastructure Project, Research Council of Norway (grant number 245927)	MB, IS, AO
Swiss National Science Foundation (grant no. 200020_172476)	SL
UK Natural Environment Research Council (SONATA: grant no. NE/P021417/1)	DRW
UK Natural Environment Research Council (NE/R015953/1; NE/N018095/1)	VK
UK Natural Environmental Research Council (NE/R016518/1)	PIP
UK Newton Fund, Met Office Climate Science for Service Partnership Brazil (CSSP Brazil)	AW, ER
UK Royal Society: The European Space Agency OCEANFLUX projects	AJW
USA Department of Agriculture, National Institute of Food and Agriculture (grants no. 2015-67003-23489 and 2015-67003-23485)	DLL
USA Department of Commerce, NOAA/OAR's Global Ocean Monitoring and Observation Program	RW, AS, SA, DP, NRB, DRM
USA Department of Commerce, NOAA/OAR's Ocean Acidification Program	RW, SA, AIS, DP
USA Department of Energy, Office of Science and BER prg. (grant no. DE-SC000 0016323)	AKJ
USA Department of Energy, SciDac award number is DESC0012972; IDS grant award number is 80NSSC17K0348	LC, GH
USA NASA Interdisciplinary Research in Earth Science Program.	BP
US National Science Foundation (grant number 1903722)	HT
USA Princeton University Environmental Institute and the NASA OCO2 science team, grant number 80NSSC18K0893.	LR
ORNL is managed by UT-Battelle, LLC, for the US DOE under contract DE-AC05-00OR22725.	APW
Computing resources	
Norway UNINETT Sigma2, National Infrastructure for High Performance Computing and Data Storage in Norway (NN2980K/NS2980K)	JS
The supercomputer systems of NIES (SX-Aurora) and MRI (FUJITSU Server PRIMERGY CX2550M5)	YN
MIROC4-ACTM inversion is run from JAMSTEC Super Computer system in coordination with Prabir Patra	NC
Japan National Institute for Environmental Studies computational resources	EK
TGCC under allocation 2019-A0070102201 made by GENCI	FC
UEA High Performance Computing Cluster, UK	DRW, CLQ
Supercomputing time was provided by the Météo-France/DSI supercomputing center.	RS, EJ
CarbonTracker Europe was supported by the Netherlands Organization for Scientific Research (NWO; grant no. SH-312, 17616)	WP
Deutsches Klimarechenzentrum (allocation bm0891)	JEMSN, JP
The Leibniz Supercomputing Centre provided computing time on its Linux-Cluster	KH
PRACE for awarding access to JOLIOT CURIE at GENCI@CEA, France	LB

<p>The CESM project is supported primarily by the National Science Foundation (NSF). This material is based upon work supported by the National Center for Atmospheric Research, which is a major facility sponsored by the NSF under Cooperative Agreement No. 1852977. Computing and data storage resources, including the Cheyenne supercomputer (doi:10.5065/D6RX99HX), were provided by the Computational and Information Systems Laboratory (CISL) at NCAR. We thank all the scientists, software engineers, and administrators who contributed to the development of CESM2.</p>	DLL
--	-----

Figure Captions

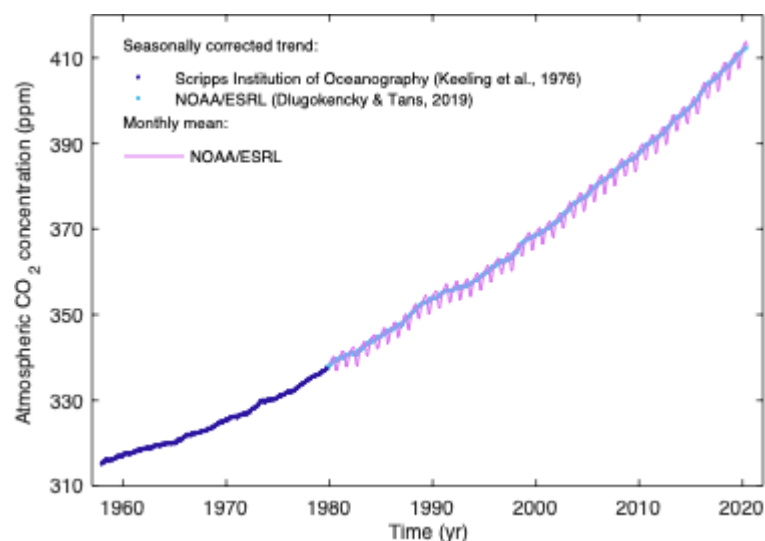


Figure 1. Surface average atmospheric CO₂ concentration (ppm). The 1980-2019 monthly data are from NOAA/ESRL (Dlugokencky and Tans, 2020) and are based on an average of direct atmospheric CO₂ measurements from multiple stations in the marine boundary layer (Masarie and Tans, 1995). The 1958-1979 monthly data are from the Scripps Institution of Oceanography, based on an average of direct atmospheric CO₂ measurements from the Mauna Loa and South Pole stations (Keeling et al., 1976). To take into account the difference of mean CO₂ and seasonality between the NOAA/ESRL and the Scripps station networks used here, the Scripps surface average (from two stations) was deseasonalised and harmonised to match the NOAA/ESRL surface average (from multiple stations) by adding the mean difference of 0.542 ppm, calculated here from overlapping data during 1980-2012.

The global carbon cycle

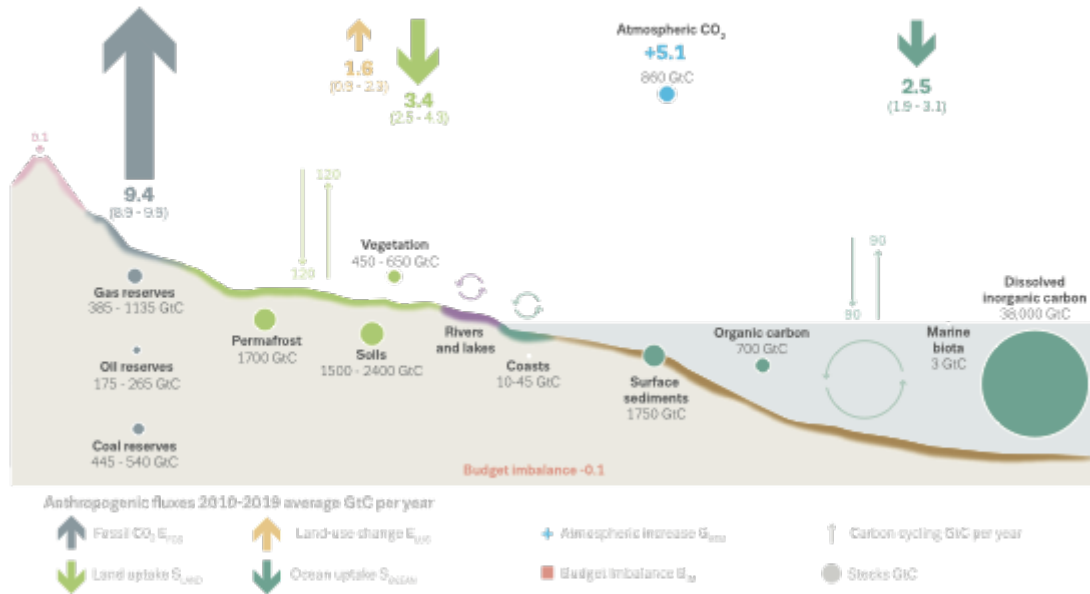


Figure 2. Schematic representation of the overall perturbation of the global carbon cycle caused by anthropogenic activities, averaged globally for the decade 2009-2019. See legends for the corresponding arrows and units. The uncertainty in the atmospheric CO₂ growth rate is very small (± 0.02 Gt C yr⁻¹) and is neglected for the figure. The anthropogenic perturbation occurs on top of an active carbon cycle, with fluxes and stocks represented in the background and taken from Ciais et al. (2013) for all numbers, with the ocean gross fluxes updated to 90 GtC yr⁻¹ to account for the increase in atmospheric CO₂ since publication, and except for the carbon stocks in coasts which is from a literature review of coastal marine sediments (Price and Warren, 2016).

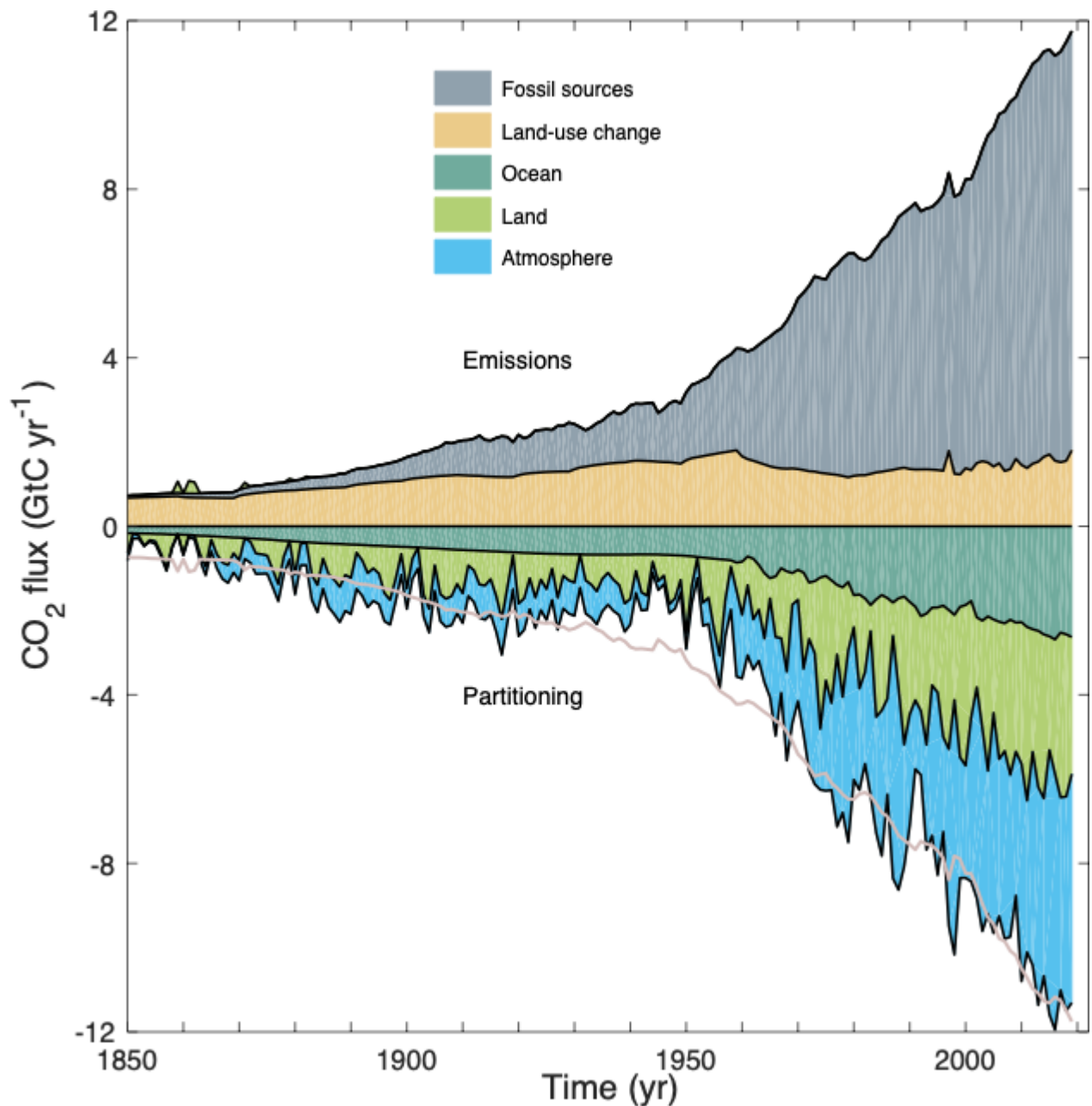


Figure 3. Combined components of the global carbon budget illustrated in Fig. 2 as a function of time, for fossil CO₂ emissions (E_{FOS} , including a small sink from cement carbonation; grey) and emissions from land-use change (E_{LUC} ; brown), as well as their partitioning among the atmosphere (G_{ATM} ; blue), ocean (S_{OCEAN} ; turquoise), and land (S_{LAND} ; green). The partitioning is based on nearly independent estimates from observations (for G_{ATM}) and from process model ensembles constrained by data (for S_{OCEAN} and S_{LAND}), and does not exactly add up to the sum of the emissions, resulting in a budget imbalance which is represented by the difference between the bottom pink line (reflecting total emissions) and the sum of the ocean, land and atmosphere. All time series are in GtC yr^{-1} . G_{ATM} and S_{OCEAN} prior to 1959 are based on different

methods. E_{FOS} are primarily from (Gilfillan et al. 2020), with uncertainty of about $\pm 5\%$ ($\pm 1\sigma$); E_{LUC} are from two bookkeeping models (Table 2) with uncertainties of about $\pm 50\%$; G_{ATM} prior to 1959 is from Joos and Spahni (2008) with uncertainties equivalent to about $\pm 0.1-0.15 \text{ GtC yr}^{-1}$, and from Dlugokencky and Tans (2020) from 1959 with uncertainties of about $\pm 0.2 \text{ GtC yr}^{-1}$; S_{OCEAN} prior to 1959 is averaged from Khatiwala et al. (2013) and DeVries (2014) with uncertainty of about $\pm 30\%$, and from a multi-model mean (Table 4) from 1959 with uncertainties of about $\pm 0.5 \text{ GtC yr}^{-1}$; S_{LAND} is a multi-model mean (Table 4) with uncertainties of about $\pm 0.9 \text{ GtC yr}^{-1}$. See the text for more details of each component and their uncertainties.

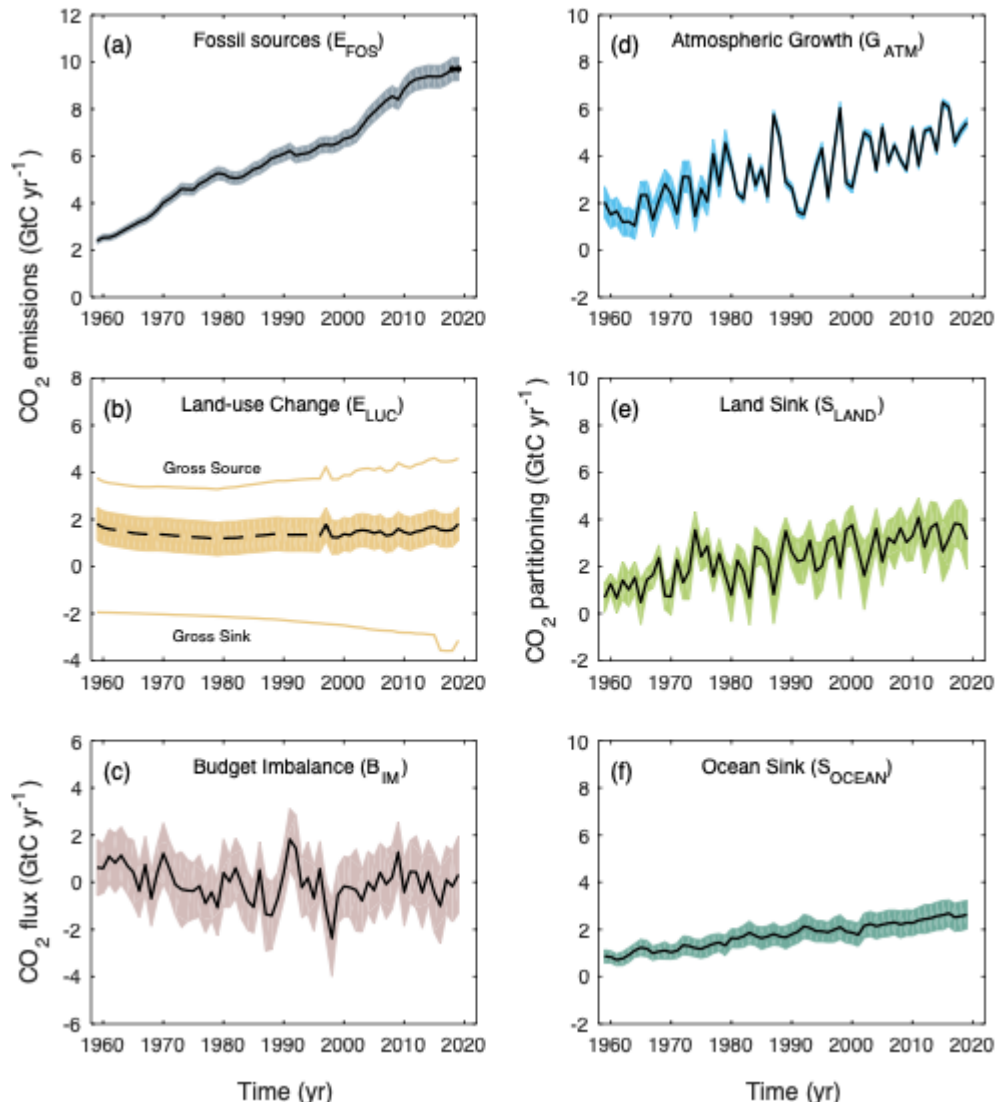


Figure 4. Components of the global carbon budget and their uncertainties as a function of time, presented individually for **(a)** fossil CO₂ emissions (E_{FOS}), **(b)** emissions from land-use change (E_{LUC}), **(c)** the budget imbalance that is not accounted for by the other terms, **(d)** growth rate in atmospheric CO₂ concentration (G_{ATM}), and **(e)** the land CO₂ sink (S_{LAND} , positive indicates a flux from the atmosphere to the land), **(f)** the ocean CO₂ sink (S_{OCEAN} , positive indicates a flux from the atmosphere to the ocean). All time series are in GtC yr⁻¹ with the uncertainty bounds representing $\pm 1\sigma$ in shaded colour. Data sources are as in Fig. 3. The black dots in **(a)** show values for 2018-2019 that originate from a different data set to the remainder of the data (see text). The dashed line in **(b)** identifies the pre-satellite period before the inclusion of emissions from peatland burning.

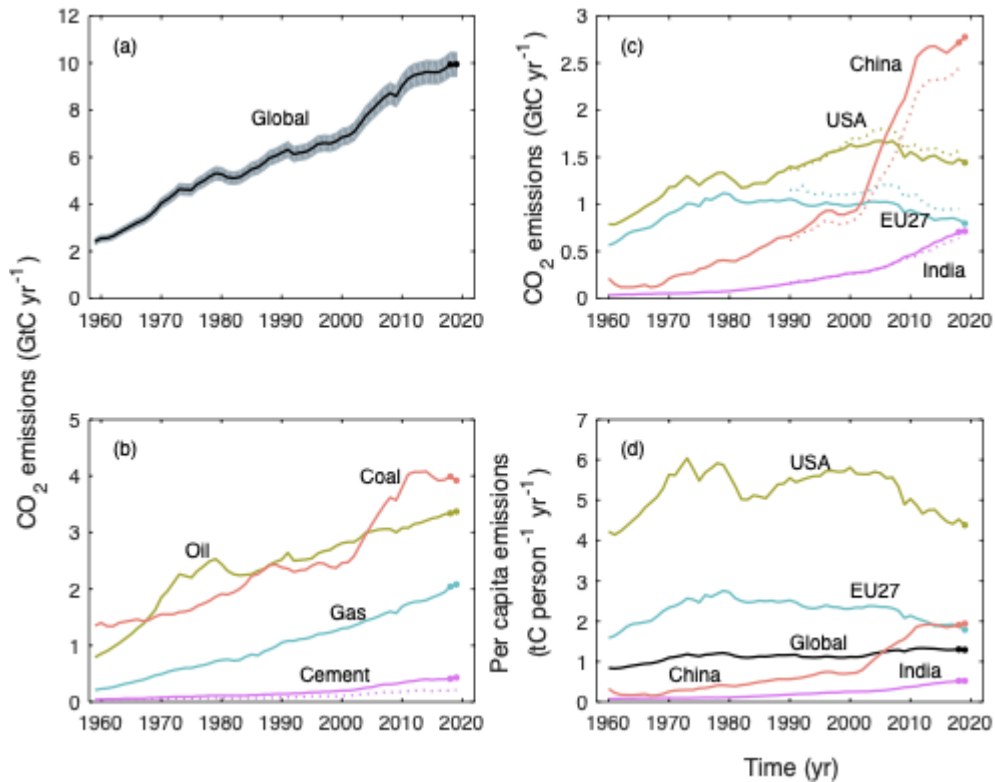


Figure 5. Fossil CO₂ emissions for **(a)** the globe, including an uncertainty of $\pm 5\%$ (grey shading), and the emissions extrapolated using BP energy statistics (black dots), **(b)** global emissions by fuel type, including coal (salmon), oil (olive), gas (turquoise), cement (purple), and cement carbonation (dotted purple), and excluding gas flaring which is small (0.6% in 2013), **(c)** territorial (solid lines) and consumption (dashed lines) emissions for the top three country emitters (USA - olive; China - salmon; India - purple) and for the European Union (EU; turquoise for the 27 member states of the EU as of 2020), and **(d)** per-capita emissions for the top three country emitters and the EU (all colours as in panel **(c)**) and the world (black). In **(b-c)**, the dots show the data that were extrapolated from BP energy statistics for 2018-2019. All time series are in GtC yr⁻¹ except the per-capita emissions **(d)**, which are in tonnes of carbon per person per year (tC person⁻¹ yr⁻¹). Territorial emissions are primarily from Gilfillan et al. (2020) except national data for the USA and EU27 (the 27 member states of the EU) for 1990-2018, which are reported by the countries to the UNFCCC as detailed in the text; consumption-based emissions are updated from Peters et al. (2011a). See Section 2.1.1 for details of the calculations and data sources.

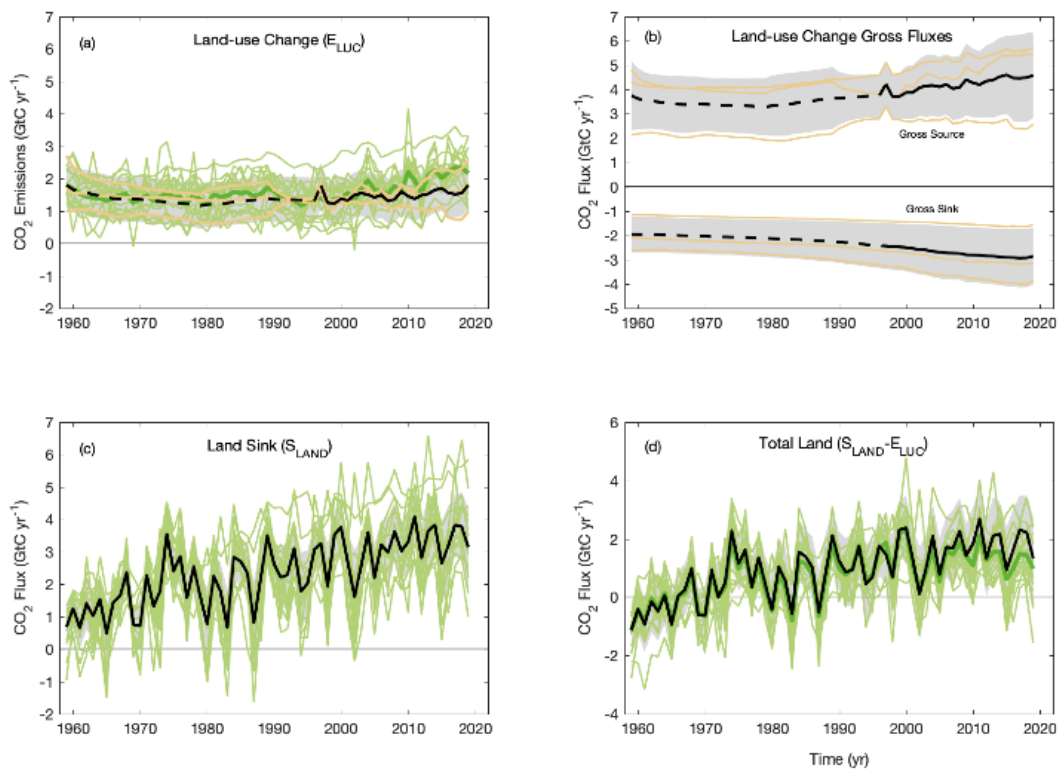


Figure 6. CO₂ exchanges between the atmosphere and the terrestrial biosphere as used in the global carbon budget (black with $\pm 1\sigma$ uncertainty in grey shading), for **(a)** CO₂ emissions from land-use change (E_{LUC}), showing also individually the three bookkeeping models (three brown lines) and the DGVM model results (green) and their multi-model mean (dark green). The dashed line identifies the pre-satellite period before the inclusion of peatland burning; **(b)** Land CO₂ sink (S_{LAND}) with individual DGVMs (green); **(c)** Total land CO₂ fluxes (**b minus a**) with individual DGVMs (green) and their multi-model mean (dark green).

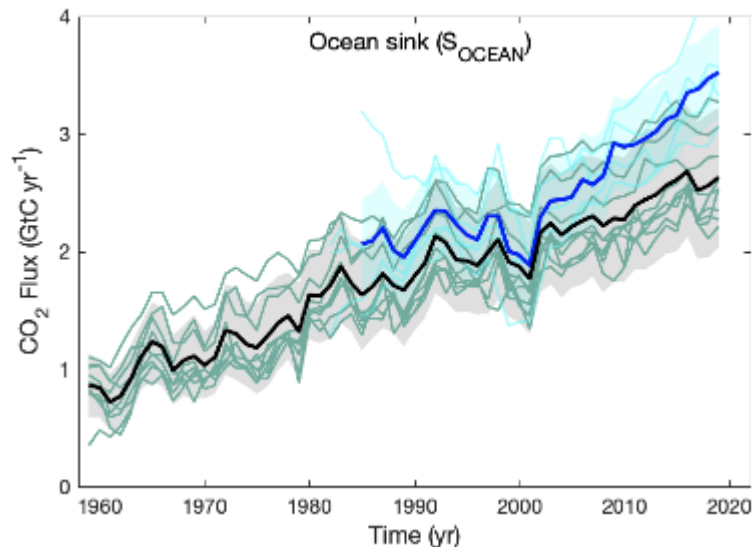


Figure 7. Comparison of the anthropogenic atmosphere-ocean CO₂ flux showing the budget values of S_{OCEAN} (black; with $\pm 1\sigma$ uncertainty in grey shading), individual ocean models (teal), and the five ocean pCO₂-based flux products (ensemble mean in dark blue; with $\pm 1\sigma$ uncertainty in light blue shading see Table 4, individual products in cyan). The pCO₂-based flux products were adjusted for the pre-industrial ocean source of CO₂ from river input to the ocean, which is not present in the ocean models, by adding a sink of 0.61 GtC yr⁻¹ to make them comparable to S_{OCEAN} (see Section 2.7.3).

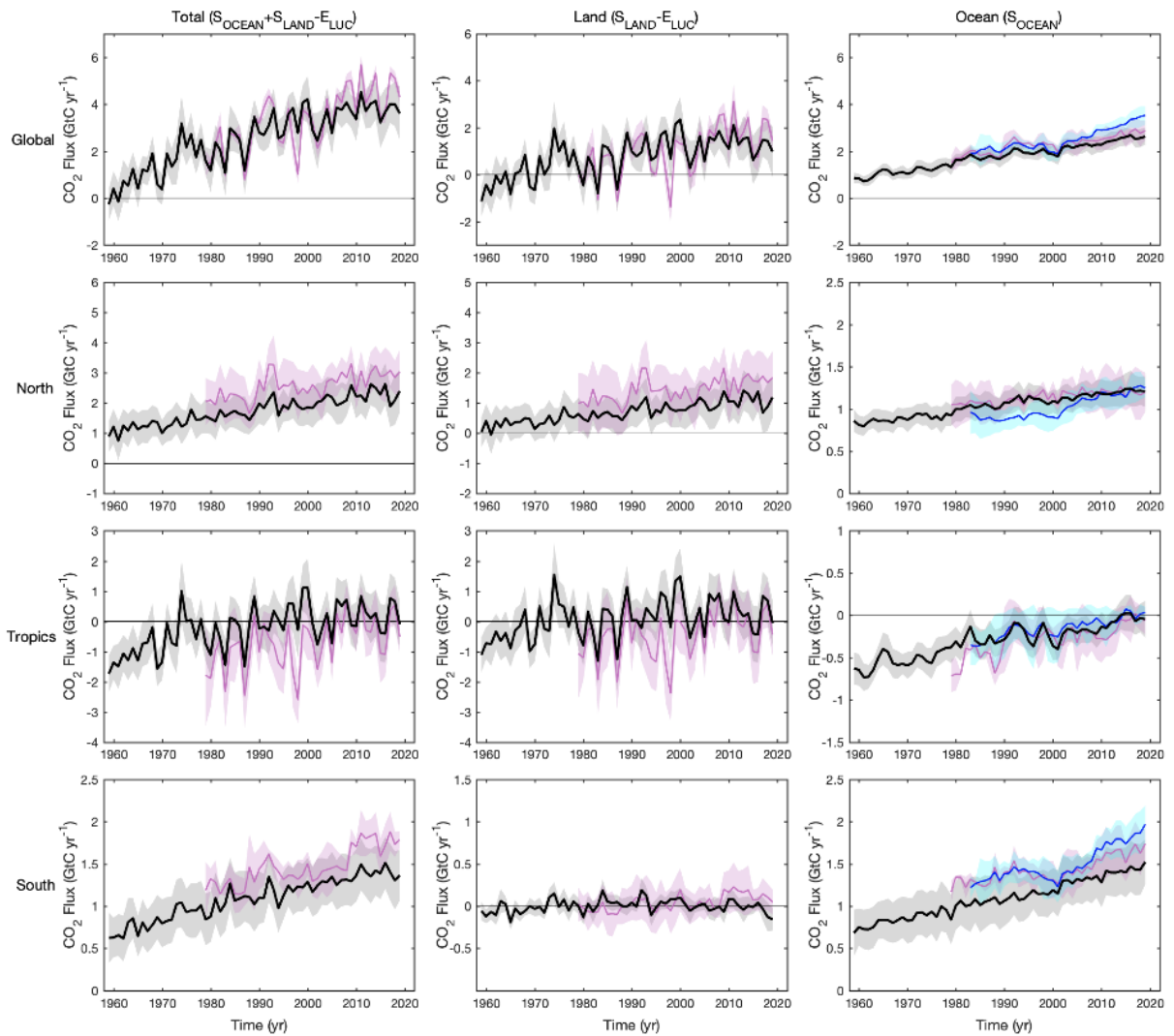


Figure 8. CO₂ fluxes between the atmosphere and the surface, S_{OCEAN} and $(S_{\text{LAND}} - E_{\text{LUC}})$ by latitude bands for the (top) globe, (2nd row) north (north of 30°N), (3rd row) tropics (30°S-30°N), and (bottom) south (south of 30°S), and over (left) total ($S_{\text{OCEAN}} + S_{\text{LAND}} - E_{\text{LUC}}$), (middle) land only ($S_{\text{LAND}} - E_{\text{LUC}}$) and (right) ocean only (S_{OCEAN}). Positive values indicate a flux from the atmosphere to the land and/or ocean. Mean estimates from the combination of the process models for the land and oceans are shown (black line) with $\pm 1\sigma$ of the model ensemble (grey shading). For total uncertainty, the land and ocean uncertainties are summed in quadrature. Mean estimates from the atmospheric inversions are shown (pink lines) with their $\pm 1\sigma$ spread (pink shading). Mean estimates from the pCO₂-based flux products are shown for the ocean

domain (dark blue lines) with their $\pm 1\sigma$ spread (light blue shading). The global S_{OCEAN} (upper right) and the sum of S_{OCEAN} in all three regions represents the anthropogenic atmosphere-to-ocean flux based on the assumption that the preindustrial ocean sink was 0 GtC yr^{-1} when riverine fluxes are not considered. This assumption does not hold on the regional level, where preindustrial fluxes can be significantly different from zero. Hence, the regional panels for S_{OCEAN} represent a combination of natural and anthropogenic fluxes. Bias-correction and area-weighting were only applied to global S_{OCEAN} , hence the sum of the regions is slightly different from the global estimate ($<0.05 \text{ GtC yr}^{-1}$).

Anthropogenic carbon flows

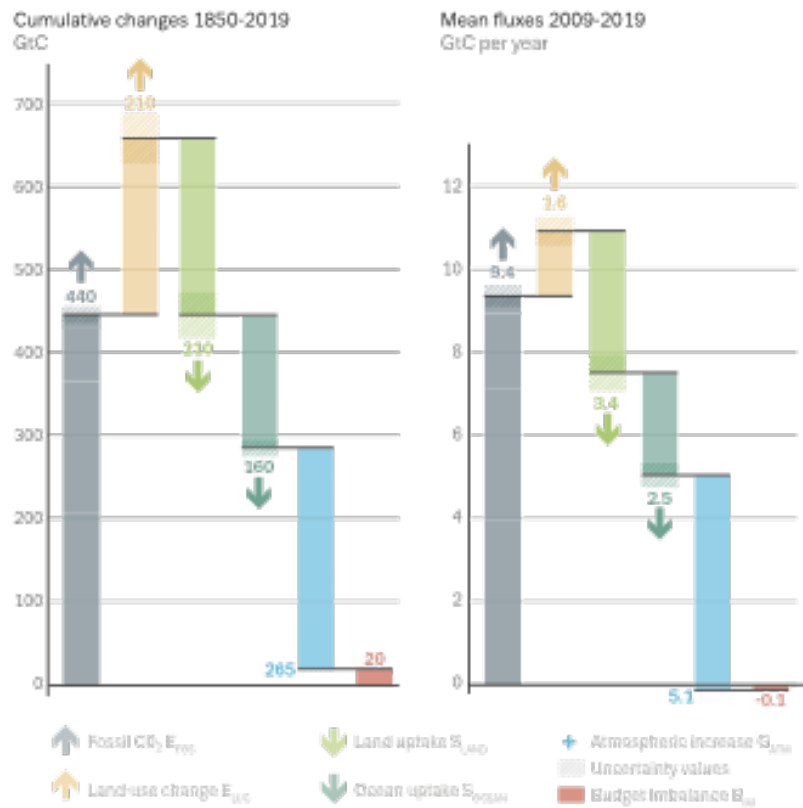


Figure 9. Cumulative changes during 1850-2018 and mean fluxes during 2009-2018 for the anthropogenic perturbation as defined in the legend.

Appendix B. Supplementary figures.

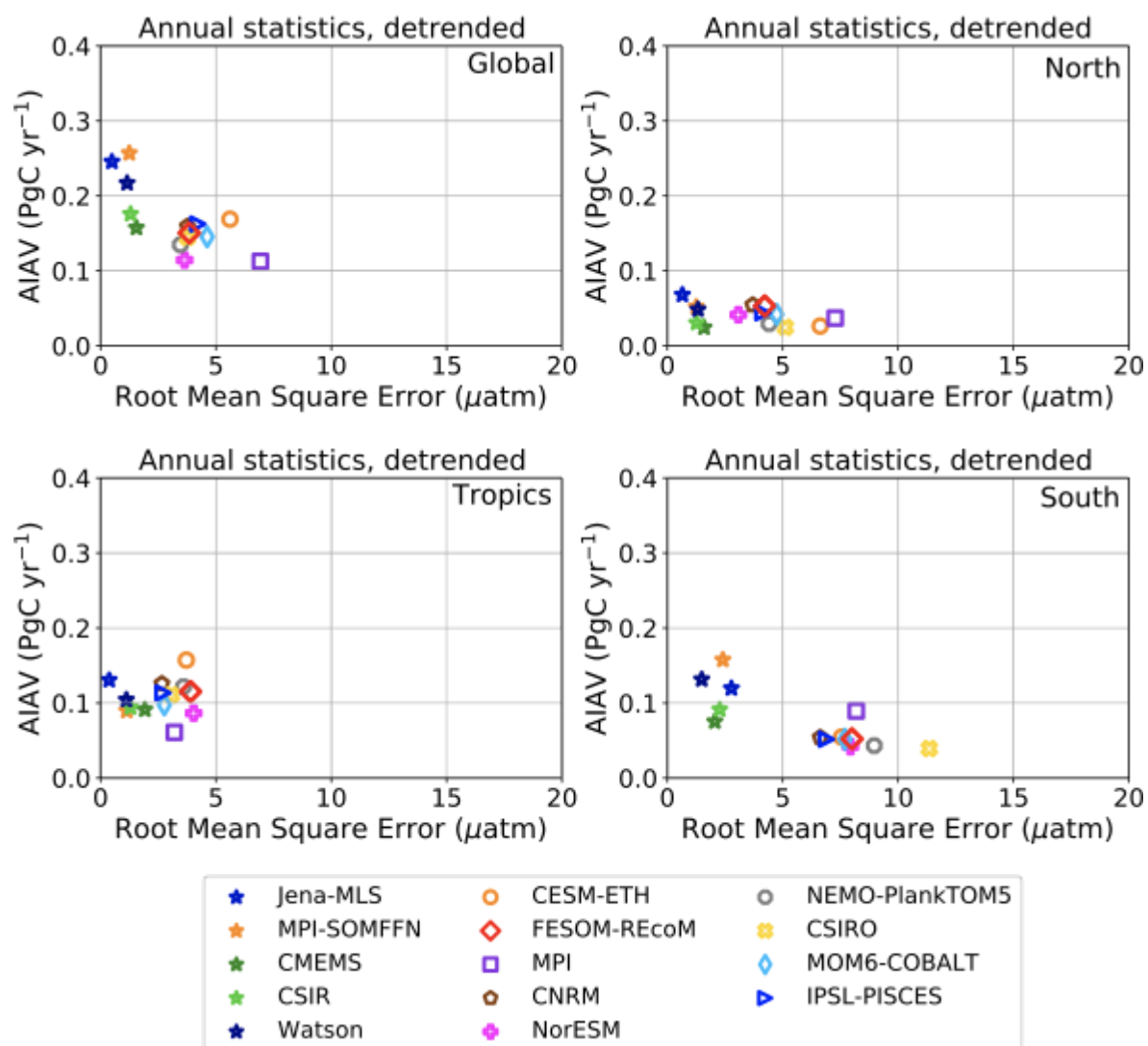


Figure B1. Evaluation of the GOBMs and flux products using the root mean squared error (RMSE) for the period 1985 to 2019, between the individual surface ocean pCO₂ estimates and the SOCAT v2020 database. The y-axis shows the amplitude of the interannual variability (AIAV, taken as the standard deviation of a detrended time-series calculated as a 12-months running mean over the monthly flux time-series, Rödenbeck et al., 2015). Results are presented for the globe, north (>30°N), tropics (30°S-30°N), and south (<30°S) for the GOBMs (see legend circles) and for the pCO₂-based flux products (star symbols). The five pCO₂-based flux products use the SOCAT database and therefore are not fully independent from the data (see section 2.4.1).

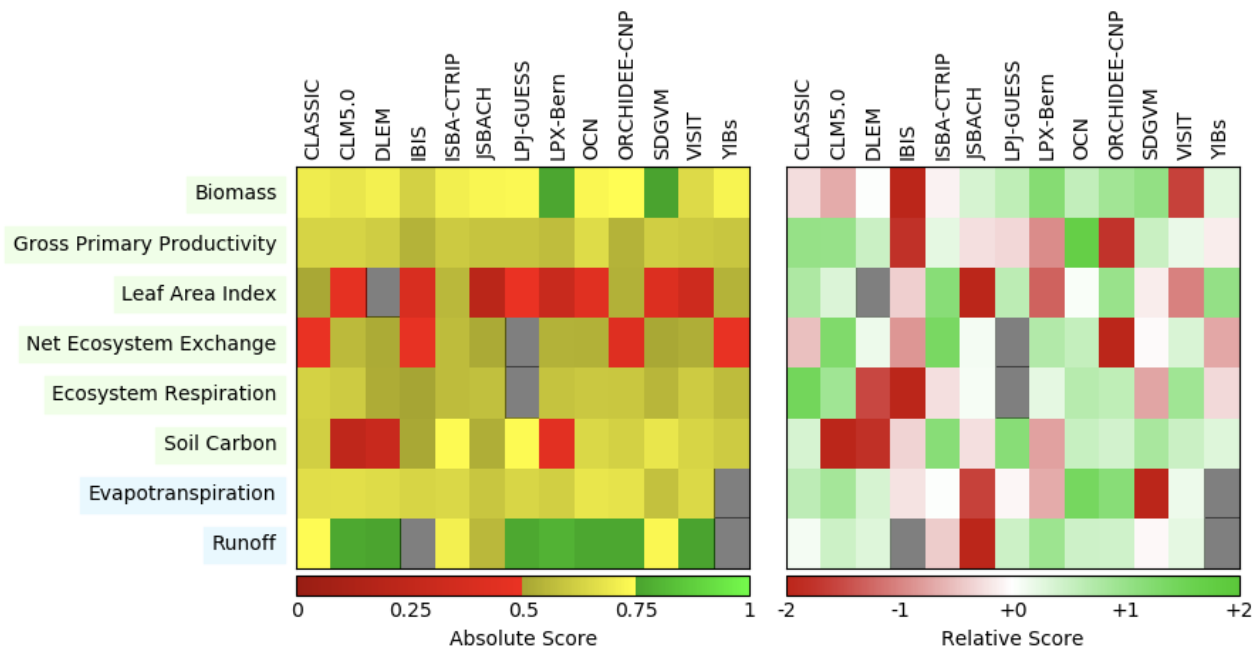


Figure B2. Evaluation of the DGVM using the International Land Model Benchmarking system (ILAMB; Collier et al., 2018) (left) absolute skill scores and (right) skill scores relative to other models. The benchmarking is done with observations for vegetation biomass (Saatchi et al., 2011; and GlobalCarbon unpublished data; Avitabile et al., 2016), GPP (Jung et al., 2010; Lasslop et al., 2010), leaf area index (De Kauwe et al., 2011; Myneni et al., 1997), net ecosystem exchange (Jung et al., 2010; Lasslop et al., 2010), ecosystem respiration (Jung et al., 2010; Lasslop et al., 2010), soil carbon (Hugelius et al., 2013; Todd-Brown et al., 2013), evapotranspiration (De Kauwe et al., 2011), and runoff (Dai and Trenberth, 2002). For each model-observation comparison a series of error metrics are calculated, scores are then calculated as an exponential function of each error metric, finally for each variable the multiple scores from different metrics and observational data sets are combined to give the overall variable scores shown in the left panel. Overall variable scores increase from 0 to 1 with improvements in model performance. The set of error metrics vary with data set and can include metrics based on the period mean, bias, root mean squared error, spatial distribution, interannual variability and seasonal cycle. The relative skill score shown in the right panel is a Z-score, which indicates in units of standard deviation the model scores relative to the multi-model mean score for a given variable. Grey boxes represent missing model data.

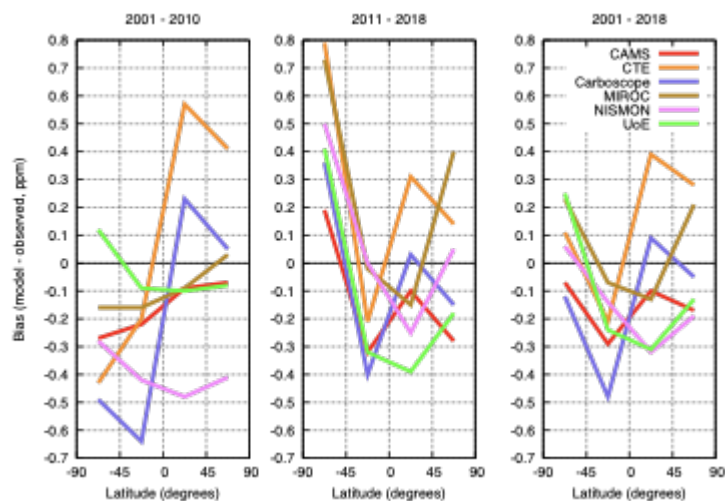


Figure B3. Evaluation of the atmospheric inversion products. The mean of the model minus observations is shown for four latitude bands in three periods: (left) 2001-2010, (centre) 2011-2018, (right) 2001-2018. The four models are compared to independent CO₂ measurements made onboard aircraft over many places of the world between 2 and 7 km above sea level. Aircraft measurements archived in the Cooperative Global Atmospheric Data Integration Project (CGADIP, 2020) from sites, campaigns or programs that cover at least 9 months between 2001 and 2018 and that have not been assimilated, have been used to compute the biases of the differences in four 45° latitude bins. Land and ocean data are used without distinction.

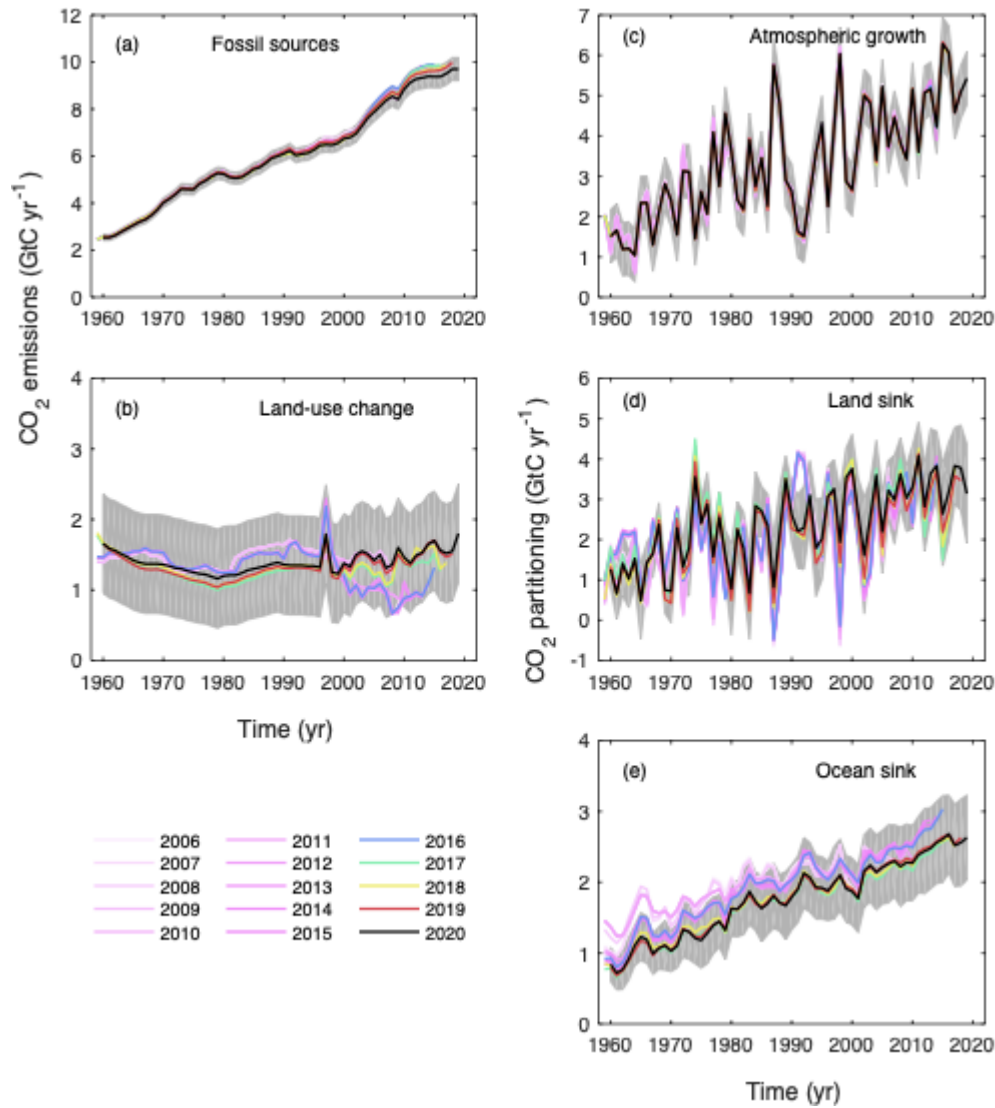


Figure B4. Comparison of global carbon budget components released annually by GCP since 2006. CO₂ emissions from **(a)** fossil CO₂ emissions (E_{FOS}), and **(b)** land-use change (E_{LUC}), as well as their partitioning among **(c)** the atmosphere (G_{ATM}), **(d)** the land (S_{LAND}), and **(e)** the ocean (S_{OCEAN}). See legend for the corresponding years, and Tables 3 and A7 for references. The budget year corresponds to the year when the budget was first released. All values are in GtC yr⁻¹. Grey shading shows the uncertainty bounds representing ±1σ of the current global carbon budget.

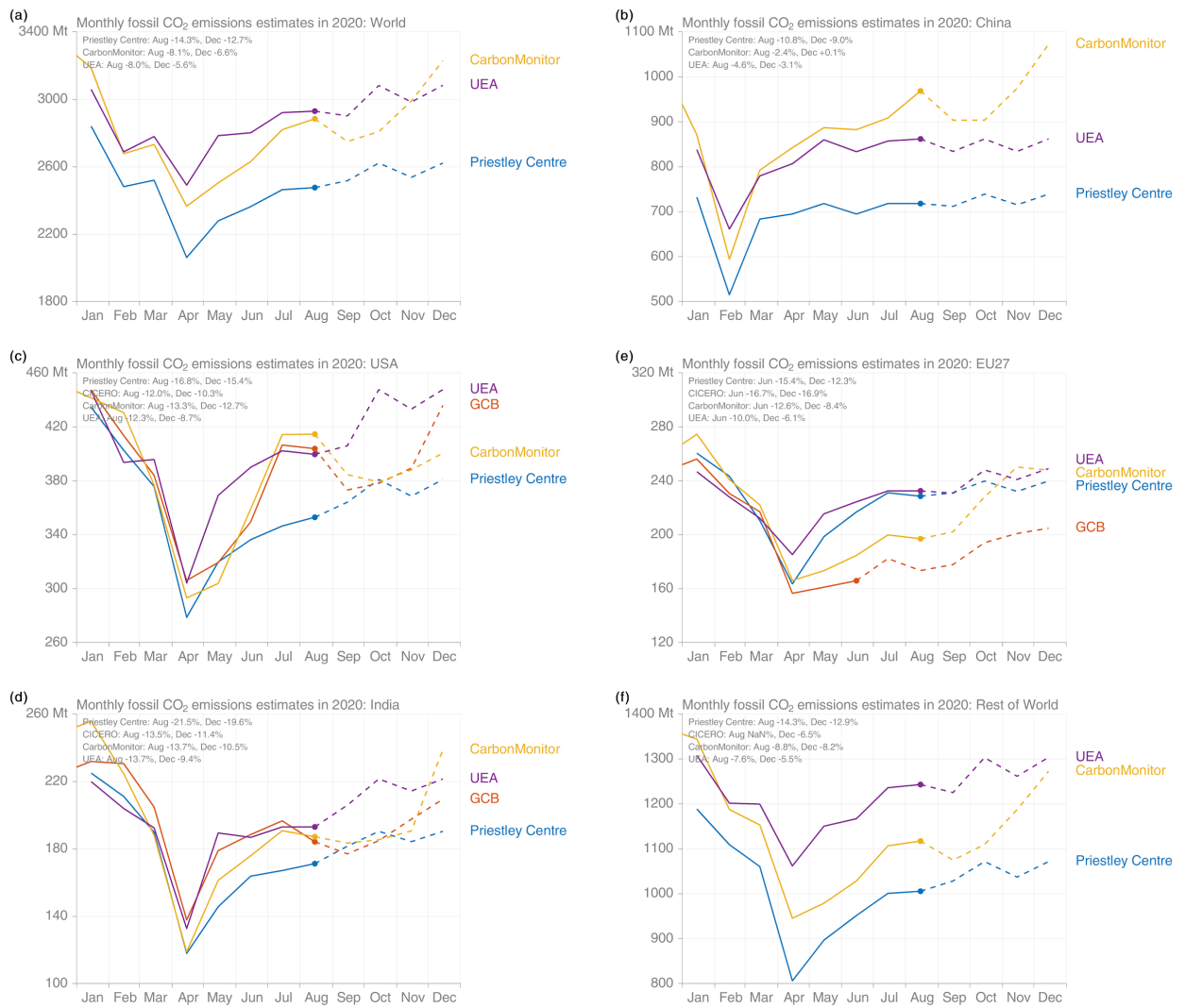


Figure B5. Monthly 2020 fossil CO₂ emission based on year-to-date data (solid lines) and projections (dashed lines) following four available approaches for (a) total world, (b) China, (c) USA, (d) European Union, (e) India, and (f) the rest of the world. Methods of the four approaches are described in Section 2.1.5 and Appendix C.

Appendix C. Supplementary Information

Details of the Global Carbon Budget projection method

China: The method for the projection uses: (1) the sum of monthly domestic production of raw coal, crude oil, natural gas and cement from the National Bureau of Statistics (NBS, 2020a), (2) monthly net imports of coal, coke, crude oil, refined petroleum products and natural gas from the General Administration of Customs of the People's Republic of China (2019); and (3) annual energy consumption data by fuel type and annual production data for cement from the NBS, using data for 2000-2018 (NBS, 2019), with the growth rates for 2019 taken from official preliminary statistics for 2019 (NBS, 2020a, 2020b). We estimate the full-year growth rate for 2020 using a Bayesian regression for the ratio between the annual energy consumption data (3 above) from 2014 through 2019, and monthly production plus net imports through August of each year (1+2 above). The uncertainty range uses the standard deviations of the resulting posteriors. Sources of uncertainty and deviations between the monthly and annual growth rates include lack of monthly data on stock changes and energy density, variance in the trend during the last three months of the year, and partially unexplained discrepancies between supply-side and consumption data even in the final annual data. The YTD estimate is made in the same way, but instead of regressing the ratio between historical monthly data for August and full-year annual data, monthly data for December is used instead, to produce regression results that capture the systematic differences between the monthly supply and annual consumption data, without the additional effect of projecting forward from August to the end of the year.

Note that in recent years, the absolute value of the annual growth rate for coal energy consumption, and hence total CO₂ emissions, has been consistently lower (closer to zero) than the growth or decline suggested by the monthly, tonnage-based production and import data, and this is reflected in the projection. This pattern is only partially explained by stock changes and changes in energy content, and it is therefore not possible to be certain that it will continue in any given year. For 2020 in particular, COVID-19-related lockdown and reopening in China, similar but delayed restrictions in major export markets, as well as unusual amounts of flooding and extreme weather during the summer months imply that seasonal patterns and correlations between supply, stock changes and consumption are likely to be quite different this year than

in the previous years that the regression is based on. This adds a major but unquantified amount of uncertainty to the estimate.

USA: We use emissions estimated by the U.S. Energy Information Administration (EIA) in their Short-Term Energy Outlook (STEO) for emissions from fossil fuels to get both YTD and a full year projection (EIA, 2020). The STEO also includes a near-term forecast based on an energy forecasting model which is updated monthly (last update with preliminary data through August 2020), and takes into account expected temperatures, household expenditures by fuel type, energy markets, policies, and other effects. We combine this with our estimate of emissions from cement production using the monthly U.S. cement data from USGS for January-June 2020, assuming changes in cement production over the first part of the year apply throughout the year.

India: We use monthly emissions estimates for India updated from Andrew (2020) through August. These estimates are derived from many official monthly energy and other activity data sources to produce direct estimates of national CO₂ emissions, without the use of proxies. For purposes of comparison with other methods, we use a simple approach to extrapolating their observations by assuming the remaining months of the year change by the same relative amount compared to 2019 in the final month of observations.

EU: We use (1) monthly coal delivery data from Eurostat for January through June 2020 (Eurostat, 2020); (2) monthly oil and gas demand data for January through June from the Joint Organisations Data Initiative (JODI, 2020), with adjustments for deliveries to petrochemical industries using data from Eurostat (2020); and (3) cement production is assumed stable. For purposes of comparison with other methods, we use a simple approach to extrapolating their observations by assuming the remaining months of the year change by the same relative amount compared to 2019 in the final month of observations.

Rest of the world: This method only provides a full year projection. We use the close relationship between the growth in GDP and the growth in emissions (Raupach et al., 2007) to project emissions for the current year. This is based on a simplified Kaya Identity, whereby E_{FOS} (GtC yr⁻¹) is decomposed by the product of GDP (USD yr⁻¹) and the fossil fuel carbon intensity of the economy (I_{FOS} ; GtC USD⁻¹) as follows:

$$E_{FOS} = GDP \times I_{FOS} \quad (3)$$

Taking a time derivative of Equation (3) and rearranging gives:

$$\frac{1}{E_{FOS}} \frac{dE_{FOS}}{dt} = \frac{1}{GDP} \frac{dGDP}{dt} + \frac{1}{I_{FOS}} \frac{dI_{FOS}}{dt} \quad (4)$$

where the left-hand term is the relative growth rate of E_{FOS} , and the right-hand terms are the relative growth rates of GDP and I_{FOS} , respectively, which can simply be added linearly to give the overall growth rate.

The I_{FOS} is based on GDP in constant PPP (Purchasing Power Parity) from the International Energy Agency (IEA) up to 2017 (IEA/OECD, 2019) and extended using the International Monetary Fund (IMF) growth rates through 2019 (IMF, 2020). Interannual variability in I_{FOS} is the largest source of uncertainty in the GDP-based emissions projections. We thus use the standard deviation of the annual I_{FOS} for the period 2009-2019 as a measure of uncertainty, reflecting a $\pm 1\sigma$ as in the rest of the carbon budget.

World: This method only provides a full year projection. The global total is the sum of each of the countries and regions, but this year we additionally apply a GDP approach to the world to provide an additional consistency check (see Rest of World Description).